ELECTRONIC AND TRANSPORT PROPERTIES OF ARMCHAIR GRAPHENE NANORIBBON JUNCTIONS INVOLVING ZIGZAG EDGE INTERFACES

LI SUCHUN

NATIONAL UNIVERSITY OF SINGAPORE

2014

ELECTRONIC AND TRANSPORT PROPERTIES OF ARMCHAIR GRAPHENE NANORIBBON JUNCTIONS INVOLVING ZIGZAG EDGE INTERFACES

LI SUCHUN

(*B.Sc.* (*Hons.*), *NTU*)

A THESIS SUBMITTED

FOR THE DEGREE OF DOCTOR OF PHILOSOPHY

NUS GRADUATE SCHOOL FOR INTEGRATIVE

SCIENCES AND ENGINEERING

NATIONAL UNIVERSITY OF SINGAPORE

2014

Declaration

I hereby declare that the thesis is my original work and it has been written by me in its entirety. I have duly acknowledged all the sources of information which have been used in the thesis.

This thesis has also not been submitted for any degree in any university previously.

Li Suchun

14 April 2014

Acknowledgement

First of all, I wish to thank my supervisors, Professor Feng Yuan Ping and Professor Quek Su Ying, for their consistent guidance and support throughout my Ph.D. Their contagious enthusiasm and creativity are invaluable inspirations for me, and I truly value their constructive advice at every step of the research.

Next, we wish to acknowledge our collaborators: Dr. Young-Woo Son from the Molecular Foundry in Berkeley (currently at the Korea Institute for Advanced Studies) and Dr. Chee Kwan Gan from Institute of High Performance Computing (IHPC), A*STAR. This project began as a collaboration between the Molecular Foundry and IHPC, coordinated by Prof. Su Ying Quek. Dr. Young-Woo Son has obtained very intriguing preliminary results, which motivates us to extend the work into a comprehensive Ph.D project. They have also been very helpful in providing active discussions in later stages of the project.

We gratefully acknowledge Prof. Steven G. Louie, Marvin L. Cohen, and Jeffrey B. Neaton for preliminary discussions. We thank the chair of my thesis advisor committee (TAC) Prof. Sow Chorng Haur for his help throughout the whole Ph.D journey. I also wish to thank members in Prof. Su Ying Quek's group including Dr. Luo Xin, Dr. Narjes Gorjizadeh, Dr. Amy K. H. Khoo, and members in Prof. Feng Yuan Ping's group including Dr. Shen Lei, Dr. Zeng Ming Gang, Dr. Wu Rongqin, Dr. Yang Ming, Dr. Zhou Miao, Dr. Bai Zhaoqiang, Dr. Wu Qingyun, Miss Sandhya, Prof. Lu Yunhao, Prof. Li Dechun, Prof. Liu Jun, etc. for their valuable discussions and kind help.

I thank A*STAR for the supportive financial support through the A*STAR Graduate Scholarship. I thank A*STAR Graduate Academy (A*GA) and NUS Graduate School for Integrative Sciences and Engineering (NGS) for their consistent support, and the Department of Physics and IHPC for the kind hosting. We acknowledge A*STAR Computational Resource Centre and Graphene Research Centre for computational support. Special thanks to Prof. Hyoung-Hoon Choi for the SCARLET code.

Finally, I am very grateful of my family and my previous schools, especially my Physics teachers including Mr. Jiang Lin (Anqiu No. 1 High School, Shandong Province, China) and Prof. Wang Lan (undergraduate research supervisor, Physics Division of NTU), etc. for stimulating and fostering my interest in Physics. I also thank the Singapore government for the Undergraduate SM3 Scholarship, which supports me to pursue my interest in Physics at NTU.

Contents

Summary

Nanoscale size and geometry effects play important roles in determining the properties of graphene nanostructures. On one hand, graphene nanoribbons with armchair edges (AGNRs) possess bandgaps that are strongly dependent on the ribbon width. On the other hand, the zigzag edge of graphene supports a spin-polarized edge state around the Fermi level E_F. We wonder what phenomena would appear if we combine *AGNRs* and *zigzag edges* into a single nanostructure?

We designed a junction where a narrow AGNR is sandwiched in-between two wide AGNR-leads and naturally incorporating zigzag edges at the interfaces. We find that when the middle AGNR is in the 3*p*+2 family, the junction exhibits two transmission peaks that are *independent of the length* of the narrow AGNR segment. This is unexpected from the quantum confinement effect, which predicts that the energy of a confined state approaches E_F as the ribbon gets longer.

By investigating the eigenchannel wavefunctions, we revealed that this length-independence behavior arises from the locally repeating pattern in the wavefunction. We proved from mathematical induction that *an eigenstate containing at least three locally repeating units in the eigenwavefunction pattern has an invariant eigenenergy as the structure lengthens.* Although a periodic wavefunction pattern is straightforward in an infinite periodic structure, it can hardly be preserved when the structural symmetry is broken. A locally repeating pattern can be preserved here because of the zigzag edges serving as sources/drains, so that electrons are not confined within the AGNR segment. However, the zigzag edge state is able to provide electrons only for states near E_F, which explains why such length-independent transmission peaks are observed only for 3*p*+2-AGNRs, but not for other AGNRs with much larger gaps.

The length-independent transmission makes AGNR-junctions excellent molecular wires exhibiting an invariant conductance as the wire lengthens. This solves a big problem as traditional molecular wires suffer from fast exponential decay of conductance with wire length.

We further find that these states are bonding and antibonding couplings of two Fermi level states. The original state originates from the zigzag edge and extends into the middle AGNR within the same sub-lattice. Such extension results in a non-decaying state in 3*p*+2-AGNRs and an exponentially decaying evanescent state in 3*p*- and 3*p*+1-AGNRs.

The extension into an AGNR overcomes the localized nature of the zigzag edge state, potentially leading to many interesting phenomena. For example, in the symmetric AGNR-junction we studied, zigzag edges at two interfaces are coupled across the AGNR in-between them. Such coupling results in perfect transmission channels showing length-independent transmission peaks in 3*p*+2-AGNRs. We further demonstrate that these channels can be destroyed if we break the degeneracy of the two extended states by applying opposite spin-polarizations. In this way, we can obtain a *large magnetoresistance* reaching ~900%.

The AGNR-junctions also show excellent properties making them suitable for achieving *negative differential resistance* (NDR) with low on-site voltage and high peak-to-valley ratio. By utilizing a semiconducting AGNR as the leads, we can drive the transmission peak close to E_F into the gap of leads and obtain NDR via the resonant tunneling mechanism.

Publications

[1] **Suchun Li**, Young-Woo Son, and Su Ying Quek, *"Extension of the Graphene Zigzag Edge State into a Front Armchair Ribbon"* (preparing).

[2] **Suchun Li**, Yuan Ping Feng, and Su Ying Quek, *"Origin of the double bands in armchair graphene nanoribbons of the 3p+1 family"* (preparing).

[3] **Suchun Li**, Chee-Kwan Gan, Young-Woo Son, Yuan Ping Feng, and Su Ying Quek *"Low-bias Negative Differential Resistance Effect in Armchair Graphene Nanoribbon Junctions"* (accepted by APL).

[4] **Suchun Li**, Young-Woo Son, and Su Ying Quek, *"Large Magnetoresistance from Long-Range Interface Coupling in Armchair Graphene Nanoribbon Junctions"* (accepted by APL).

[5] Khoong Hong Khoo, Yifeng Chen, **Suchun Li**, and Su Ying Quek, *"Length Dependence of Electron Transport through Molecular Wires – A First Principles Perspective"* Phys. Chem. Chem. Phys. 17, 77 (2015).

[6] Matthew Yankowitz, Joel I-Jan Wang, **Suchun Li**, A. Glen Birdwell, Yu-An Chen, K. Watanabe, T. Taniguchi, Su Ying Quek, Pablo Jarillo-Herrero, and Brian J. LeRoy, "*Band Structure Mapping of Bilayer Graphene via Quasiparticle Scattering*" APL Mat. 2, 092503 (2014).

[7] **Suchun Li**, Chee-Kwan Gan, Young-Woo Son, Yuan Ping Feng, and Su Ying Quek *"Anomalous Length-Independent Frontier Resonant Transmission Peaks in Armchair Graphene Nanoribbon Molecular Wires"* Carbon 76, 285 (2014).

[8] Lei Shen (沈雷), Minggang Zeng, **Suchun Li**, Michael B. Sullivan, and Yuan Ping Feng *"Electron transmission modes in electrically biased graphene nanoribbons and their effects on device performance"* Phys. Rev. B 86, 115419 (2012).

[9] **S. C. Li**, P. Ren, B. C. Zhao, B. Xia and L. Wang *"Room temperature ferromagnetism of bulk polycrystalline* $(In_{0.85}\text{-}xSnxFe_{0.15})_2O_3$*: charge carrier mediated or oxygen vacancy mediated?"* Appl. Phys. Letts. 95, 102101 (2009).

List of Figures

List of Abbreviations

GNR	Graphene Nanoribbon
AGNR	Armchair Graphene Nanoribbon
ZGNR	Zigzag Graphene Nanoribbon
n-AGNR	AGNR with *n* carbon atoms spanning its width
m-ZGNR	ZGNR with *m* zigzag-shaped carbon chain
AGNR junction	Junction made of a narrower AGNR in-between two wider AGNRs
AGNR Z-Z junction	AGNR junction with zigzag edges at both interfaces
AGNR Z-A junction	AGNR junction with one zigzag edge interface and one armchair edge interface
AGNR A-A junction	AGNR junction with armchair edges at both interfaces
BZ	Brillouin Zone
E_F	Fermi energy/level
2D	two-dimensional
1D	one-dimensional
quasi-1D	quasi-one-dimensional
MO	Molecular Orbital
LCAO	Linear Combination of Atomic Orbitals
TB	Tight-Binding
nn	nearest neighbors
DFT	Density Functional Theory
LDA	Local Density Approximation
NEGF	Non-Equilibrium Green's Function
HOGO	Highest Occupied Gamma-point wavefunction Orbital
LUGO	Lowest Unoccupied Gamma-point wavefunction Orbital
HOGO-(*n*-1)	n^{th} Highest Occupied Gamma-point wavefunction Orbital
LUGO+(*n*-1)	n^{th} Lowest Unoccupied Gamma-point wavefunction Orbital

Chapter 1. Introduction

1.1 Size and Geometry Effects in Graphene Nanostructures

Graphene is a two-dimensional material consisting of carbon atoms linked together within a single layer in a hexagonal honeycomb lattice, as shown in Fig. 1.1 (a) [1-3]. The reciprocal lattice of graphene is also hexagonal, the first Brillouin Zone (BZ) of which is shown in Fig. 1.1 (b).

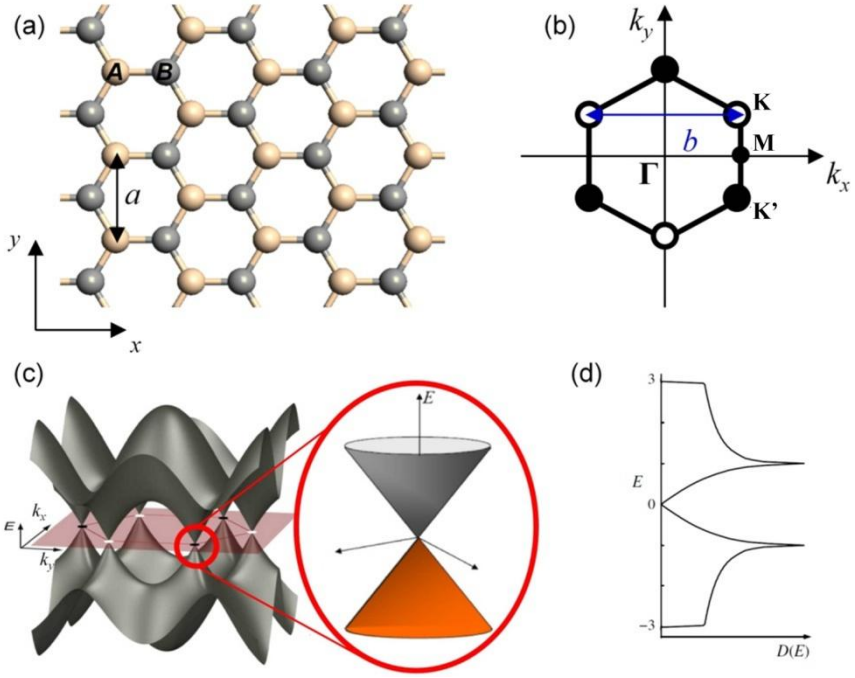

Fig. 1.1 (a) Atomic structure of graphene in real space, where the yellow and gray balls represent carbon atoms on the A- and B-sublattices, and a is the lattice constant. (b) The reciprocal lattice of graphene, where $b = \frac{4\pi}{\sqrt{3}a}$, and $\mathbf{K} = \frac{2\pi}{3a}(\sqrt{3}, 1)$, $\mathbf{K'} = \frac{2\pi}{3a}(\sqrt{3}, -1)$. (c) The π bandstructure from tight-binding calculations, adapted from Ref. [4]. Copyright Institute of Physics. (d) The density of states of graphene, adapted from Ref. [5]. Copyright Institute of Physics.

This unique carbon lattice determines graphene as a zero-gap semiconductor with the conduction band and the valence band touching each other at the 6 Dirac points **K** and

K′ (Fig. 1.1 (c)) [6, 7]. Most interestingly, the dispersion relation close to the Dirac points is linear, which leads to zero effective mass for electrons and holes, thus an extremely high Fermi velocity $v_F \sim 10^6$ m/s. The density of states (DOS) vanishes at the Fermi level E_F (Fig. 1.1 (d)).

Although graphene possesses many outstanding properties, its application in semiconductor-based electronics is greatly limited by the fact that there is no bandgap. Cutting the two-dimensional (2D) graphene into a quasi-one-dimensional (quasi-1D) nanoribbon is a good way to open a gap via the quantum size confinement effect across the width. Finite termination of graphene results in two types of natural edge geometries: *armchair* edge and *zigzag* edge. Accordingly, a typical graphene nanoribbon (GNR) could be terminated with either armchair or zigzag edges on both sides and they are referred to as an AGNR or a ZGNR. Figure 1.2 (a) and (c) show examples of an AGNR and a ZGNR, where each dangling bond at the edge Carbon atoms is passviated with one Hydrogen atom. Following previous convention, we refer to an AGNR with *n* carbon atoms across its width as *n*-AGNR and a ZGNR with *m* zigzag-shaped chains across its width as *m*-ZGNR. The ribbons shown in Fig. 1.2 (a) and (c) are 5-AGNR and 4-ZGNR, respectively. As we will review in the next few sections, the difference in edge geometry brings many differences between the electronic properties of AGNRs and ZGNRs.

The reciprocal space of graphene is two-dimensional and continuous. By cutting the 2D graphene into a quasi-1D GNR, the wave vector corresponding to the width dimension of the ribbon $k_\perp$ is quantized into discrete $k_\perp^p$ values due to quantum confinement effect, whereas the wave vector corresponding to the longitudinal dimension of the GNR $k_\parallel$ remains continuous. As a result, the reciprocal space of a quasi-1D GNR is composed

of 1D lines along the continuous $k_{\parallel}$ direction and with discrete $k_{\perp}^{p}$ values, that slices through the 2D reciprocal space of graphene.

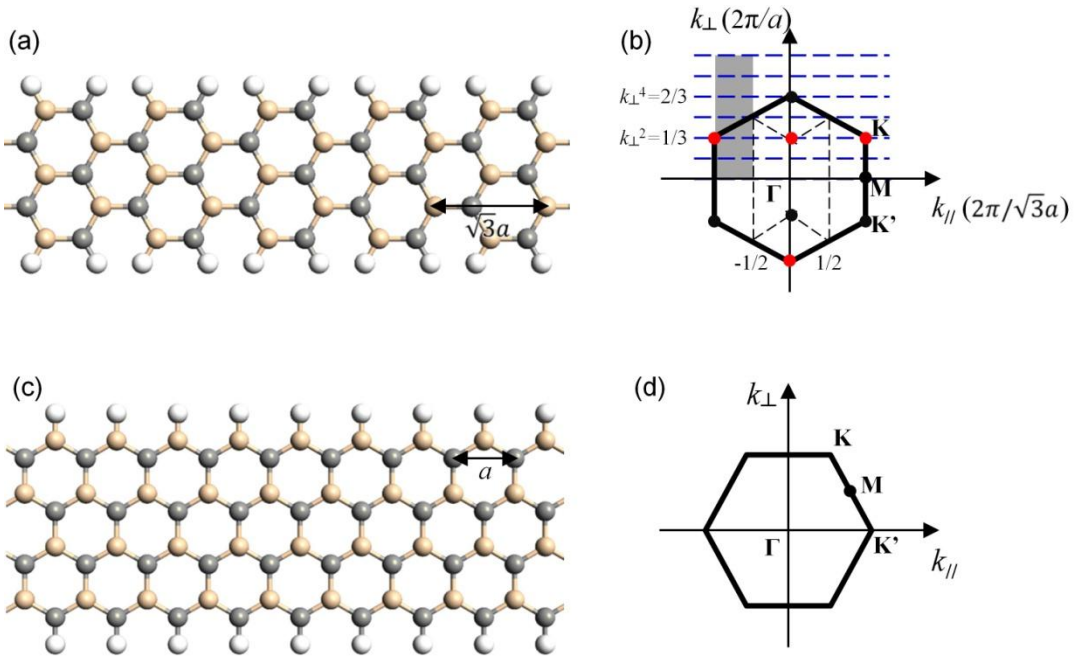

Fig. 1.2 (a) Atomic structure of 5-AGNR, where the yellow (gray) balls represent carbon atoms on the A(B)-sublattice and the white balls represent passivating Hydrogen atoms. (b) The reciprocal space of a quasi-1D AGNR, indicated by the parallel dashed blue lines within the 2D reciprocal space of graphene. The shaded region indicates an alternative reduced BZ of graphene [8]. (c) Atomic structure of 4-ZGNR. (d) The continues wave vector $k_{\parallel}$ and quantized wave vector $k_{\perp}$ for ZGNRs, within the 2D reciprocal space of graphene. The length unit cells in AGNRs and ZGNRs are $\sqrt{3}a$ and a, respectively.

The continuous $k_{\parallel}$ vector of AGNRs turns out to be along the direction from **Γ** point to **M** point, while that of ZGNRs turns out to be along the direction from **Γ** point to **K** point (Fig. 1.2 (b) and (d)). The Dirac **K** points in graphene reciprocal lattice are then folded onto the **Γ** point ($k_{\parallel}=0$) and $k_{\parallel}=\pm\frac{2\pi}{3a}$ & $\pm\frac{4\pi}{3a}$ points of the quasi-1D reciprocal space of AGNRs and ZGNRs, respectively. The parallel dashed blue lines in Fig. 1.2 (b) indicate the slicing planes (normal to the paper) for an AGNR. In this way, the global bandstructure of a quasi-1D AGNR can be surmised by projecting the 2D

bandstructure of graphene onto these parallel planes. For the case of ZGNRs, the quantized $k_\perp^p$ values depend on the longitudinal wave vector $k_\parallel$, so the slicing planes are slightly curved, rather than being flat [9, 10]. Moreover, one quantized $k_\perp^p$ value of *m*-ZGNR involves an imaginary part within the region $k_c < |k_\parallel| \leq \pi/a$, where $k_c = 2\cos^{-1}\left(\frac{1}{2(1+1/m)}\right) \sim 2\pi/3a + 2/(\sqrt{3}m)$. This imaginary $k_\perp^p$ gives rise to a partial flat band and a localized edge state.

According to the slicing principle reviewed above, a GNR would be metallic (gap = 0) if its reciprocal space includes any Dirac point, and semiconducting otherwise. The reciprocal space of ZGNRs will always include a Dirac point at $k_\parallel = \pm 2\pi/3a$, thus ZGNRs are metallic without considering magnetic effect that opens a gap [11, 12]. On the other hand, the flat slicing planes for *n*-AGNR will pass through a Dirac point if and only if $n = 3p+2$, where p is a positive integer. Therefore, the nearest neighbor tight-binding model predicts that 3*p*+2-AGNRs are metallic, whereas 3*p*- and 3*p*+1-AGNRs are semiconducting [8, 11, 13-17]. However, if edge deformation due to Peierls' distortion is taken into account, 3*p*+2-AGNRs also exhibit a small gap [12].

1.1.1 The Family Behavior of AGNRs

This family behavior of AGNRs can be understood by simply considering an AGNR as a quantum well with hard walls (vacuum) on both sides and examining how $k_\perp^p$ is quantized within this quantum well [9, 10, 17], as illustrated in Fig. 1.3. For each sub-lattice A and B, we represent the width dimension wavefunction component at an atomic site on the i^{th} row as $\phi_A(i)$ and $\phi_B(i)$, respectively. We may apply the hard wall boundary condition by requiring

$$\begin{cases} \phi_A(0) = \phi_B(0) = 0 & (1.1a) \\ \phi_A(n+1) = \phi_B(n+1) = 0 & (1.1b) \end{cases}$$

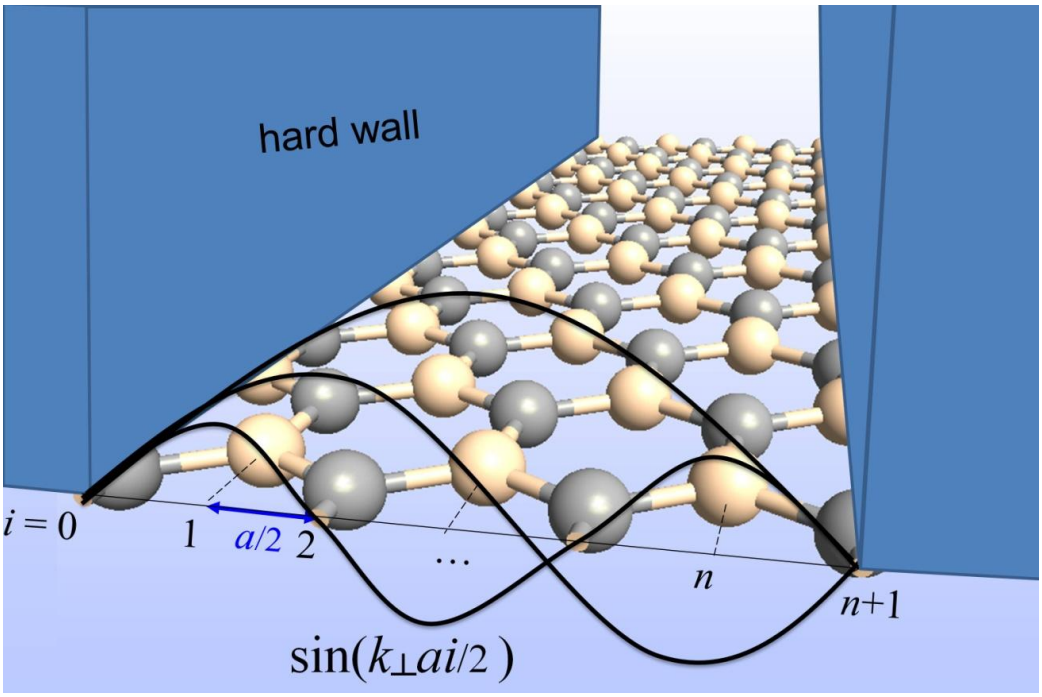

Fig. 1.3 Illustration of viewing *n*-AGNR as a quantum well between two hard walls. *a* is the lattice constant of graphene.

We choose the simple quantum well solution $\phi_A(i) = \phi_B(i) = \sin(k_\perp ai/2)$, which already satisfies the boundary condition at one hard wall $\phi_A(0) = \phi_B(0) = 0$. By letting $\phi_A(n+1) = \phi_B(n+1) = \sin(k_\perp a(n+1)/2) = 0$, we obtain $k_\perp a(n+1)/2 = p\pi$, where p is an integer. Therefore, the wave vector across the width is quantized to

$$k_\perp^p = \frac{2p\pi}{(n+1)a} \qquad (1.2)$$

$k_\perp^p$ would cut through a Dirac point if $k_\perp^p = \frac{2p\pi}{a(n+1)} = \frac{2\pi}{3a}$, which requires that $n = 3p - 1$. Since $n \geq 3$ for a real AGNR, we usually represent this metallicity requirement as

$$n = 3p + 2, \quad p = 1, 2, 3, \ldots \qquad (1.3)$$

For example, when n = 5, the 2D π-band of graphene reduces to 5 1D sub-bands corresponding to 5 discrete $k_{\perp}^{p}$ values within (0, $2\pi/a$): $\pi/3a$, $2\pi/3a$, π, $4\pi/3a$, and $5\pi/3a$, where both $2\pi/3a$ and $4\pi/3a$ pass through the Dirac point.

Figure 1.4 (a-c) shows the tight-binding bandstructures and DOSs of AGNRs with various widths. When the AGNR is as wide as n = 30, the bandstructure closely resembles the projection of the 2D graphene bandstructure onto the armchair axis (Fig. 1.4 (d)), except for a very small gap opening. As the AGNR becomes narrower, the number of bands is gradually reduced due to quantization effects. Consistent with the hard wall model we reviewed above, the bandstructures and DOSs indicate clearly that AGNRs with width $n = 3p + 2$ (Fig. 1.4 (b)) are metallic, whereas AGNRs with widths $n = 3p$ (Fig. 1.4 (c)) and $n = 3p + 1$ (Fig. 1.4 (a)) are semiconducting.

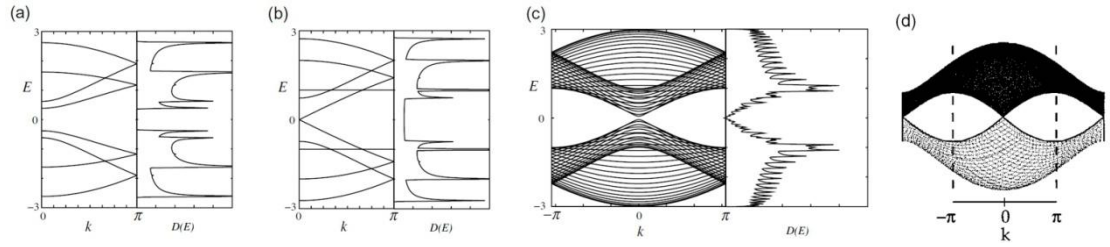

Fig. 1.4 Tight-binding band structure and Density of States of *n*-AGNRs with width *n* = (a) 4, (b) 5, and (c) 30, adapted from Ref. [5]. Copyright Institute of Physics. The energy *E* is scaled by the tight-binding hopping integral t = 2.75eV. (d) The projected band structure of 2D graphene onto an armchair axis, reprinted with permission from Ref. [13]. Copyright (1996) by the American Physical Society. Dashed lines at π and –π indicate the boundary of the first BZ. Note that *k* in all these figures is in unit of $\left(\sqrt{3}a\right)^{-1}$, rather than Å^{-1}

Later, the 3*p*+2-AGNRs were found to be also semiconducting by both first-principles [12] and tight-binding [17] analysis considering shorter bonds at the armchair edges. Figure 1.5 shows the bandgaps of all three families of AGNRs as a function of width by both local density approximation (LDA) [12] and with GW corrections included [18]. For all three families, the bandgap decays as the ribbon becomes wider, consistent with

the quantum confinement effect. Experimental results also confirm that energy gaps do increase with decreasing ribbon width [19].

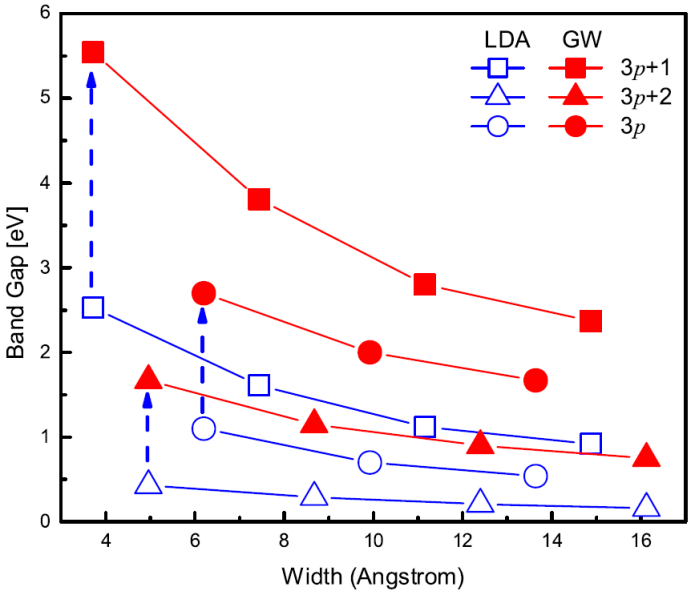

Fig. 1.5 The bandgaps of three families of *n*-AGNRs as a function of width by first principles and GW calculations, reprinted with permission from Ref. [18]. Copyright (2007) by the American Physical Society.

These AGNRs can now be synthesized from bottom-up approaches with well controlled widths [20-24].

1.1.2 The Dirac Point State in 3*p*+2-AGNRs

The **Γ** point state in metallic 3*p*+2-AGNRs stems from the Dirac point state in graphene by zone folding (Fig. 1.2 (b)). This Dirac point state is predicted to show a very interesting pattern: *the probability density disappears at every third row of carbon atoms* counting from the edge [8], as illustrated in Fig. 1.6. Such interesting pattern is a characteristic feature of the **Γ** point state in 3*p*+2-AGNRs. It has been recognized in the literature since 1987 [17, 25-27] and recently observed in the experimental STM image of 14-AGNR [23], as shown in Fig. 1.6 (b).

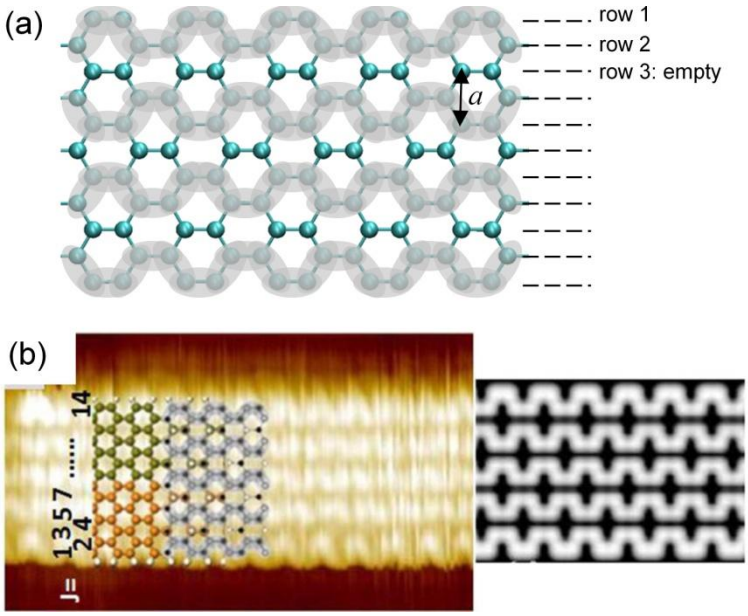

Fig. 1.6 (a) The electron density pattern of the analytical tight-binding state at the Dirac point in 11-AGNR. a = lattice constant. (b) The electron scattering pattern visualized with Scanning Tunneling Microscope (left) and corresponding DFT simulations (right) in 14-AGNR, adapted from Ref. [23] with permission.

Such an interesting pattern with a line node every three carbon rows can be understood as a standing wave formed by intervalley backscattering of the Fermi electrons (electrons at the Fermi energy) scattered off the armchair-edges on both sides of a 3p+2-AGNR [8]. The Fermi electrons at Dirac point **K** is backscattered to another Dirac point **K'** (see Fig. 1.2 (b)). The incoming and scattered electron waves then interfere to form a standing wave. The wave vector difference between these two waves is $\Delta k = 4\pi/3a$ (Fig. 1.2 (b)), resulting in a wavelength of $2\pi/\Delta k = 3a/2$ for the resulting standing wave. $3a/2$ is exactly three rows of carbon atoms across the width of AGNR, consistent with the standing wave pattern shown in Fig. 1.6.

Such a standing wave does not exist in AGNRs of other families ($n \neq 3p + 2$), since there is no Fermi electrons available in those semiconducting AGNRs. However, it is predicted that for a state slightly away from the Dirac point by $\delta\theta$, the densities at the $(3j)^{th}$ row is proportional to $\sin^2(3j\delta\theta)$. Therefore, as j increases or as we go to the

inner region from the armchair edge, the density at the $(3j)^{th}$ row gradually increases [8]. As a result, the periodic absence of probability density at the $(3j)^{th}$ row is not seen for j being sufficiently away from the armchair edge. The STM image in Fig. 1.7 shows clearly that the density at the $(3j)^{th}$ row is suppressed for $j \leq 3$ and the appreciable density appears for $j > 3$.

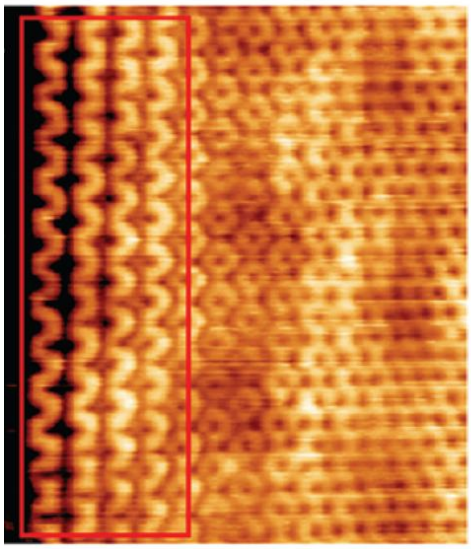

Fig. 1.7 STM topography showing quantum interference at a regular armchair edge of a graphene monolayer, adapted with permission from Ref. [28]. Copyright (2010) American Chemical Society.

1.1.3 The Zigzag Edge State

From the review in previous sections, we see that the electronic properties of AGNRs are determined mainly by the quantization effect across the width. The armchair edges introduce little effect except a slight increase of bandgaps due to edge deformation. In contrast to the relatively inactive armchair edge, the zigzag edge supports an interesting edge state around E_F, that is localized along the edge and decays towards the inner region, as illustrated in Fig. 1.9 [11]. The edge state results in a partial flat band and a large DOS around E_F for ZGNRs, as shown in Fig. 1.8 (a-c). The partial flat band starts from $k = \pi/a$ and gets flatter with increasing ZGNR width. It reaches around $k = 2\pi/3a$ for a sufficiently wide 30-ZGNR (Fig. 1.8 (c)). There is no such partial flat

band in the projection of graphene bandstructure onto the zigzag axis (Fig. 1.8 (d)), indicating that the partial flat band is not originated from intrinsic states in graphene.

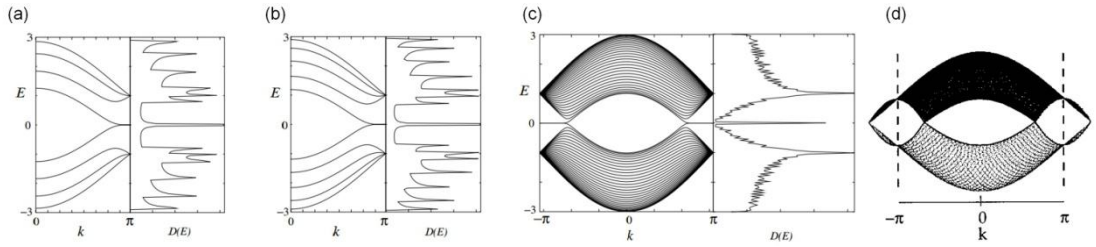

Fig. 1.8 (a-c) Tight-binding band structure $E(k)$ and Density of States $D(E)$ of (a) 4-ZGNR, (b) 5-ZGNR, and (c) 30-ZGNR, adapted from Ref. [5]. Copyright Institute of Physics. The energy E is scaled by the tight-binding hopping integral t = 2.75eV. (d) The projected band structure of graphene onto the zigzag axis, reprinted with permission from Ref. [13]. Copyright (1996) by the American Physical Society. Dashed lines at π and $-\pi$ indicate the boundary of the first BZ. Note that k in all these figures is in unit of a^{-1}, rather than $Å^{-1}$

The emergence of the puzzling zigzag edge state can be understood by analytically solving the tight-binding Hamiltonian of a semi-infinite graphene sheet with a zigzag edge termination [11], as indicated in Fig. 1.9. Considering the translational symmetry, we can start constructing the analytic solution for the edge state by letting the Bloch components of the linear combination of atomic orbitals (LCAO) be …, $e^{ik(n-1)a}, e^{ikna}, e^{ik(n+1)a}, \ldots$ on successive edge sites, where n donates a site location on the edge (see Fig. 1.9 (a)).

We consider the Schrödinger equation $H\psi = E\psi$ of the whole system and look for tight-binding form solution $\psi = (c_1, c_2, \ldots, c_i, \ldots)$ as a linear combination of the basis π-orbitals localized on each atomic site i of the graphene nanostructure. Then the Schrödinger equation can be written in matrix multiplication form as

$$\begin{bmatrix} H_{11} & H_{12} & \cdots & \\ H_{21} & \ddots & \cdots & \cdots \\ \vdots & \vdots & H_{ij} & \\ & \vdots & & \ddots \end{bmatrix} \begin{pmatrix} c_1 \\ c_2 \\ \vdots \\ c_i \\ \vdots \end{pmatrix} = E \begin{pmatrix} c_1 \\ c_2 \\ \vdots \\ c_i \\ \vdots \end{pmatrix} \quad (1.4)$$

where H_{ij} is the hopping integral between atoms *i* and *j*.

Each row *i* of the Schrödinger equation (1.4) reads

$$\sum_{j=\mathrm{nn}} H_{ij} c_j = E c_i \qquad (1.5)$$

Here, only interactions between nearest neighbors (nn) are taken into account, which is sufficient to describe the essential physics of π-electrons in graphene [29].

As the value of H_{ij} between nearest neighbors is identical over the whole structure, it is straightforward that for an eigenwavefunction ψ to satisfy the Schrödinger equation at $E = 0$ (at the Fermi energy), we would require

$$\sum_{j=nn} c_j = 0 \qquad (1.6)$$

for all atoms. Namely, *the sum of wavefunction coefficients on all nearest neighbors of any carbon atom has to vanish* [11].

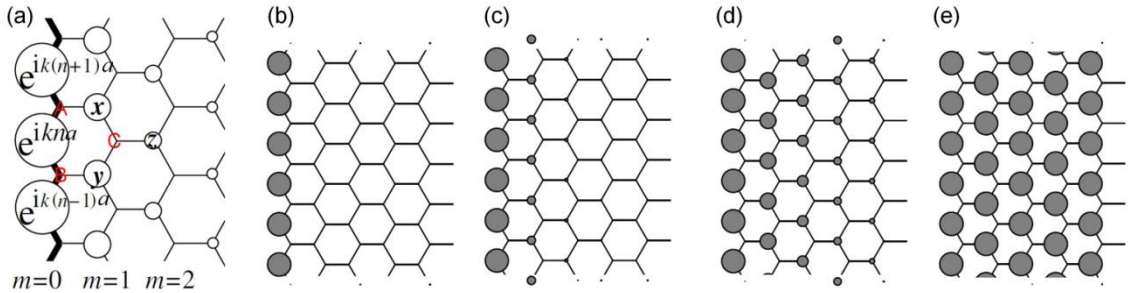

Fig. 1.9 (a) Analytical form of the edge state for a semi-infinite graphene sheet with a zigzag edge. The bold line indicates the zigzag edge, and A, B, C indicates the atomic sites. (b-e) Charge density plot for analytical solution of the edge state, when $k =$ (b) π/a, (c) $8\pi/9a$, (d) $7\pi/9a$, and (e) $2\pi/3a$. The radius of each circle in (a-e) is proportional to the charge density on each site. This figure is adapted from [5]. Copyright Institute of Physics.

Applying the sum rule to atomic sites A, B, and C in Fig. 1.9 (a), we have

$$e^{ikna} + e^{ik(n+1)a} + x = 0 \qquad (1.7a)$$

$$e^{ik(n-1)a} + e^{ikna} + y = 0 \qquad (1.7b)$$

$$x + y + z = 0 \qquad (1.7c)$$

We can easily solve this to obtain that

$$x = -2\cos(k/2)e^{ik(n+1/2)a} \qquad (1.8a)$$

$$y = -2\cos(k/2)\, e^{ik(n-1/2)a} \qquad (1.8b)$$

$$z = [-2\cos(k/2)]^2 e^{ikna} \qquad (1.8c)$$

If we start from the zigzag chain with m=1 to solve further inside, we would successively obtain the same form of solution: *the wavefunction component at each non-nodal site of the mth zigzag chain from the edge is proportional to* $[-2\cos(ka/2)]^m$. The convergence condition requires that $|-2\cos(ka/2)| \leq 1$. Otherwise, the state would diverge in a semi-infinite graphene sheet. This convergence condition defines the region $2\pi/3a \leq |k| \leq \pi/a$, where the partial flat band appears. As a result, the state is decaying from the edge towards the inner region following a power law, with the decaying rate depending on the wave number k. As shown in Fig. 1.9 (b-e), the state is completely localized at the edge for $k = \pi/a$ and gradually becomes a extended state at $k = 2\pi/3a$, which is nothing but the Dirac point state.

The edge state is reasonably robust even if the graphene edge does not have a clear zigzag shape [13]. In fact, a general edge structure that is not parallel to the armchair edge can have a zero-energy edge state, which was shown by analogy to the condition of the zero-energy Andreev bound state in an unconventional superconductor [30]. Recent studies have demonstrated the robustness of the edge state against changes in their size and geometry [31-33]. Nevertheless, the edge state does require a sp^2-configuration at the zigzag edge atoms, which is necessary to preserve the π electron

orbital. According to this principle, we can destroy the edge state by passivating each carbon atom at the zigzag edge with two (rather than one) Hydrogen atoms [34].

This robust edge state is also spin-polarized, it plays an important role in the magnetic properties of nano size graphene systems since it contributes significantly to the DOS near E_F. The existence of this magnetic state has been confirmed using mean field theory [11, 35-42], the density matrix renormalization group for the Hubbard model [43], and density functional theory [12, 44]. This magnetic edge state has induced many interesting phenomena, such as half-metallicity [45], spin-polarized transmission [46], spin-filtering and rectifying behaviors [47], large magnetoresistance [48-53], spin-valve effect [54, 55], and negative differential conductance [56].

This edge-localized state has been observed in recent experiments using scanning tunneling microscopy [57-60] and high-resolution angle-resolved photoemission spectroscopy (ARPES) [61]. Figure 1.10 shows one example of the experimentally observed zigzag edge state localized along the two edges of a GNR on Au (111).

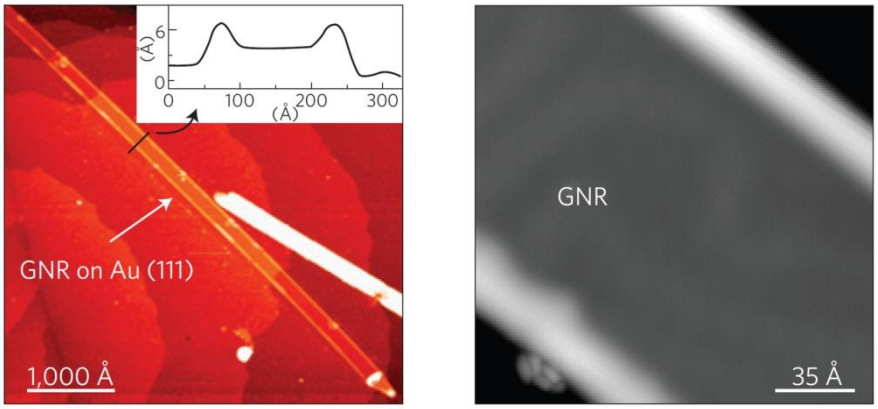

Fig. 1.10 Left panel: Constant-current STM image of a monolayer GNR on Au (111) at room temperature. Inset shows the indicated line profile. Right panel: Higher resolution STM image of a GNR at T = 7K (greyscale height map). This figure is adapted with permission from Ref. [60], copyright (2011).

The localized nature offers the zigzag edge state many intriguing properties including the magnetic ordering and perfectly conducting channels along the zigzag edge dimension [30]. On the other hand, it also prevents the state from interacting with other states that are located away from the edge.

1.2 Bonding and Antibonding Molecular Orbitals

In molecular orbital theory, bonding and antibonding orbitals are formed when isolated atomic orbitals (AO) combine to form molecules. Here, we illustrate this using an example of two 1s atomic orbitals of the Hydrogen atom, as shown in Fig. 1.11. When the two Hydrogen atoms are well isolated, there is no interaction between them, and they are at the same energy level. As the two hydrogen atoms approach one another, their atomic orbitals start to overlap. Therefore, the two atomic orbitals interact with each other and split into two molecular orbitals (MO) belonging to the pair.

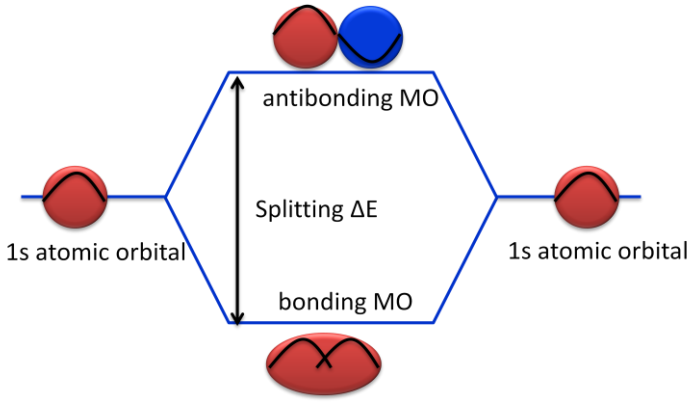

Fig. 1.11 Schematic illustration of two 1s atomic orbitals of the Hydrogen atom forming the bonding and antibonding molecular orbitals.

One of the MO comes from addition of the two atomic orbitals. It is lower in energy than the original atomic level, thus is more stable and promoting the bonding of two hydrogen atoms into hydrogen molecule H_2. Therefore, this MO is termed *bonding* MO. The other MO comes from subtraction of the two atomic orbitals and is higher in

energy than the original atomic level. This MO therefore is unstable and termed *antibonding* MO. As a result of the addition and subtraction, the wavefunction pattern of the bonding MO is symmetric whereas that of the antibonding MO is antisymmetric. The energy splitting ΔE between the bonding and antibonding MOs is determined by the coupling strength, which is strongly related to the overlap of the two atomic orbitals.

1.3 Motivation

As we have reviewed in Section 1.1, nanoscale size and geometry introduce many interesting effects into the electronic and magnetic properties of graphene nanostructures. Firstly, AGNRs show bandgaps mainly determined by their width. In particular, 3*p*+2-AGNRs involve a Dirac point state that shows an interesting node on every third row. Secondly, the graphene zigzag edge supports an edge state around E_F that is localized along the edge. If we combine the two geometries *AGNR* and *zigzag edge* into a single nanostructure, we expect to see more interesting phenomena. One good design of such a single structure could be a junction made of AGNRs of different widths and naturally incorporating zigzag edges at the interface, as shown in Fig. 1.12 (a). In such a junction, the AGNRs and the zigzag edge may interact with each other to produce new interesting phenomena.

1.3.1 Preliminary Results

Previous to our work, Dr. Young-Woo Son has studied the transmission properties of such an AGNR-junction from tight-binding approach. More specifically, the system for transport study is composed of a narrow AGNR segment sandwiched in-between two semi-infinite wider AGNRs (serving as the leads) and incorporating zigzag edges at the interfaces. Figure 1.12 (a) gives an example of such a system, i.e. a 5-AGNR segment

sandwiched between two semi-infinite 23-AGNRs with two zigzag edged interfaces; we call this a 23-5-23-AGNR Z-Z junction. As we will introduce in Chapter 5, if the junction involves one zigzag edged interface and one armchair-edged, we will call it a Z-A junction.

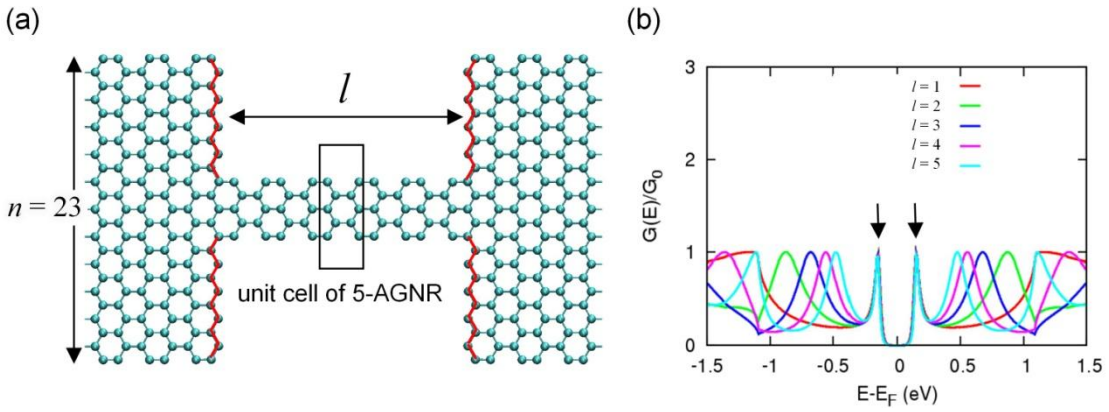

Fig. 1.12 (a) A junction made of a 5-AGNR segment sandwiched between two semi-infinite 23-AGNR leads and incorporating two zigzag edged interfaces (23-5-23-AGNR Z-Z junction). The red lines indicate the zigzag edges at the two interfaces. The black box indicates one unit cell within the 5-AGNR region, and the length of the 5-AGNR segment l = 5 unit cells. (b) Transmission curves of the 23-5-23-AGNR Z-Z junction with l varying from 1 to 5 unit cells, calculated by Dr. Young-Woo Son from tight-binding approach. Black arrows indicate two interesting peaks that do not depend on l. These results are unpublished, and we are adapting them here with permission from Dr. Young-Woo Son.

In particular, Dr. Son studied how the transmission curve varies as the length of the middle AGNR l increases. Figure 1.12 (b) shows the TB transmission results of the 23-5-23-AGNR Z-Z junction. As l increases, the quantum confinement effect becomes weaker, hence the energy levels of molecular orbitals inside the 5-AGNR reduces towards the Fermi level. Therefore, the corresponding resonant transmission peaks should also shift towards the Fermi level. Most of the transmission peaks follow this trend, such as the Lorentzian-shaped peaks within the ranges of (±1, ±0.25) eV in Fig. 1.12 (b). However, there are two sharp peaks immediately below and above E_F in the

23-5-23-AGNR Z-Z junction (indicated by black arrows in Fig. 1.12 (b)) that are almost independent of *l*.

1.3.2 Objective of the Current Ph.D Project

We are very curious of why the two transmission peaks are *l*-independent. This could be another interesting phenomenon arising from the nanoscale size and geometry effects. Therefore, we extended the research as a Ph.D project to explore the origin of this anomalous behavior. With the two *l*-independent peaks as a starting point, we hope we could obtain a complete understanding of the junction combining AGNRs and zigzag edges into a single structure, with a focus on any new phenomenon arising from the interaction of these two geometries.

In addition, the length-independent transmission spectrum suggests that the junction could sustain an invariant conductance with respect to length. As we know, molecular wires constitute the basic circuitry for nanoscale electronic devices [62]. However, most molecular wires studied to date are single molecule junctions [63-69], where the low-bias conductance *G* decays *exponentially* with the length *l* of the molecule, $G \sim \exp(-\beta l)$ [62-67, 69, 70], for molecular wires shorter than ~3 nm [63]. This exponential decay with length is a signature of off-resonant tunneling through evanescent states in the molecular wire close to the Fermi level [69, 71-73]. The promising potential application of AGNR-junctions as perfect molecular wires greatly increases our motivation to further investigate the electronic and transport properties of these junctions.

1.3.3 Thesis Outline

The current thesis is organized as follows:

In Chapter 1, we have reviewed several size and geometry induced electronic properties in graphene nanostructures, including the family behaviour of AGNRs and the zigzag edge state. We then introduced our motivation of studying a junction involving both AGNRs and zigzag edges and some preliminary transport results by Dr. Son's involving two very interesting length-independent transmission peaks.

In Chapter 2, we will review the calculation methods used in this Ph.D project, including how we construct the TB Hamiltonian, the density function theory, and two approaches to calculate the transport properties: scattering-state approach and non-equilibrium green's function approach.

In Chapter 3, we will present some of our further studies on the bandstructures and wavefunction of AGNRs. In particular, we will show a double bands feature in 3*p*+1-AGNRs and explain its origin from the quantization effect across the width of AGNR. We will also discuss how the "3*j*" wavefunction pattern is affected if we consider the deformation at the armchair edges of 3*p*+2-AGNRs. These AGNR results are good references for later discussion the AGNR-junctions in Chapters 4-9.

In Chapter 4, we answered "why the two transmission peaks are length-independent?" from both a mathematical approach analyzing the wavefunction pattern, and the physical origin attributed to the zigzag edges.

In Chapter 5, we further demonstrated that the two length-independent peaks arise from the bonding and antibonding coupling of two original states. The original states originates from the zigzag edge and extends into the middle AGNR within the same sublattice.

In Chapter 6, we showed that the extension of the zigzag edge state into the middle AGNR results in a real non-decaying state in 3*p*+2-AGNRs and a decaying evanescent state in 3*p*- and 3*p*+1-AGNRs.

In Chapter 7 and 8, we demonstrated two applications of the AGNR-junction: *Large magnetoresistance* based on the bonding and antibonding coupling principle and *negative differential resistance* based on the two peaks close to E_F and the gap in the AGNR leads.

Finally, we give a short conclusion and propose possible directions worth future investigation in Chapter 9.

Chapter 2. Calculation Methodology

2.1 Tight-Binding Hamiltonian

Consider a system where electrons are tightly bound to the atoms, i.e. the orbital ϕ_i of each electron is strongly localized at an atom, then we can use ϕ_i as the basis and approximate the solution to the whole system as a linear combination of these atomic orbitals (LCAO)

$$\psi = \sum_i c_i \phi_i \quad (2.1)$$

Substituting this form of wavefunction into the Schrödinger equation for the whole system $H\psi = E\psi$, we get

$$\sum_i c_i H|\phi_i\rangle = E \sum_i c_i |\phi_i\rangle \quad (2.2)$$

We can obtain each element H_{ji} of the Hamiltonian H by multiplying $\langle\phi_j|$ on both sides of Eqn.(2.2)

$$\sum_i c_i \big(\langle\phi_j|H|\phi_i\rangle - E\langle\phi_j|\phi_i\rangle\big) = 0 = \sum_i c_i \big(H_{ji} - ES_{ji}\big) \quad (2.3)$$

Assuming the Hamiltonian as a sum of all the atomic Hamiltonians H_i (Hamiltonians for isolated atoms) perturbed by the crystal field of other atoms H_{other}, then each diagonal element

$$H_{ii} = \langle\phi_i|H|\phi_i\rangle = \langle\phi_i|\sum_i H_i + H_{other}|\phi_i\rangle = E_i + \langle\phi_i|H_{other}|\phi_i\rangle \quad (2.4)$$

is the atomic energy E_i plus a shift due to the crystal field of other atoms H_{other}. The shift is usually small since the atomic orbitals $|\phi_i\rangle$ are strongly localized (tightly bound) on atom i.

The off-diagonal matrix element $H_{ij} = E_j S_{ij} + \langle \phi_i | H_{other} | \phi_j \rangle$ is the hopping integral that couples the atomic orbitals $|\phi_i\rangle$ and $|\phi_j\rangle$ together. It is closely related to the overlapping between the atomic orbitals $S_{ij} = \langle \phi_i | \phi_j \rangle$. This value is larger when orbitals ϕ_i and ϕ_j are spatially closer to each other, and becomes negligible when ϕ_i and ϕ_j are separated far away. In many cases, the matrix elements H_{ij} and S_{ij} are found from either first-principles calculations or experimental data. For example, the hopping integral between nearest neighbours of the π-orbitals in graphene is found to be $-2.7eV$ [29]. We then solve the Tight-Binding (TB) Hamiltonian matrix to find the eigenenergies E_m and vector form eigenwavefunctions $\psi_m = (c_1, c_2, \dots, c_i, \dots)$, where m is the index of the eigen-solution.

In the present Ph.D project, we used this tight-binding model to calculate the eigenstates of graphene nanostructures under periodic boundary conditions, including perfect AGNRs (see Section 3.4) and AGNR Z-Z junctions. We consider interactions between nearest neighbours only, which is sufficient to describe the essential physics of graphene π-electrons [12, 29]. Figure 2.1 shows a ladder representation of the 23-5-23-AGNR Z-Z junction. Each body atom has three nearest neighbours: on the top, bottom, and left/right, while each edge atom has only two nearest neighbours. We apply the periodic boundary condition along the length direction (z direction in Fig. 2.1) by making atoms at the most left column to be neighbouring with atoms at the most right column. The length of 23-AGNR segment is 8 unit cells, which we found is enough to screen effects from the other zigzag edge over the 23-AGNR from our convergence

tests. As the unit cell of this periodic structure contains a huge number of atoms N, the Hamiltonian matrix is of dimension N×N. We use MATLAB to solve the Hamiltonian and obtain the eigenenergies and eigenwavefunctions at **Γ**-point.

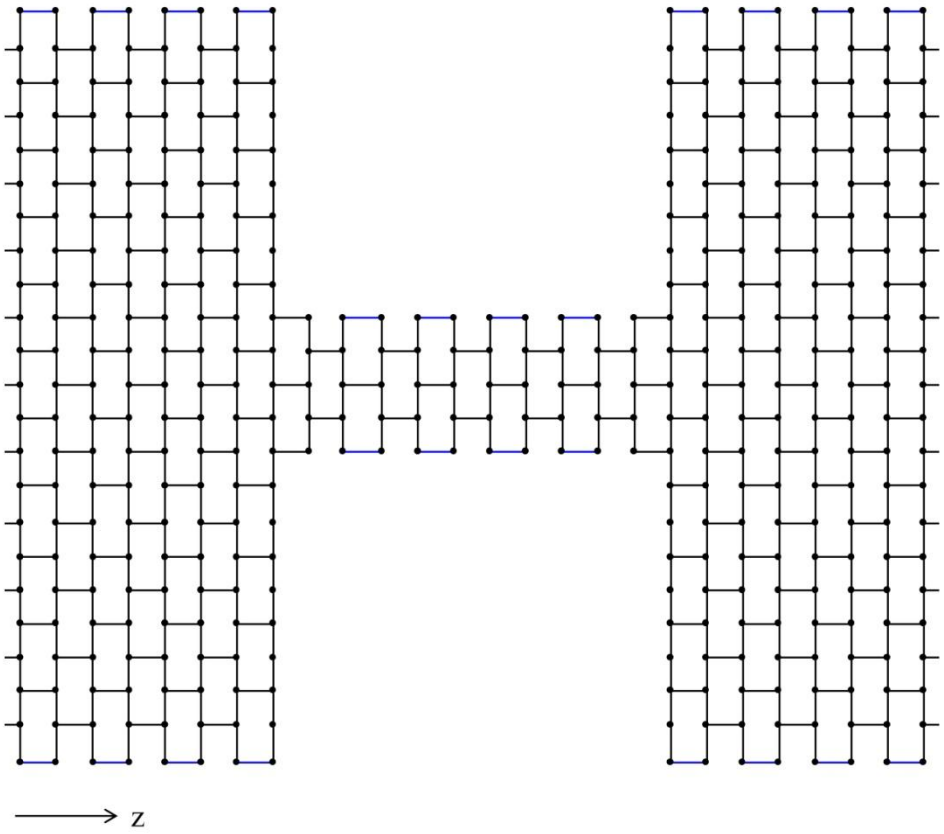

Fig. 2.1 Ladder form representation of the 23-5-23-AGNR Z-Z junction under periodic boundary condition. Each point represents an atomic site and each horizontal or vertical segment between the atomic sites represents the coupling between nearest neighbours.

In fully relaxed graphene structures, the bond lengths at the armchair edge (blue bonds in Fig. 2.1) are shorter than bond lengths at the inner region by 3.5%, which is energetically favourable due to the Peierls' distortion effect [12]. This 3.5% shortage in bond length corresponds to a 12% increase in hopping integral. The TB Hamiltonian can easily take this edge deformation effect into account by using a slightly larger

hopping integral of $-2.7\text{eV} \times (1 + 12\%) = -3.024$ eV between atoms at the armchair edge.

2.2 Density Functional Theory

Many of the properties of atoms, molecules, and solids may be understood by solving the time-independent Schrödinger equation

$$\hat{H}\Psi = E\Psi \qquad (2.5)$$

where the non-relativistic many-body Hamiltonian can be represented by five terms:

$$\begin{aligned}\hat{H} &= \hat{T}_n(r_\alpha) + \hat{T}_e(r_i) + \hat{V}_{en}(r_i, r_\alpha) + \hat{V}_{nn}(r_\alpha) + \hat{V}_{ee}(r_i) \\ &= -\sum_\alpha \frac{\hbar^2}{2m_\alpha}\nabla_\alpha^2 - \frac{\hbar^2}{2m}\sum_i \nabla_i^2 - \sum_i \sum_\alpha \frac{Z_\alpha e^2}{4\pi\varepsilon_0 |r_i - r_\alpha|} \\ &+ \sum_\alpha \sum_{\beta<\alpha} \frac{Z_\alpha Z_\beta e^2}{4\pi\epsilon_0 |r_\alpha - r_\beta|} + \sum_i \sum_{j<i} \frac{e^2}{4\pi\varepsilon_0 |r_i - r_j|} \qquad (2.6)\end{aligned}$$

The indices α, β run over the nuclei, and i, j run over the electrons. Z_α is the nuclear number, e is the elementary charge, and m_α and m are the masses of the nuclei and electrons respectively.

Solving Eqn. (2.6) for a system of many particles is intractable in practice. Fortunately, many approximations are proposed to reduce the many-body problem to a single-particle one, the first of which is the Born-Oppenheimer approximation.

2.2.1 The Born-Oppenheimer Approximation

Since nuclei are thousands of times more massive than electrons, they are nearly fixed with respect to electron motion. The wavefunction can thus be separated as

$$\Psi(r_i, r_\alpha) = \psi(r_i; r_\alpha)\Phi(r_\alpha) \qquad (2.7)$$

In this frozen nuclei approach, the electronic wavefunction $\psi(r_i; r_\alpha)$ depends only parametrically on the nuclear coordinates r_α, and satisfies the Schrödinger equation for electrons

$$\left[-\frac{\hbar^2}{2m}\sum_i \nabla_i^2 - \sum_i \sum_\alpha \frac{Z_\alpha e^2}{4\pi\varepsilon_0 |r_i - r_\alpha|} + \sum_i \sum_{j<i} \frac{e^2}{4\pi\varepsilon_0 |r_i - r_j|}\right] \psi(r_i; r_\alpha) = E(r_\alpha)\psi(r_i; r_\alpha) \qquad (2.8)$$

whereas $\Phi(r_\alpha)$ is a wavefunction of the nuclear coordinates only and satisfies

$$\left[-\sum_\beta \frac{\hbar^2}{2m_\beta}\nabla_\beta^2 + \sum_\beta \sum_{\gamma<\beta} \frac{Z_\beta Z_\gamma e^2}{4\pi\epsilon_0 |r_\beta - r_\gamma|} + E(r_\alpha)\right] \Phi(r_\alpha) = \varepsilon\Phi(r_\alpha) \qquad (2.9)$$

After adopting the Born-Oppenheimer approximation, the many-body problem is reduced to the solution of the dynamic electrons in the background of frozen nuclei. This however is still difficult to solve. Many approaches can further reduce the equation to a single electron scenario, such as the Hartree Fock approximation and density functional theory.

2.2.2 Density Functional Theory

Density functional theory (DFT) describes the properties of the system using functionals that only depend on the electron density $n(r)$. For a system with N_e electrons, the density is defined as:

$$n(r) = \langle\psi| \sum_i^{N_e} \delta(r - r_i) |\psi\rangle = N_e \int \left|\psi\left(r, r_2 \cdots, r_{N_e}\right)\right|^2 dr_2 \cdots dr_{N_e} \qquad (2.10)$$

where the density is normalized according to

$$\int n(r) dr = N_e \qquad (2.11)$$

Let us consider the electronic part of the Schrödinger equation (2.8) again, with the Hamiltonian written here in atomic units:

$$\hat{H}_e = \hat{T} + \hat{V}_{en} + \hat{V}_{ee} = -\frac{1}{2}\sum_i \nabla_i^2 - \sum_\alpha \sum_i \frac{Z_\alpha}{|r_i - r_\alpha|} + \sum_i \sum_{j<i} \frac{1}{|r_i - r_j|} \qquad (2.12)$$

Let us first start by calculating the expectation value of $\hat{V}_{en}$

$$E_{en} = \langle \psi(r_1, \cdots, r_N) | \hat{V}_{en} | \psi(r_1, \cdots, r_N) \rangle$$

$$= -\sum_\alpha^{N_n} \sum_i^{N_e} \int \frac{Z_\alpha}{|r_i - r_\alpha|} |\psi(r_1 \cdots, r_{N_e})|^2 dr_1 \cdots dr_{N_e} \qquad (2.13)$$

We can then expand the sum over the electronic index *i* and separate the integral over the variable in the Columbic terms from the others

$$E_{en} = -\sum_\alpha^{N_n} \begin{bmatrix} \int \frac{Z_\alpha}{|r_1 - r_\alpha|} dr_1 \int |\psi(r_1 \cdots, r_N)|^2 dr_2 dr_3 \cdots dr_N \\ + \int \frac{Z_\alpha}{|r_2 - r_\alpha|} dr_2 \int |\psi(r_1 \cdots, r_N)|^2 dr_1 dr_3 \cdots dr_N + \cdots \end{bmatrix} \qquad (2.14)$$

For each term in Eqn. (2.14), the second integral is equal to the electron density as defined in Eqn. (2.10), differing by a factor of $1/N_e$. By changing the variable of integration and summing over the term, the electron-nucleus energy can be written as

$$E_{en} = -\sum_\alpha^{N_n} \int n(r) \frac{Z_\alpha}{|r - r_\alpha|} dr = \int n(r) V_{en}(r) dr \qquad (2.15)$$

This linear functional form E_{en} can be extended to E_{ext} that includes any single-body external potential terms such as an applied electric field.

Using the same derivation technique for the electron-electron interaction,

$$E_{ee} = \frac{1}{2} \iint \frac{n^{(2)}(r, r')}{|r - r'|} dr dr' \qquad (2.16)$$

where $n^{(2)}(r,r')$ is the two-particle density. We can write this term as the product of one-electron densities plus an unknown correction term that arises from electron correlations:

$$n^{(2)}(r,r') = n(r)n(r) + \Delta n^{(2)}(r,r') \qquad (2.17)$$

The electron-electron interaction energy can now be written as

$$E_{ee} = \frac{1}{2}\iint \frac{n(r)n(r')}{|r-r'|}drdr' + \Delta E_{ee} \qquad (2.18)$$

The first term is known as the Hartree energy, and the correction term is generally non-negligible.

In order to approximate the kinetic energy term, we have to introduce the Kohn-Sham orbitals ϕ_i, defined as single-particle orbitals whose collective ground-state density is the same as the real system.

$$n(r) = \sum_{i}^{N^e} |\phi_i(r)|^2 \qquad (2.19)$$

The kinetic energy T can then be written as the kinetic energy of the Kohn-Sham orbitals plus a correction

$$T = \frac{1}{2}\sum_{i}^{N_e} \int \phi_i^*(r)\nabla^2\phi_i(r)dr + \Delta T \qquad (2.20)$$

While the kinetic energy cannot be differentiated directly with respect to the density $n(r)$ it can be minimized with respect to the orbitals $\phi_i(r)$ which is equivalent to minimizing with respect to $n(r)$.

The sum of the two unknown terms ΔE_{ee} and ΔT is called the exchange-correlation energy E_{ex}. It plays crucial role in DFT and we will later introduce some approximations to this term. The total energy as a functional of $n(r)$ can now be written as

$$E[n] = T[n] + E_{ext}[n] + E_H[n] + E_{xc}$$

$$= \frac{1}{2}\sum_{i}^{N_e}\int [\phi_i^*(r)\nabla^2\phi_i(r) + n(r)V_{ext}(r)]dr + \frac{1}{2}\iint \frac{n(r)n(r')}{|r-r'|}drdr' + E_{xc} \qquad (2.21)$$

2.2.3 The Hohenberg-Kohn theorems

Before introducing the Kohn-Sham equations, we will first prove two theorems put forward by Hohenberg and Kohn in 1964 [74] that made DFT possible. The first theorem legitimizes the use of electron density as a variable instead of wavefunctions.

Theorem 1. *The external potential $V_{ext}(r)$ is a unique functional of the ground state electron density $n_0(r)$.*

Proof. Assume that there exist two external potentials $V(r)$ and $V'(r)$ differing by more than a trivial constant, that result in the same ground state electron density, $n_0(r)$. Let their distinct Hamiltonians be $\hat{H}$ and $\hat{H}'$ and the wavefunctions ψ and ψ', respectrively. Due to the variational principle, the ground state energies satisfy the following inequalities:

$$E_0 = \langle\psi|\hat{H}|\psi\rangle < \langle\psi'|\hat{H}|\psi'\rangle = \langle\psi'|\hat{H}'|\psi'\rangle + \langle\psi'|\big(V(r) - V'(r)\big)|\psi'\rangle$$

$$= E_0' + \int (V(r) - V'(r))\, n_0(r)dr \qquad (2.22)$$

and

$$E_0' = \langle \psi' | \hat{H}' | \psi' \rangle < \langle \psi | \hat{H}' | \psi \rangle = \langle \psi | \hat{H} | \psi \rangle + \langle \psi | \big(V'(r) - V(r) \big) | \psi \rangle$$

$$= E_0 + \int (V'(r) - V(r))\, n_0(r) dr \qquad (2.23)$$

Adding Eqns. (2.22) and (2.23), we obtain

$$E_0 + E_0' < E_0' + E_0 \qquad (2.24)$$

which is clearly a contradiction. Hence the theorem is proven by *reduction ad absurdum*.

The second theorem provides the energy variation principle.

Theorem 2. *A universal functional for the energy E_n can be defined in terms of the electron density. The exact ground state is the global minimum value of this functional.*

Proof. The ground state energy is determined uniquely by the ground state density, $n(r)$. A different density, $n'(r)$ will necessarily give a higher energy by variational principle

$$E_0 = E[n(r)] = \langle \psi | \hat{H} | \psi \rangle < \langle \psi' | \hat{H} | \psi' \rangle = E' \qquad (2.25)$$

It follows that the electron density that minimized the energy is then the ground state density.

2.2.4 The Kohn-Sham Equations

Using the Hohenberg-Kohn theorem, the ground-state electron density is the density that minimizes the energy functional $E[n]$ (defined in equation (2.21)) with the normalizing constraint equation (2.11) that the total number of electrons is conserved. Mathematically,

$$\delta[E[n] + \mu(\int n(r)\, dr - N)] = 0 \quad (2.26)$$

where μ is the Lagrangian multiplier. If we define an effective potential that is the functional derivative of all the energy terms in equation (2.21), that is

$$V_{effective}\,(r) = \frac{\delta}{\delta n(r)}[E_{ext} + E_H + E_{xc}]$$

$$= V_{ext} + \int \frac{n(r)}{|r - r'|}\, dr + \frac{\delta E_{xc}}{\delta n(r)} = V_{ext} + V_H + V_{xc} \quad (2.27)$$

We can obtain the Euler equation from Eqn. (2.26) as

$$\frac{\delta T[n]}{\delta n(r)} + V_{effective} = \mu \quad (2.28)$$

Equation (2.28) is precisely the same equation obtained for a system of non-interacting electrons moving in an external potential. Hence for a given external potential $V_{effective}$, to find the ground-state density $n(r)$ that satisfies equation (2.28), we simply solve the one-electron Schrödinger equations

$$[\hat{T} + V_{effective}]\phi_i(r) = \varepsilon_i \phi_i(r) \quad (2.29)$$

Hence, eqns. (2.27), (2.19), and (2.29) can be solved consistently.

The total energy of the system can be computed using the following flow-chart Fig. 2.2 .

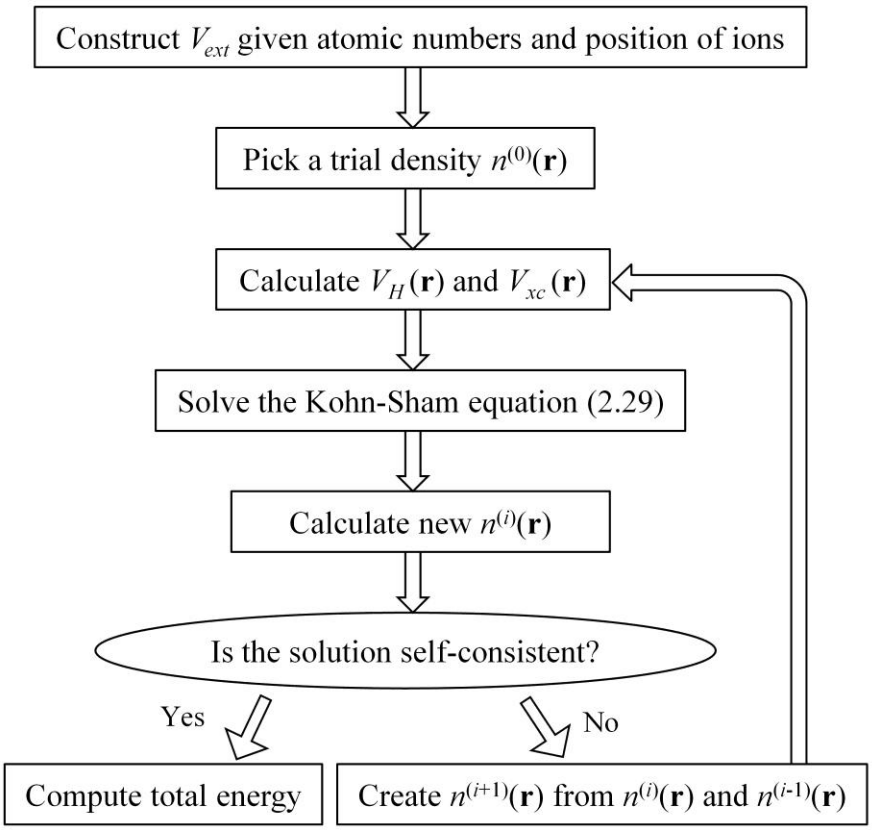

Fig. 2.2 Self-consistent procedures for the calculation of total energy using DFT.

2.2.5 Local Density Approximation

While the exact functionals for the exchange and correlation are not known in general, there are several approximations that reproduce certain physical quantities quite accurately. The simplest one is the local density approximation (LDA), which assumes that the exchange correlation energy per electron $\varepsilon_{xc}(n(r))$ is equal to that of a homogeneous electron gas that has the same density at the same point *r*. Therefore,

$$E_{xc}^{LDA} = \int n(r)\varepsilon_{xc}^{hom}(n(r))dr \qquad (2.30)$$

LDA assumes that the exchange-correlation energy functional is purely local, hence ignoring corrections to the E_{xc} due to nearby inhomogenities in $n(r)$. It is herefore very surprising that calculations performed using LDA have been so successful. This is partially due to the fact that the LDA gives the correct sum rule to the exchange

correlation, whereas it typically overestimates exchange E_x and underestimates correlation E_c. We shall employ LDA, and the spin-polarized version throughout the calculations.

2.2.6 Local Spin Density Approximation

The extension of LDA to spin polarized systems is straightforward. Firstly we can define electron densities for the spin-up and spin-down states as :

$$n^{\uparrow}(r) = \sum_{i=1}^{N^{\uparrow}} \left|\psi_i^{\uparrow}(r)\right|^2,$$

$$n^{\downarrow}(r) = \sum_{i=1}^{N^{\downarrow}} \left|\psi_i^{\downarrow}(r)\right|^2 \qquad (2.31)$$

And we can introduce the total charge and magnetization:

$$n(r) = n^{\uparrow}(r) + n^{\downarrow}(r), \quad m(r) = n^{\uparrow}(r) - n^{\downarrow}(r), \qquad (2.32)$$

The quantization axis is usually chosen as the z axis.

The total energy is now a functional of the up and down charge densities, but more conveniently expressed in terms of n and m:

$$E[n, m] = T + E_{ext} + E_H + E_{xc}[n, m] \qquad (2.33)$$

We can now exploit the properties

$$\frac{\delta n(r)}{\delta n^{\uparrow}(r')} = \frac{\delta n(r)}{\delta n^{\downarrow}(r')} = \delta(r - r'), \frac{\delta m(r)}{\delta n^{\uparrow}(r')} = \delta(r - r'), \frac{\delta m(r)}{\delta n^{\downarrow}(r')} = -\delta(r - r') \qquad (2.34)$$

And calculate the functional derivatives to get the Hamiltonian. The Kohn-Sham equations become

$$\left[-\frac{\hbar^2}{2m}\nabla^2 + V_{ext} + V_H + V_{xc} + B_{xc}\right]\psi_i^{\uparrow} = \varepsilon_i^{\uparrow}\psi_i^{\uparrow}$$

$$\left[-\frac{\hbar^2}{2m}\nabla^2 + V_{ext} + V_H + V_{xc} - B_{xc}\right]\psi_i^{\downarrow} = \varepsilon_i^{\downarrow}\psi_i^{\downarrow}$$

where

$$V_{xc}(r) = \frac{\delta E_{xc}[n,m]}{\delta n(r)}, \quad B_{xc}(r) = \frac{\delta E_{xc}[n,m]}{\delta m(r)} \qquad (2.35)$$

Magnetism stems from the exchange-correlation functional, where one spin is more energetically favourable than the other (as under a magnetic field). This is called the local spin-density approximation, or LSDA. The spin-polarized exchange functional is obtained from the unpolarized case as

$$E_x^{LSDA}[r] = \sum_{\sigma=\uparrow,\downarrow}\int \varepsilon_x^{LSDA}[n^{\sigma}(r)]dr = \sum_{\sigma=\uparrow,\downarrow}\int \frac{1}{2}\varepsilon_x^{LSDA}[2n^{\sigma}(r)]dr \qquad (2.36)$$

where

$$E_x^{LSDA}[r] = \int \varepsilon_x^{LSDA}[n(r)]dr \qquad (2.37)$$

The correlation functional can be obtained from the interpolation of polarized and unpolarized functionals:

$$E_c^{LSDA}[n,m] = \int\left[\varepsilon_c^{U}[n(r)] + f\big(\zeta(r)\big)(\varepsilon_c^{P}[n(r)] - \varepsilon_c^{U}[n(r)])\right]n(r)dr \qquad (2.38)$$

where f is a smooth interpolating function of the polarization

$$\zeta = \frac{m(r)}{n(r)} = \frac{n^{\uparrow}(r') - n^{\downarrow}(r')}{n^{\uparrow}(r') + n^{\downarrow}(r')} \qquad (2.39)$$

2.2.7 Implementation of DFT on this Project

In this Ph.D project, we use the DFT implemented in the Spanish Initiative for Electronic Simulations with Thousands of Atoms (SIESTA) [75], which utilizes

atomic-orbitals as basis-set. We use a double-ζ basis-set, which we have tested to be accurate enough for carbon systems. We use the LDA for the exchange-correlation functional. All edge carbon atoms in the graphene structures are passviated with a H atom and the structure is fully relaxed until the forces on atoms are less than 0.01 eV/Å.

2.3 Electrical Transport Calculation

In each step of the self-consistent calculation within DFT, a standard procedure to solve the Kohn-Sham equation and obtain the electron density $n(r)$ is to project the equation into a set of basis functions ϕ_i, thus transforming it into a matrix eigenvalue problem (see Section 2.1, especially Eqns. (2.1) to (2.3), for more details)

$$\sum_j (H_{ij} - ES_{ij})c_j = 0 \quad (2.40)$$

where $H_{ij} = \langle \phi_i | H | \phi_j \rangle$ and $S_{ij} = \langle \phi_i | \phi_j \rangle$.

For an isolated system or a unit cell of a periodic system, the Hamiltonian matrix is finite, thus solvable via standard linear algebra packages.

However, when we probe the transport property of a nanostructure, we need at least two semi-infinite leads connected to the nanostructure, as illustrated in Fig. 2.3. One lead is put at a lower chemical potential μ_1 while the other is put at a higher chemical potential μ_2, so that electrons will be driven by the bias voltage $V_b = (\mu_1 - \mu_2)/e$ to transport from one lead to the other. For such an open system, the reduction of system size is less obvious. The trick here is to separate the system into two lead regions and a central region, so that we can solve the Hamiltonian for the leads as bulks, and then use these solutions as matching boundary conditions for the central region. The central region should include large enough parts of the leads to screen the effects from

presence of the surfaces of the leads, the nanostructure, and the voltage drop, so that the remaining lead regions outside the central region could be in the same situation as in an equivalent bulk.

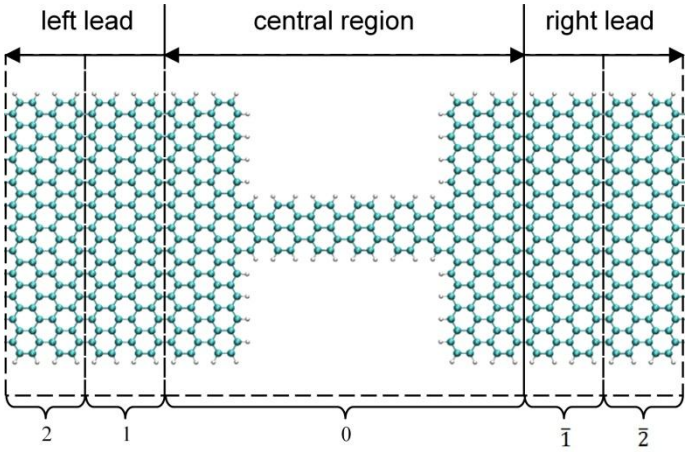

Fig. 2.3 An example of the 2-lead system: a 5-AGNR segment coupled seamlessly to two semi-infinite 23-AGNR leads. The regions 0, 1 ($\bar{1}$), and 2 ($\bar{2}$) represent the central region, the intermediate region and the bulk region on the left (right) side.

Here, we describe two approaches in obtaining the electron density $n(\boldsymbol{r})$ in the central region of a 2-leads system: the scattering-state approach and the non-equilibrium Green's function (NEGF) approach.

2.3.1 The Scattering-State Approach

The scattering-state approach [76] directly calculates all the eigenstates of the 2-leads system, and integrate all the occupied scattering and bound states up to the chemical potentials μ_1 and μ_2 to obtain $n(\boldsymbol{r})$ as:

$$n(\boldsymbol{r}) =$$

$$2\int_{-\infty}^{\mu_1} dE \sum_{k,\boldsymbol{k}_{||}} \left|\psi_{k,\boldsymbol{k}_{||}}^{(L)}(\boldsymbol{r},E)\right|^2 D_{k,\boldsymbol{k}_{||}}^{(L)}(E) +$$

$$2\int_{-\infty}^{\mu_2} dE \sum_{k,\boldsymbol{k}_{||}} \left|\psi_{k,\boldsymbol{k}_{||}}^{(R)}(\boldsymbol{r},E)\right|^2 D_{k,\boldsymbol{k}_{||}}^{(R)}(E) + 2\sum_{E_b}|\psi_b(\boldsymbol{r},E_b)|^2 f(E_b) \qquad (2.41)$$

Here, the factor 2 accounts for the number of spins, $D^{(L)}_{k,\boldsymbol{k}_{||}}(E)$ ($D^{(R)}_{k,\boldsymbol{k}_{||}}(E)$) is the density of states per spin in the left (right) lead, and $f(E_b)$ is the occupation number of the bound state ψ_b at energy E_b.

In principle, the scattering-states can be obtained in a similar way as calculating the transmission probability of a square potential barrier, as described in many textbooks (e.g. [77]). Namely, we first solve different regions separately to obtain general solutions, then determine the final solution by letting wavefunctions match at the interfaces between different regions.

The situation in a real nanostructure with two leads is more complicated because of the many unknown potential terms arising from all the nuclei and electrons in the system, which we have to determine self-consistently using DFT. We divide the 2-leads system into 5 regions as shown in Fig. 2.3: the central region that contains the nanostructure and enough parts of the leads (region 0), two intermediate regions that are the first unit cells of the leads (regions 1 and $\bar{1}$), and two semi-infinite bulk regions (regions u and $\bar{u}$, with u = 2, 3, 4, …).

As the first step, we solve each lead using standard DFT calculations by considering only one unit cell (2 or $\bar{2}$) under periodic boundary condition, and obtain all eigenwavefunctions at each energy E of a continuous energy spectrum. Each eigenwavefunction is in the form of a linear combination of the N_1 atomic basis-functions within one unit cell, with all the coefficients constituting a vector ($c_1^{(2)}$, $c_2^{(2)}$, … , $c_j^{(2)}$, …, $c_{N_1}^{(2)}$) or ($c_1^{(\bar{2})}$, $c_2^{(\bar{2})}$, …, $c_j^{(\bar{2})}$, … , $c_{N_1}^{(\bar{2})}$).

Then, we use the solutions of the leads to calculate the central and intermediate regions. The matrix form Kohn-Sham equation for the central and intermediate regions are

$$\sum_{j=1}^{N_0} \mathcal{H}_{ij}^{(00)} c_j^{(0)} + \sum_{j=1}^{N_1} \mathcal{H}_{ij}^{(01)} c_j^{(1)} + \sum_{j=1}^{N_{\bar{1}}} \mathcal{H}_{ij}^{(0\bar{1})} c_j^{(\bar{1})} = 0 \quad (2.42a)$$

for the i^{th} orbital ($1 \leq i \leq N_0$) in the central region,

$$\sum_{j=1}^{N_0} \mathcal{H}_{ij}^{(10)} c_j^{(0)} + \sum_{j=1}^{N_1} \mathcal{H}_{ij}^{(11)} c_j^{(1)} + \sum_{j=1}^{N_1} \mathcal{H}_{ij}^{(12)} c_j^{(2)} = 0 \quad (2.42b)$$

for the i^{th} orbital ($1 \leq i \leq N_1$) in the intermediate region on the left side, and

$$\sum_{j=1}^{N_0} \mathcal{H}_{ij}^{(\bar{1}0)} c_j^{(0)} + \sum_{j=1}^{N_{\bar{1}}} \mathcal{H}_{ij}^{(\bar{1}\bar{1})} c_j^{(\bar{1})} + \sum_{j=1}^{N_{\bar{1}}} \mathcal{H}_{ij}^{(\bar{1}\bar{2})} c_j^{(\bar{2})} = 0 \quad (2.42c)$$

for the i^{th} orbital ($1 \leq i \leq N_{\bar{1}}$) in the intermediate region on the right side. Here,

$$\mathcal{H}_{ij}^{(xy)} = \sum_{\boldsymbol{R}_{||}} e^{i\boldsymbol{k}_{||}\boldsymbol{R}_{||}} \left\langle i, x, \mathbf{0} \middle| \hat{H} - E \middle| j, y, \boldsymbol{R}_{||} \right\rangle \quad (2.43)$$

represents the interaction between the i^{th} orbital in the unit cell $\mathbf{0}$ of region x and the j^{th} orbital in the unit cell $\boldsymbol{R}_{||}$ of region y, and $c_j^{(x)}$ represent the coefficient of the j^{th} orbital in region x.

The effects from the leads are involved in the terms $\sum_{j=1}^{N_1} \mathcal{H}_{ij}^{(12)} c_j^{(2)}$ and $\sum_{j=1}^{N_{\bar{1}}} \mathcal{H}_{ij}^{(\bar{1}\bar{2})} c_j^{(\bar{2})}$, where $c_j^{(2)}$ and $c_j^{(\bar{2})}$ are known from solutions of the leads. We are left with only $N_0 + N_1 + N_{\bar{1}}$ undetermined coefficients, which is same as the total number of equations. Given all the potential terms in $\mathcal{H}_{ij}^{(xy)}$, we can solve these $N_0 + N_1 + N_{\bar{1}}$ equations to obtain the coefficients on the $N_0 + N_1 + N_{\bar{1}}$ atoms in the resistive and intermediate regions.

All the $N_0 + 2N_1 + 2N_{\bar{1}}$ coefficients together form the scattering-state $\psi^{(L)}_{k,\boldsymbol{k}_{||}}(\boldsymbol{r}, E)$ or $\psi^{(R)}_{k,\boldsymbol{k}_{||}}(\boldsymbol{r}, E)$, representing a wavefunction coming from the Left or Right lead at energy E, with a wave number k in the transport dimension and a wave vector $\boldsymbol{k}_{||}$ in the transverse dimension. Besides these scattering-states coming from one lead, there may also exists bound states $\psi_b(\boldsymbol{r}, E_b)$ within the central region. Such states can be solved by letting $c_j^{(2)} = c_j^{(\bar{2})} = 0$ in Eqn. (2.42).

After obtaining all the scattering-states and bound states, we then use Eqn. (2.41) to obtain the electron density $n(\boldsymbol{r})$. After that, we calculate effective potential in $\mathcal{H}_{ij}^{(xy)}$ from $n(\boldsymbol{r})$ and go to the next loop of the self-consistent calculation until convergence is reached. In particular, the Hartree potential in the central region is uniquely determined by the Poisson equation inside the region and the values on the boundary planes between the central region and the intermediate regions. The Hartree potentials inside the intermediate and bulk regions are obtained from the separate lead calculations. Note that the central region has to contain large enough parts of the leads so that voltage drop occurs within the central region.

Once self-consistence is reached, we can determine the transmission probability $T(E, k, \boldsymbol{k}_{||}, V_b)$ from the scattering-states, and integrate all the transmission probabilities within the voltage bias to obtain the current

$$I(V_b) = \frac{2|e|}{h} \int_{\mu_1}^{\mu_2} \langle T(E, \boldsymbol{k}_{||}, V_b) \rangle dE$$

where $\langle T(E, \boldsymbol{k}_{||}, V_b) \rangle$ represents the average over k. The flow chart of this scattering-state calculation is shown in Fig. 2.4.

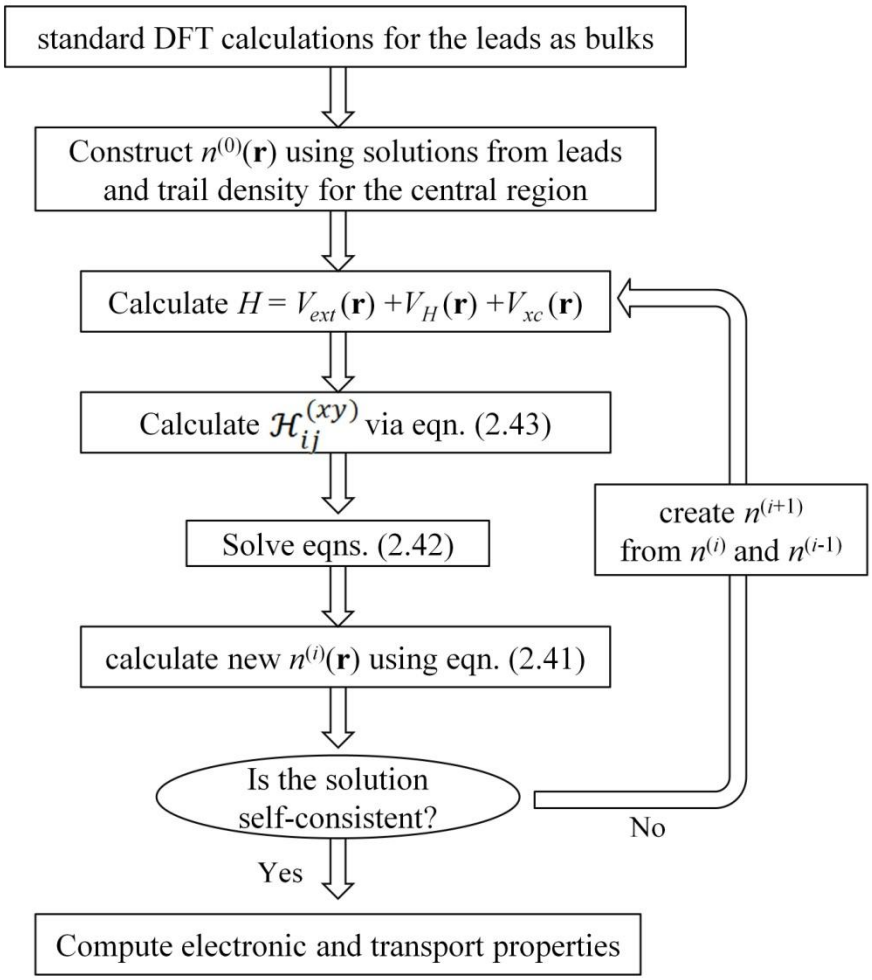

Fig. 2.4 Flow chart for the DFT self-consistent calculation of a 2-lead system from the Scattering-State approach.

This scattering-state approach can be implemented in any localized-orbital-based DFT code. For calculations in the present thesis, we have used this method as implemented in SCARLET [76].

2.3.2 Non-Equilibrium Green's Function

Instead of calculating the scattering-states, the non-equilibrium green's function method obtains the electron density $n(\boldsymbol{r})$ from the spectral-density operator [78]

$$\hat{\rho}(\varepsilon) \equiv \delta(\varepsilon - \hat{H}) \qquad (2.44a)$$

By integrating $\hat{\rho}(E)$ over all occupied energies, we obtain the total density

$$\widehat{D} = \int_{-\infty}^{\infty} \hat{\rho}(\varepsilon) f(\varepsilon - \mu) d\varepsilon \quad (2.44b)$$

where f is the Fermi distribution function and μ is the chemical potential of the system. Then the spatial electron density $n(\boldsymbol{r})$ can be evaluated by taking the trace of the density matrix $\widehat{D}$ as

$$n(\boldsymbol{r}) = Tr\left(\widehat{D}\right) \quad (2.44c)$$

According to the Sokhotski-Plemelj theorem $Im(\frac{1}{x \pm i\delta_+}) = \mp\pi\delta(x)$ where δ_+ is an infinitesimal positive number [79, 80], the spectral density $\hat{\rho}(E)$ can be obtained from the (retarded) Green's function

$$\hat{G}(\varepsilon) = \frac{1}{\varepsilon - \widehat{H} + i\delta_+} \quad (2.45)$$

as

$$\hat{\rho}(\varepsilon) = -\frac{1}{\pi} Im\left(\hat{G}(\varepsilon)\right) \quad (2.46)$$

We transform Eqns. (2.45), (2.46), and (2.44) into matrix form by projecting the operators into basis functions $\{\phi_i(\boldsymbol{r})\}$.

$$\boldsymbol{G}(\varepsilon) = [(\varepsilon + i\delta_+)\boldsymbol{S} - \boldsymbol{H}]^{-1} \quad (2.47a)$$

$$\boldsymbol{\rho}(\varepsilon) = \frac{1}{\pi} Im(\boldsymbol{G}(\varepsilon)) \quad (2.47b)$$

$$\boldsymbol{D} = \int_{-\infty}^{\infty} \boldsymbol{\rho}(\varepsilon) f(\varepsilon - \mu) d\varepsilon \quad (2.47c)$$

$$n(\boldsymbol{r}) = \sum_{i,j} D_{i,j}\phi_i^*(\boldsymbol{r})\phi_j(\boldsymbol{r}) \qquad (2.47d)$$

where **S** represents an identity matrix. As the spectral-density $\boldsymbol{\rho}(\varepsilon)$ is usually a rapidly varying function along the axis ε, the integration in $(2.47c)$ over ε is replaced by an equivalent contour integration in the complex plane. The problem of calculating $n(\boldsymbol{r})$ now is converted to the matrix inversion in Eqn. (2.47a). Because the 2-lead system is infinite, the matrix to be inverted is also of infinite dimension. However, the electron density in the leads can be calculated separately as a standard DFT bulk calculation, and we only have to solve $n(\boldsymbol{r})$ in the central region. Since the basis functions $\{\phi_i(\boldsymbol{r})\}$ are localized, we only need to calculate a sub-matrix of the Green's function in the central region plus a few layers of the leads.

Self Energy

The Hamiltonian matrix for the whole 2-lead system can be written as

$$\boldsymbol{H} = \begin{pmatrix} \boldsymbol{H}_{LL} & \boldsymbol{H}_{LC} & \mathbf{0} \\ \boldsymbol{H}_{CL} & \boldsymbol{H}_{CC} & \boldsymbol{H}_{CR} \\ \mathbf{0} & \boldsymbol{H}_{RC} & \boldsymbol{H}_{RR} \end{pmatrix}$$

where the sub-matrixes $\boldsymbol{H}_{LL}$, $\boldsymbol{H}_{CC}$, $\boldsymbol{H}_{RR}$ represent the Hamiltonian for the left lead, the central region, and the right lead, respectively. $\boldsymbol{H}_{CL} = \boldsymbol{H}_{LC}{}^T$ and $\boldsymbol{H}_{CR} = \boldsymbol{H}_{RC}{}^T$ represent the coupling between the central region and the left or right lead.

If there were no interaction between the central region and the leads, the total Hamiltonian is block diagonal, and the unperturbed Green's functions will be

$$\boldsymbol{G}_{LL}^0 = [(\varepsilon + i\delta_+)\boldsymbol{S}_{LL} - \boldsymbol{H}_{LL}]^{-1}$$

$$\boldsymbol{G}_{CC}^0 = [(\varepsilon + i\delta_+)\boldsymbol{S}_{CC} - \boldsymbol{H}_{CC}]^{-1}$$

$$\boldsymbol{G}_{RR}^{0} = [(\varepsilon + i\delta_{+})\boldsymbol{S}_{RR} - \boldsymbol{H}_{RR}]^{-1}$$

From these unperturbed Green's functions, we can obtain the perturbed Green's function through the Dyson's equation

$$\boldsymbol{G}_{CC} = \boldsymbol{G}_{CC}^{0} + \boldsymbol{G}_{CC}^{0}[\boldsymbol{\Sigma}^{\mathrm{L}} + \boldsymbol{\Sigma}^{\mathrm{R}}]\boldsymbol{G}_{CC} \quad (2.48)$$

where $\boldsymbol{\Sigma}^{\mathrm{L}}$ and $\boldsymbol{\Sigma}^{\mathrm{R}}$ are the self energies of the two leads

$$\boldsymbol{\Sigma}^{\mathrm{L}} = \boldsymbol{H}_{CL}\boldsymbol{G}_{LL}^{0}\boldsymbol{H}_{CL}{}^{\dagger} \quad (2.49a)$$

$$\boldsymbol{\Sigma}^{\mathrm{R}} = \boldsymbol{H}_{CR}\boldsymbol{G}_{RR}^{0}\boldsymbol{H}_{CR}{}^{\dagger} \quad (2.49b)$$

We can solve Eqns. (2.47) and (2.48) to obtain [81, 82]

$$\boldsymbol{G}_{CC} = \left[(\varepsilon + i\delta_{+})\boldsymbol{S}_{CC} - \boldsymbol{H}_{CC} - \boldsymbol{H}_{CL}\boldsymbol{G}_{LL}^{0}\boldsymbol{H}_{CL}{}^{\dagger} - \boldsymbol{H}_{CR}\boldsymbol{G}_{RR}^{0}\boldsymbol{H}_{CR}{}^{\dagger}\right]^{-1} \quad (2.50)$$

Green's Functions of the Leads

In order to obtain $\boldsymbol{G}_{CC}$ according to Eqn. (2.49), we need to obtain the unperturbed Green's functions of the leads $\boldsymbol{G}_{LL}^{0}$ and $\boldsymbol{G}_{RR}^{0}$, which could not be obtained from matrix inversion because the corresponding Hamiltonians $\boldsymbol{H}_{LL}$ and $\boldsymbol{H}_{RR}$ are of infinite dimension. However, since the leads are periodic, $\boldsymbol{G}_{LL}^{0}$ and $\boldsymbol{G}_{RR}^{0}$ can be approximated using a recursive algorithm.

We divide the lead into unit cells R_1, R_2, R_3, …, of an appropriate size so that only neighboring unit cells can interact. Thus, the Hamiltonian $\boldsymbol{H}_{RR}$ could be written as periodic blocks along the diagonal

$$\boldsymbol{H}_{RR} = \begin{bmatrix} \boldsymbol{H}_{R_1R_1} & \boldsymbol{H}_{R_1R_2} & \mathbf{0} & \mathbf{0} & \mathbf{0} & \cdots \\ \boldsymbol{H}_{R_2R_1} & \boldsymbol{H}_{R_2R_2} & \boldsymbol{H}_{R_2R_3} & \mathbf{0} & \mathbf{0} & \cdots \\ \mathbf{0} & \boldsymbol{H}_{R_3R_2} & \boldsymbol{H}_{R_3R_3} & \boldsymbol{H}_{R_3R_4} & \mathbf{0} & \cdots \\ \mathbf{0} & \mathbf{0} & \boldsymbol{H}_{R_4R_3} & \boldsymbol{H}_{R_4R_4} & \boldsymbol{H}_{R_4R_5} & \cdots \\ \mathbf{0} & \mathbf{0} & \mathbf{0} & \boldsymbol{H}_{R_5R_4} & \boldsymbol{H}_{R_5R_5} & \cdots \\ \vdots & \vdots & \vdots & \vdots & \vdots & \ddots \end{bmatrix} \quad (2.51)$$

where $\boldsymbol{H}_{R_1R_1} = \boldsymbol{H}_{R_2R_2} = \boldsymbol{H}_{R_3R_3} = \cdots$ and $\boldsymbol{H}_{R_1R_2} = \boldsymbol{H}_{R_2R_3} = \cdots$ can be obtained by the separate lead calculation as a bulk.

We can then build up a recursive approximation of $\boldsymbol{G}^0_{RR}$ as

$$\mathbf{G}^0_{R_1R_1}{}^{[0]} = \left[(\varepsilon + i\delta_+)\boldsymbol{S}_{R_1R_1} - \boldsymbol{H}_{R_1R_1}\right]^{-1}$$

$$\mathbf{G}^0_{R_1R_1}{}^{[1]} = \left[(\varepsilon + i\delta_+)\boldsymbol{S}_{R_1R_1} - \boldsymbol{H}_{R_1R_1} - \boldsymbol{H}_{R_1R_2}\boldsymbol{G}^0_{R_2R_2}{}^{[0]}\boldsymbol{H}_{R_1R_2}{}^{\dagger}\right]^{-1}$$

$$\mathbf{G}^0_{R_1R_1}{}^{[2]} = \left[(\varepsilon + i\delta_+)\boldsymbol{S}_{R_1R_1} - \boldsymbol{H}_{R_1R_1} - \boldsymbol{H}_{R_1R_2}\boldsymbol{G}^0_{R_2R_2}{}^{[1]}\boldsymbol{H}_{R_1R_2}{}^{\dagger}\right]^{-1} \quad (2.52)$$

where the superscript $[n]$ represents the order of approximation. We can then solve the unperturbed Green's function of both leads recursively until it is converged.

Finite Bias

When a bias V_b is applied, the two leads will be at different chemical potentials μ_1 and μ_2. Assuming $\mu_1 < \mu_2$, we can divide the density matrix $\widehat{D}$ into an equilibrium part $\widehat{D}_{eq}$ with energies below both chemical potentials and a non-equilibrium part $\widehat{D}_{neq}$ with energy in-between the two chemical potentials

$$\widehat{D} = \widehat{D}_{eq} + \widehat{D}_{neq} \quad (2.53a)$$

$$\widehat{D}_{eq} = \int_{-\infty}^{\infty} \hat{\rho}(\varepsilon) f(\varepsilon - \mu_1) d\varepsilon \quad (2.53b)$$

$$\widehat{D}_{neq} = \int_{-\infty}^{\infty} \hat{\rho}^R(\varepsilon)[f(\varepsilon - \mu_2) - f(\varepsilon - \mu_1)]d\varepsilon \quad (2.53c)$$

Here, $\hat{\rho}^R(\varepsilon)$ represents the spectral-density contributed from the right lead. It can be obtained from the Green's function and the self energy of the right lead as [83, 84]

$$\hat{\rho}^R(\varepsilon) = -\hat{G}(\varepsilon) Im\hat{\Sigma}^R(\varepsilon)\hat{G}^\dagger(\varepsilon) \quad (2.54)$$

$\widehat{D}_{eq}$ can be calculated in the same way as for the case without bias voltage, where we can use the complex contour integration technique. However, $\hat{\rho}^R(\varepsilon)$ is not an analytical function, so the integral in Eqn. $(2.52c)$ can not be extended into the complex plane. It has to be calculated along the real ε axis, and a dense grid of energy points has to be used to account for the rapid variation of $\hat{\rho}^R(\varepsilon)$. For large bias, this real axis integration is the most time consuming part of the calculation.

Effective Potential and Self-Consistent Loop

So far, we have been discussing algorithms to calculate the electron density $\mathrm{n(r)}$ from the Hamiltonian H via Green's function approach in both zero bias and finite bias cases. The other half of one self-consistent loop is to calculate the Hamiltonian as a functional of the electron density $\mathrm{n(r)}$. Most terms in the Hamiltonian can be calculated following the standard procedures presented in Section 2.2 Density Function Theory. However, we need to take special consideration for the Hartree potential term (electrostatic potential from electron charge density), especially when a finite bias is applied. The Hartree potential is calculated from the Poisson's equation

$$\nabla^2 V_H(r) = -4\pi n(r) \quad (2.55)$$

Poisson's equation requires a boundary condition to fix the solutions, as it is a 2nd-order differential equation. For the lead calculations, we use periodic boundary conditions, which determines the Hartree potential with a floating additive constant. When a bias V_b is applied, we align the Hartree potential in the left and right lead with a difference of eV_b. The Hartree potentials in the two leads then define the boundary conditions to solve for the Hartree potential in the central region.

The self-consistent calculation combining NEGF and DFT to obtain the electronic structure of the 2-lead system can be summarized in the flowchart in Fig. 2.5.

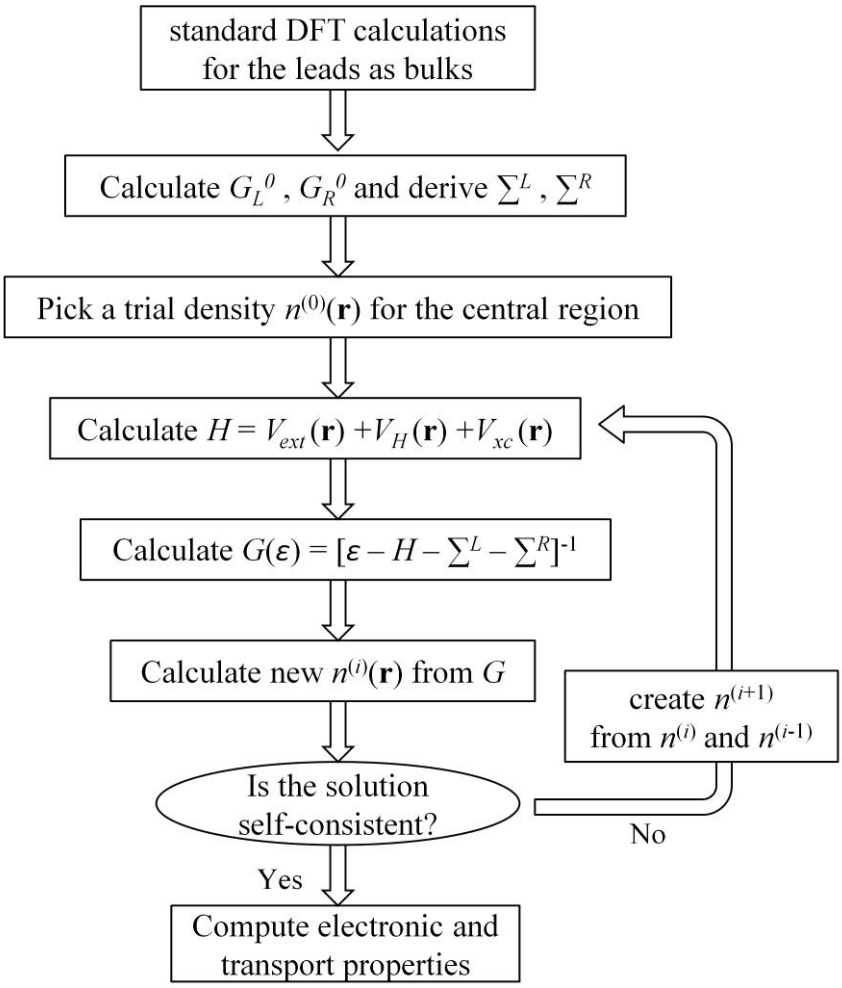

Fig. 2.5 Flow chart for the DFT-NEGF combined self-consistent calculation of a 2-lead system.

Transmission Probability and Current

Once self-consistency is reached, we can get the transmission probability from the Green's function as [81, 84]

$$T(\varepsilon) = Tr[Im\hat{\Sigma}^{L}(\varepsilon)\hat{G}^{\dagger}(\varepsilon)Im\hat{\Sigma}^{R}(\varepsilon)\hat{G}(\varepsilon)] \quad (2.56)$$

We can then calculate the current by integrating the transmission probability of all occupied states

$$I = \frac{2e}{h}\int_{-\infty}^{\infty} T(\varepsilon)(f(\varepsilon-\mu_1) - f(\varepsilon-\mu_2))d\varepsilon \quad (2.57)$$

This NEGF method has been implemented in many software packages, including McDCAL [85], TranSIESTA [83], and ATK. NEGF calculations in the present thesis are performed using TranSIESTA.

Chapter 3. Bandstructures and Wavefunctions in three Families of AGNRs

Before discussing the wide-narrow-wide-AGNR junction, we first present some results on the bandstructures and wavefunctions in three families of AGNRs. We will refer back to these results when we analyze the AGNR-junctions in later chapters.

As we have reviewed in Section 1.1, AGNRs are classified into three families according to its width n = 3p, 3p+1, or 3p+2. Tight-Binding calculations predict that 3p+2-AGNRs are metallic while 3p- and 3p+1-AGNRs are semiconducting. Such family behavior can be understood from the simple *quantization approach* [17] we reviewed in Section 1.1.1, where the transverse wavenumber is quantized into discrete values $k_\perp^p = 2p\pi/(n+1)a$. We can surmise the bandstructure of an n-AGNR as the projections of graphene bands onto these $k_\perp^p$ values. It happens that $k_\perp^p$ would cut through a Dirac point at $k_\perp = 2\pi/3a$ if $n = 3p + 2$, so 3p+2-AGNRs have no gap.

Later DFT calculations predicted an increase in the gaps for all three families of AGNRs, which means 3p+2-AGNRs become semiconducting too. Such increase of gap can be reproduced from an analytical Tight-Binding approach considering the edge deformation effect (Peierls' distortion effect) [12].

3.1 Double Bands in 3p+1-AGNRs

Figure 3.1 shows the DFT bandstructures of n-AGNRs with n = 3 to 14. We see obviously that the gaps of 3p+2-AGNRs are much smaller than that of 3p- and 3p+1-AGNRs. Within each family, the gap decreases with increasing ribbon width n,

consistent with previous studies. Focusing on the bands near the gap, we see another trend on both the occupied and the unoccupied side: *each 3p+1-AGNR has two bands at similar energies* (indicated by the red boxes in Fig. 3.1), *while each 3p- or 3p+2-AGNR has only one single band near* E_F. For description convenience, we refer to the two bands in each 3*p*+1-AGNR as *double bands*. To our knowledge, such double bands feature has neither been pointed out nor explained so far. Here, we explain this property from the *quantization approach* we introduced in Section 1.1.1.

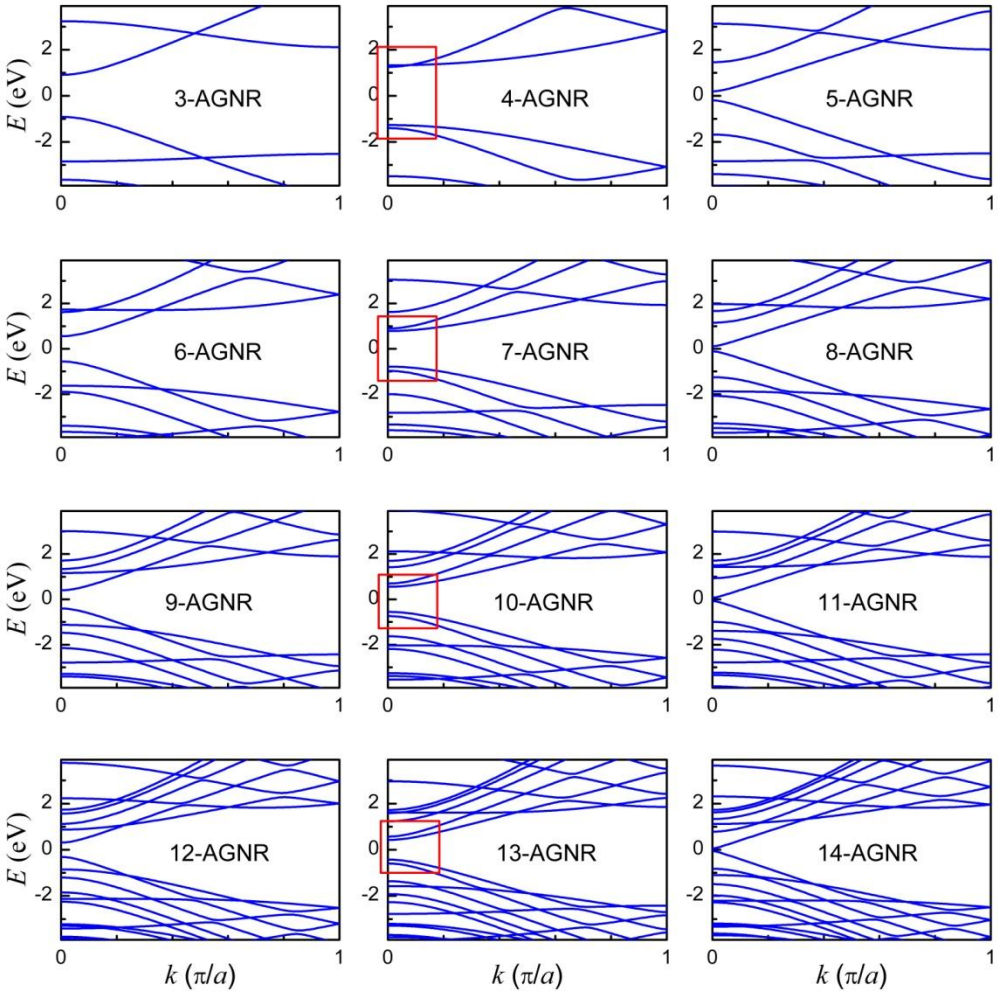

Fig. 3.1 Band structures of hydrogen passivated *n*-AGNRs with *n* varying from 3 to 14, obtained by DFT calculations implemented in ATK [75] with double-zeta polarized basis-set. The zero energy is set at Fermi level. The red boxes indicate the double bands in 3*p*+1-AGNRs.

3.2 Γ-point Wavefunctions of AGNRs

In order to find out the origin of each band near E_F, especially the double bands in 3*p*+1-AGNRs, we calculated the Γ-point eigenwavefunctions of these single or double bands, as visualized in Fig. 3.2. For description convenience, we refer to the **G**amma-point wavefunction **O**rbital of the **L**owest **U**noccupied band as **LUGO**, and the **G**amma-point wavefunction **O**rbital of the **H**ighest **O**ccupied band as **HOGO**. Accordingly, we refer to the Gamma-point wavefunction Orbital of the second, third, fourth, …, and n^{th} Lowest Unoccupied (Highest Occupied) band as LUGO+1 (HOGO-1), LUGO+2 (HOGO-2), LUGO+3 (HOGO-3), … , and LUGO+(*n*-1) (HOGO-(*n*-1)), respectively.

First of all, the AGNRs within the same family show similar wavefunction patterns. For example, the HOGOs and LUGOs of 3*p*+2-AGNRs all exhibit a "3*j*" pattern [8]: absence of wavefunction distribution on the $(3j)^{th}$ rows of carbon atoms, where *j* = positive integer (see Section 1.1.2 for details). Secondly, the HOGO-1 (LUGO+1) of 7-AGNR looks like two HOGOs (LUGOs) of 3-AGNR separated by an empty carbon row in the middle. The HOGO-1 (LUGO+1) of 13-AGNR also looks like two HOGOs (LUGOs) of 6-AGNR separated by an empty carbon row in the middle. This similarity implies that the second lowest unoccupied (second highest occupied) band in 3*p*+1-AGNRs could have similar a origin as the lowest unoccupied (highest occupied) band in 3*p*-ANGRs.

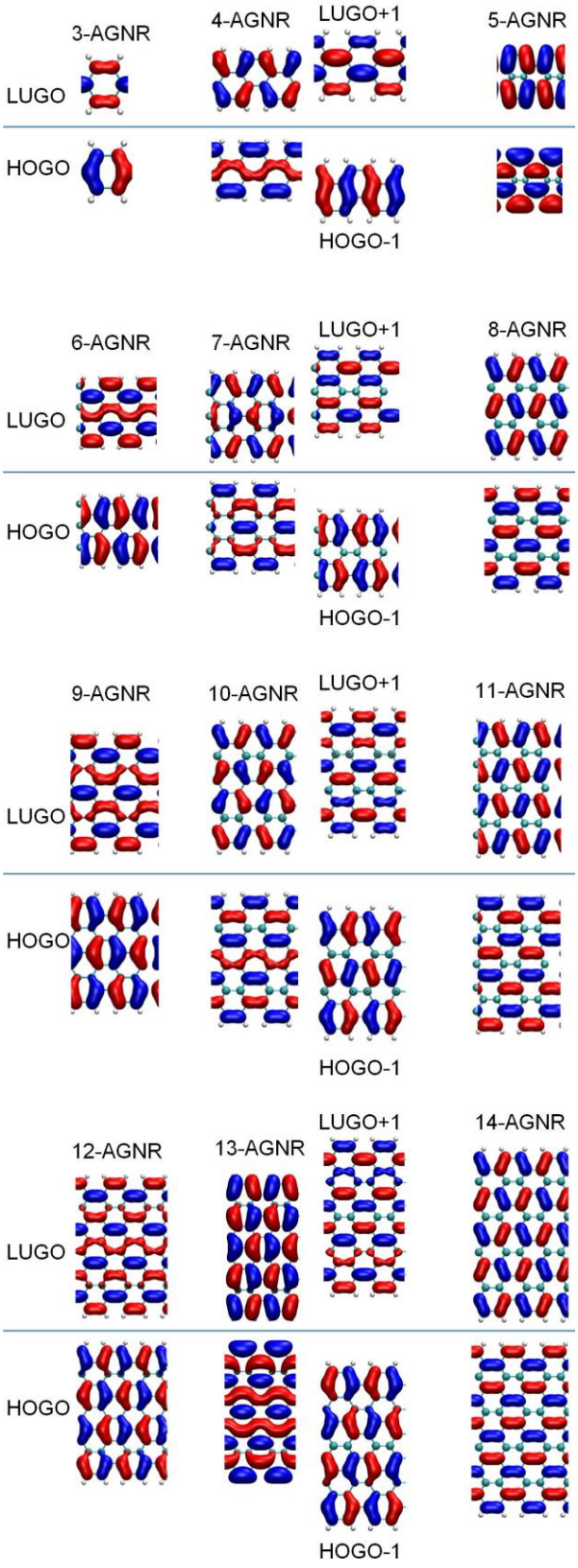

Fig. 3.2 The Γ-point eigenwavefunctions of AGNRs for the bands near the Fermi level. HOGO (LUGO) and HOGO-1 (LUGO+1) represent the Gamma-point wavefunction Orbital of the Highest Occupied (Lowest Unoccupied) and the second Highest

Occupied (Lowest Unoccupied) bands, respectively. The red and blue color represent positive and negative isosurfaces of the wavefunction, respectively.

3.3 Understanding from the Quantization Approach

Next, we examine the origin of each band of AGNRs in the 2D π- and π*-bands of graphene based on the quantization approach. We take 4-AGNR, 5-AGNR, and 6-AGNR as examples and indicate their unoccupied bands in Fig. 3.3 as horizontal lines slicing the 2D π*-band of graphene. 5-AGNR has a quantized $k_\perp$value ($k_\perp = 2\pi/3a$) slicing through the **K** point exactly, while 4-AGNR and 6-AGNR do not have any quantized $k_\perp$value slicing through a Dirac point.

Since we are interested on bands near E_F, we focus on the region near **K** point. For 4-AGNR, the two quantized $k_\perp$values nearest to **K** point are 3/15 and 6/15 (in units of $2\pi/a$). One of them is below **K** point by 2/15, while the other is above **K** point by 1/15. In other words, the $k_\perp$ value below **K** point is two times further to **K** point than the $k_\perp$ value above **K** point. In fact, this is true for all 3*p*+1-AGNRs. A 3*p*+2-AGNR has a quantized $k_\perp = \frac{p+1}{(3p+2)+1} = 1/3$ cutting through the **K** point, but a 3*p*+1-AGNR has no such $k_\perp$ value cutting through any Dirac point. For a 3*p*+1-AGNR, the two quantized $k_\perp$ values nearest to **K** point are $\frac{p}{(3p+1)+1}$ and $\frac{p+1}{(3p+1)+1}$, the former one is below **K** point by $\frac{2p+2}{(3p+2)(3p+3)}$ while the latter one is above **K** point by $\frac{p+1}{(3p+2)(3p+3)}$. It is clear that the former one is two times further from **K** point than the later one.

On the other hand, the energy contours of graphene π*-band near **K** point are triangular, with the energy minimum located at the **K** point (Fig. 3.3). Due to this triangular shape, the energy contours are sparser below the **K** point and denser above the **K** point (looking along the vertical line with $k_{||} = 0$).

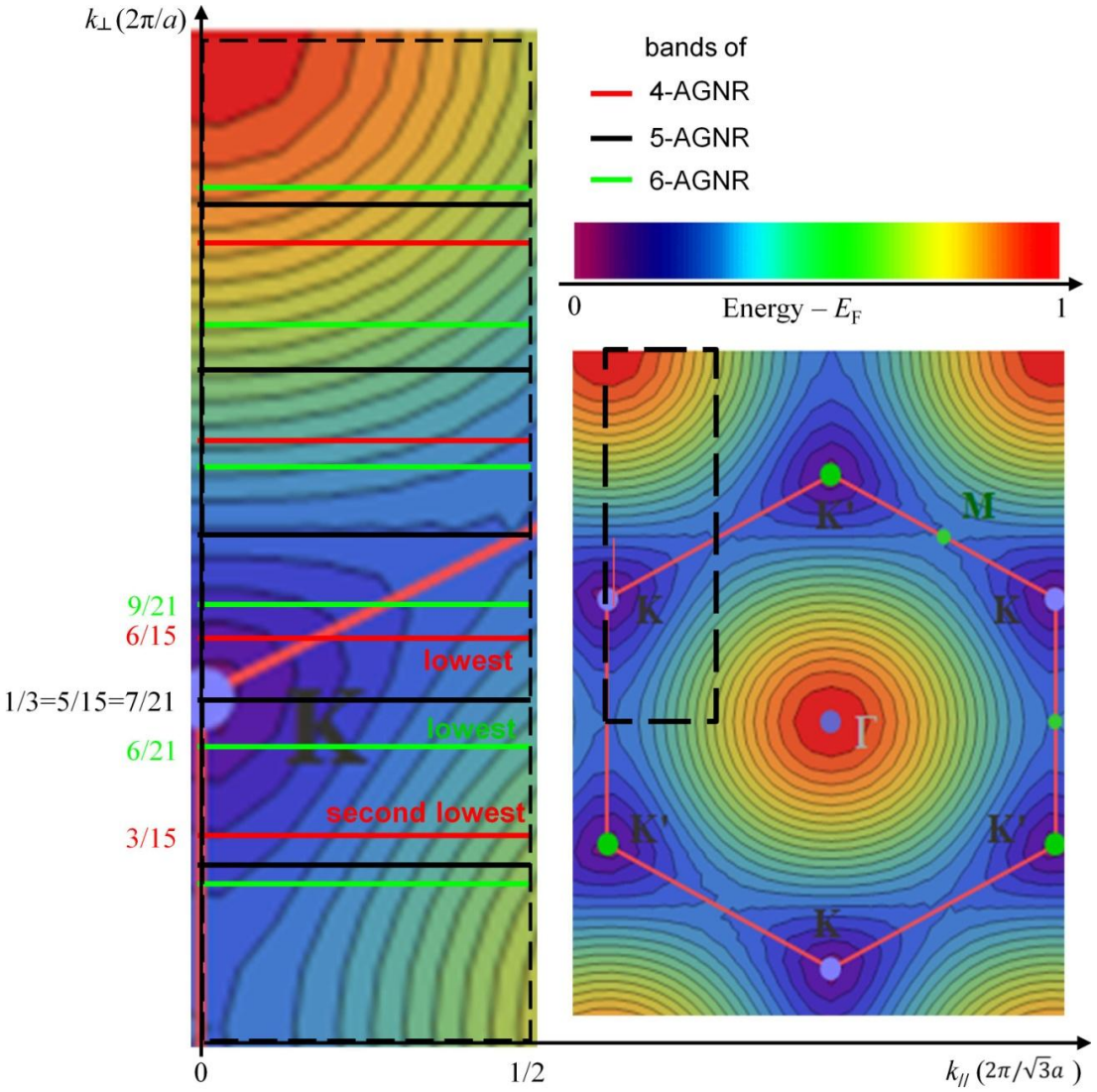

Fig. 3.3 2D energy contour plot of the graphene π*-band and its projection onto discrete $k_\perp$ values for 4-, 5-, and 6-AGNRs. The dashed black box on the right panel indicates the reduced Brillouin Zone, and is zoomed-in on the left panel.

The two effects 1) "*in 3p+1-AGNRs, the band immediately below **K** point is further to **K** point than the band immediately above **K** point*" and 2) "*the graphene energy contours are sparser below **K** point than above **K** point*" roughly offset each other. As a result, the lowest and second lowest unoccupied bands in each 3*p*+1-AGNR turn out to be at quite similar energies, especially at and near $k_{||} = 0$. This is also true for the

occupied bands, and explains the *double bands* feature observed in 3*p*+1-AGNRs (Fig. 3.1).

For 6-AGNR, the two quantized $k_\perp$ values nearest to **K** point are 6/21 and 9/21 (see Fig. 3.3), so the $k_\perp$ above **K** point is further to **K** point than the $k_\perp$ below **K** point, which is true for all 3*p*-AGNRs. In addition, the energy contours above **K** point are denser. The two effects add together and make the lowest and the second lowest unoccupied bands in a 3*p*-AGNR at quite different energies. So there is no *double bands* observed in 3*p*-AGNRs.

We also note from this quantization analysis that the lowest unoccupied band (highest occupied band) in a 3*p*-AGNR originates from graphene π*-band (π-band) immediately below the **K** point, at a $k_\perp$ value similar as that of the second lowest unoccupied band (second highest occupied band) in a 3*p*+1-AGNR. This explains why the LUGO+1 (HOGO-1) in 3*p*+1-AGNRs look similar as the LUGO (HOGO) in 3*p*-AGNRs (Fig. 3.2). By the same argument, we expect that the HOGO (LUGO) in 3*p*+1-AGNRs would also look similar as the HOGO-1 (LUGO+1) in 3*p*-AGNRs.

3.4 The "3*j*" Pattern under Edge Deformation

As we have reviewed in Section 1.1.2, the HOGO and LUGO of 3*p*+2-AGNRs exhibit an interesting "3*j*" pattern: absence of electron density on every third carbon row. This pattern has been recognized in the literature since 1987 [17, 25-27], and recently predicted analytically from tight-binding approach to be existing at E_F. The analytical TB approach ignores the deformation at the armchair edges [8]. In reality, as AGNRs energetically favor a deformation at the edge due to Peierls' distortion effect, which

opens a small gap in 3*p*+2-AGNRs [12], we wonder can the "3*j*" wavefunction pattern survive by considering the edge deformation effect?

The physical origin of the "3*j*" pattern is a standing wave with wavelength $\lambda = 3a/2$ formed by intervalley backscattering of Fermi electrons scattered off the armchair edges on both sides of a 3*p*+2-AGNR [8]. From this point of view, we expect that once the electron energy is away from E_F, the wavelength λ of this standing wave would also deviate from 3*a*/2.

In fact, such "3*j*" pattern is still observed experimentally in 14-AGNR, but with a very low resolution, as shown in Fig. 1.6 (b) left panel [23], where we believe edges are deformed. Our DFT calculated HOGOs and LUGOs of fully relaxed and hydrogen-passivated 5-AGNR, 8-AGNR, and 11-AGNR (Fig. 3.2) also indicate a preservation of this "3*j*" pattern. However, if we plot these wavefunctions with much smaller isosurfaces, as shown in Fig. 3.4 (d) and Fig. 3.5 (d), we could see some density of states on the 3rd and 9th rows of 11-AGNR. However, in the middle row of the AGNRs, i.e. the 3rd row of 5-AGNR and the 6th row of 11-AGNR, there is still almost no density of states.

To get a further insight into such DFT calculated patterns, we solved the nearest-neighboring TB Hamiltonian (see Section 1.1.3) with and without considering the edge deformation effect. Figure 3.4 (a-b) and Fig. 3.5 (a-b) show the HOGOs of 5-AGNR and 11-AGNR, respectively. Without considering the edge deformation effect, the HOGOs of 5-AGNR (Fig. 3.4 (a)) and 11-AGNR (Fig. 3.5 (a)) are both at E_F and both show a perfect "3*j*" pattern (coefficients on carbon atomic sites in the $(3j)^{th}$ rows are exactly zero), which is consistent with previous analytical prediction [8]. Moreover, the non-zero coefficients on other atoms are of the same magnitude.

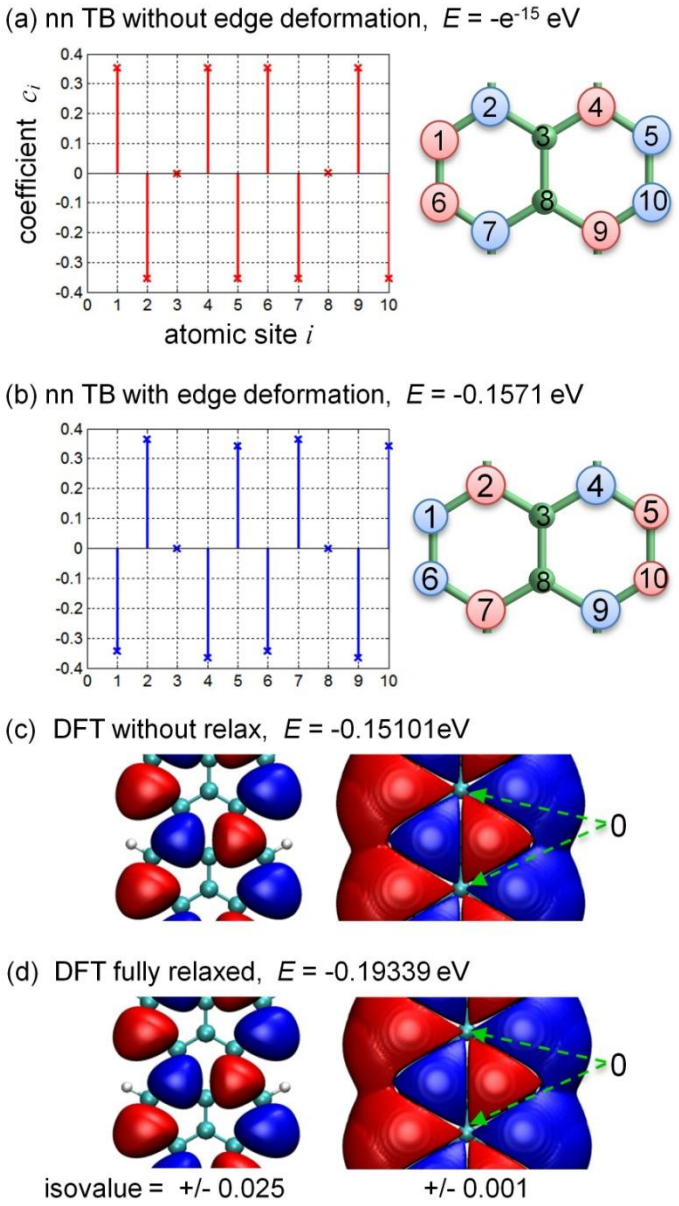

Fig. 3.4 (a-b) The HOGO of 5-AGNR by solving the tight-binding Hamiltonian with nearest neighbor (nn) approximation. In (a), we used a uniform hopping parameter $H_{ij} = -2.7\text{eV}$ for the whole structure, whereas in (b) we used $-2.7\text{eV} \times (1 + 12\%) = -3.024\text{eV}$ for $H_{1,6}$ and $H_{5,10}$, and -2.7eV for the rest H_{ij}. The radius of the red/blue spheres indicate the magnitude of the TB wavefunction coefficient at each atomic site with a +/- sign, and the figures on the left show the exact values of these coefficients. (c-d) The HOGO of hydrogen-passivated 5-AGNR (c) without and (d) with relaxation calculated using SIESTA with double-zeta basis-set. For clarity, we showed the wavefunction on only one of the two sublattices.

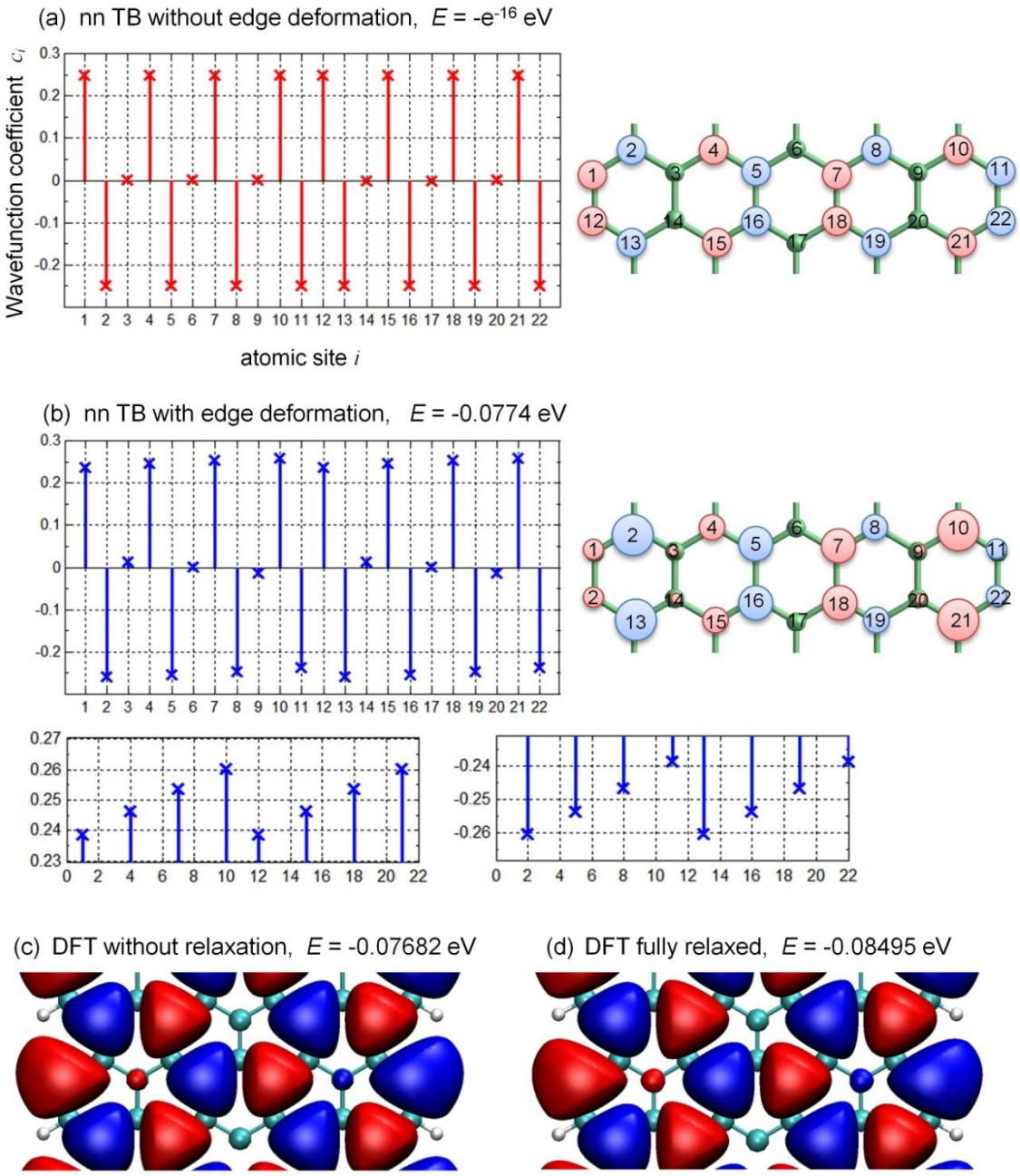

Fig. 3.5 (a-b) The HOGO of 11-AGNR by solving the tight-biding Hamiltonian with nearest neighbor (nn) approximations. In (a), we used a uniform hopping parameter -2.7eV for the whole structure, whereas in (b) we used -3.024eV for $H_{1,12}$ and $H_{11,22}$, and -2.7eV for the rest. The radius of the red/blue spheres indicate the magnitude of the TB wavefunction coefficient at each atomic site with a +/- sign (they are exaggerated to show the differences), and the figures on the left show the exact values of these coefficients. The two small figures at the bottom of (b) show the zooming-in at energy ranges of (±0.23, ±0.27) eV. (c-d) The HOGO of hydrogen-passivated 11-AGNR (c) without and (d) with relaxation, calculated using SIESTA with double-zeta

basis-set, with isosurface = +/- 0.01. For clarity, we showed the wavefunction on only one of the two sublattices.

As we take a 3.5% decrease [12] for bond lengths at the armchair edges into consideration (Fig. 3.4 (b) and Fig. 3.5 (b)), the HOGO changes in many aspects:

Firstly, the energy levels are shifted to 0.1571eV and 0.0774eV below E_F, for 5-AGNR and 11-AGNR respectively. These energy levels agree very well with the DFT calculated energy levels for hydrogen-passivated 5-AGNR and 11-AGNR without relaxation (Fig. 3.4 (c) and Fig. 3.5 (c)). After the hydrogen-passivated AGNRs are fully relaxed, their energy levels are shifted further down by a small amount, but the wavefunction patterns remain almost the same (Fig. 3.4 (d) and Fig. 3.5 (d)).

Secondly, the coefficients on carbon atoms in the 3rd and 9th rows of 11-AGNR deviate from zero, while the coefficients on the middle row (6th row of 11-AGNR and 3rd row of 5-AGNR) are still almost zero. These coefficients on the $(3j)^{th}$ rows are consistent with our DFT results (Fig. 3.4 (c-d) and Fig. 3.5 (c-d)).

Thirdly, the coefficients on atoms in the $(\text{non-}3j)^{th}$ rows are no longer of the same magnitude. Instead, both the positive coefficients and the negative coefficients are increasing in magnitude from one armchair edge towards the other edge. The absence of coefficients on the middle row is a result of cancellation of the symmetrically increasing coefficients from both armchair edges.

Next, let's use the TB results to understand the changes in energy and wavefunction pattern due to the deformation at the armchair edges. According to Eqn. (1.4), we can obtain the eigenenergy as

$$E = \left(\sum_{j=nn} H_{ij} c_j\right)/c_i \qquad (3.1)$$

for $c_i \neq 0$.

For the case without edge deformation, the HOGOs of 5-AGNR and 11-AGNR both exhibit a perfect "3*j*" pattern. In such a pattern, each carbon atom has only two effective nearest neighbours with non-zero coefficients, that are of the same magnitude but opposite sign. In addition, H_{ij} is uniform over the whole structure since all the bond lengths are considered to be the same. Therefore,

$$\sum_{j=nn} H_{ij} c_j = 0 \qquad (3.2)$$

for all carbon atoms *i*. This means that a perfect "3*j*" pattern gives an eigenenergy of exactly zero.

As the bond lengths at the armchair edges become shorter, a perfect "3*j*" pattern can no longer be a solution to the TB Hamiltonian. Would it be, the eigenenergy obtained via Eqn. (3.1) from an atom *i* in the inner region is E = 0, but the eigenenergy obtained from an atom *j* at the armchair edge would be $E \neq 0$ as the hopping parameter with one of *j's* two neighbours increases. Let's demonstrate this using the edge atom 1 in 11-AGNR shown in Fig. 3.5 (b) as an example, $H_{1,12}$ increases as the bond between atom 1 and atom 12 shortens, so the sum $H_{1,12}c_{12} + H_{1,2}c_2$ deviates from zero.

To balance the increase in $H_{1,12}$, the magnitude of coefficient at the edge atom c_{12} has to decrease, while the magnitude of coefficient at atoms on the second row c_2 has to increase. Therefore, the wavefunction pattern adjusts itself to fit into an eigen-solution of the modified Hamiltonian with eigenenergy lower than the Fermi level, which stabilizes the structure. What we obtained in Fig. 3.4 (b) and Fig. 3.5 (b) are these eigen-solutions.

3.5 Chapter Summary

In this chapter, we showed the double bands feature in 3*p*+1-AGNRs and provided an explanation from the quantization approach. This also explains the similarity between HOGO-1s (LUGO+1s) of 3*p*+1-AGNRs and HOGOs (LUGOs) of 3*p*-AGNRs. We also discussed the effects of deformations at the armchair edges of a 3*p*+2-AGNR, including 1) a small gap opens between HOGO and LUGO and 2) slight deviation of the wavefunction pattern from the perfect "3*j*" pattern. In particular, the electron density on the $(3j)^{th}$ carbon rows (except the middle row) becomes non-zero, but they are still very small compared to electron density on the $(\text{non-}3j)^{th}$ rows.

Chapter 4. Length-Independent Transmission Peaks

We are greatly motivated by the interesting transmission curves of AGNR junctions calculated from tight-binding approaches by Dr. Son (Section 1.3), so we performed a very thorough and systematical investigation on why the transmission peaks are independent of the length of the middle ribbon. In this chapter, we present an explanation for this anomalous phenomena. Most of the contents in this chapter are published in Ref. [86], and we are using them with permission from Elsevier.

4.1 DFT and Tight-Binding Results

First of all, we used density functional theory (DFT) to calculate the transmission of a 23-5-23-AGNR Z-Z junction with varying *l*. Figure 4.1 (a) shows the structure we studied, where each dangling bond at the edges is passivated with one hydrogen atom. The DFT transmission curves with varying *l* (Fig. 4.1 (b)) are consistent with the preliminary tight-binding results (Fig. 1.12 (b)).

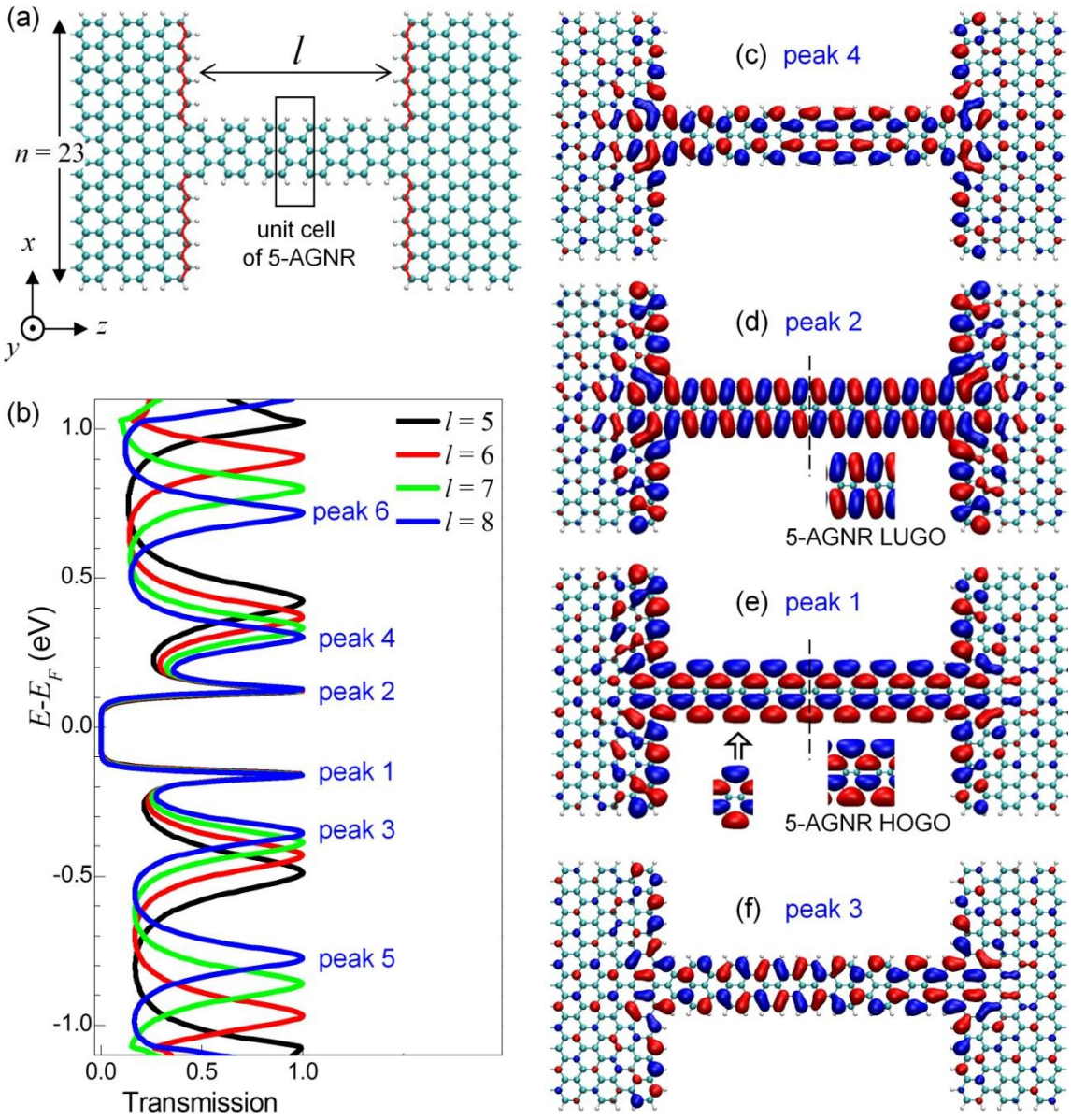

Fig. 4.1 (a) Atomic structure of 23-5-23-AGNR junction with two zigzag edge interfaces (denoted by red lines). The length of the 5-AGNR segment l = 5 unit cells. (b) Transmission curves of the junction shown in (a) with varying l, calculated from first-principles scattering-state approach as implemented in SCARLET [76]. (c-f) Real parts of eigenchannel wavefunction isosurfaces with isovalue = +/- 0.025, calculated using SCARLET at peaks 1-4 (see (b)) of the junction with l = 8. The imaginary parts (not shown) show similar features. The insets in (e) and (d) show the HOGO and LUGO of perfect 5-AGNR[1] with isovalue = +/- 0.03, calculated using SIESTA [75]. The arrow in (e) indicates insertion of an extra unit and is discussed in Section 4.2.1. This figure is reprinted from Ref. [86], with permission from Elsevier.

[1] same as those shown in Fig. 3.2.

4.1.1 Quantum Confinement Effect

Since the 5-AGNR between the two semi-infinite 23-AGNRs is essentially a segment with finite length *l*, it is instructive to visualize it as a "molecule" that is strongly coupled to the leads. As a result, the continuous band structure of a perfect 5-AGNR reduces to a finite number of discrete states in the 5-AGNR "molecule". These discrete states couple to the electrodes to result in resonant transmission peaks. The transmission probability reaches the maximum value of T = 1 at the resonant energy of the state and decays at energies away from the resonant energy, forming a Lorentzian-shaped transmission peak. As *l* increases, the eigenenergies of these discrete states are expected to shift closer towards E_F[2] because of a weaker quantum confinement effect. Therefore, we expect the corresponding resonant transmission peaks also approach E_F as *l* increases. Furthermore, the lifetime of these states (the coupling strength to the leads) should decrease as the molecular wire gets longer, leading to a narrowing of the associated transmission peaks.

4.1.2 Anomalous Length Behavior

The four transmission peaks 3, 4, 5, and 6 in Fig. 4.1 (b) follow exactly the expected *l*-dependence – approaching to E_F and becoming narrower, as *l* increases. In contrast, both the energies and widths of the frontier transmission peaks 1 and 2 closest to E_F show negligible dependence on *l*.

We wonder would the energies of the two anomalous peaks 1 and 2 vary if *l* is sufficiently long? As further increasing *l* is challenging for DFT, we use nearest neighbor tight-binding model (Section 2.1) to extend our study on the eigenenergies of

[2] The Fermi level of a 2-lead system is the charge neutrality level in the leads.

corresponding states in a periodic structure (bulk with the structure shown in Fig. 4.1 (a) as the unit cell) with l varying from 1 up to 50 unit cells. As shown in Fig. 4.2, the tight-binding eigenenergies agree well with the DFT results. As l increases, the eigenenergies of the states away from E_F (green square symbols) shift closer to E_F and asymptotically approach some constant values, consistent with the quantum confinement effect. In contrast, the eigenenergies of the frontier states, remarkably, are almost invariant. The DFT and TB results indicate that with appropriate doping or gating, one can achieve large length-independent near-resonant transmission. What is the origin of these anomalous peaks?

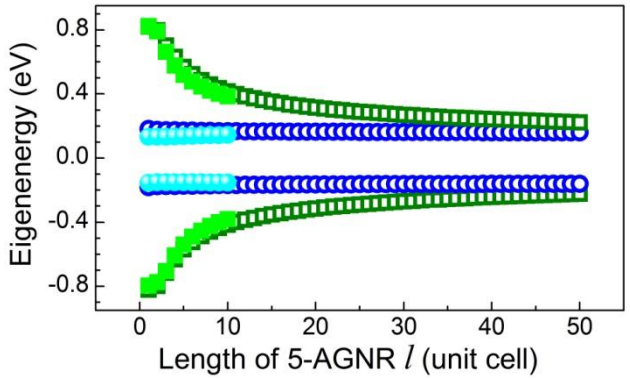

Fig. 4.2 Eigenenergies of the two l-independent states (blue circle) and two typical l-dependent states (green square) of 23-5-23-AGNR periodic structure (bulk with the structure in Fig. 4.1 (a) as the unit cell[3]) as a function of l obtained by (i) tight-binding model (hollow symbols) and (ii) DFT (solid symbols), reprinted from Ref. [86] with permission from Elsevier.

4.2 Origin of the Anomalous Transmission Peaks

The eigenchannel wavefunctions of the almost l-independent peaks (Fig. 4.1 (d-e)) resemble the HOGO and LUGO of perfect 5-AGNR (see Section 3.2) coupled seamlessly to the zigzag edge state [11]. In particular, the periodic pattern of

[3]The length of 23-AGNR = 8 unit cells.

wavefunction in a perfect 5-AGNR is well preserved when the 5-AGNR becomes a segment in-between two 23-AGNR leads. In contrast, such periodic pattern is not present in eigenwavefunctions of the usual *l*-dependent peaks 3 to 6 (see e.g. Fig. 4.1 (c) and (f)). The preservation of the periodic wavefunction pattern indicates that electrons in these states behave similarly as if they were in an infinite 5-AGNR. Specifically, it seems electrons are not confined within the finite 5-AGNR segment. This is attributed to the Fermi level zigzag edge state essentially serving as an electron source or drain for states near E_F. For states further away from E_F (e.g. peaks 3 to 6), there is no such source or drain of electrons, thus confinement effect comes into effect. In addition, if we remove the zigzag edges, such anomalous peaks also disappear (see Section 5.1), confirming the necessity of the edge state as an electron source or drain for these near-E_F states.

4.2.1 The Length Independence of Peak Energy

To quantitatively explain the length-independence of the resonant energy, we provide a proof by mathematical induction in Appendix A, and elucidate the key ideas here. The essential physics is: (1) the wavefunction exhibits a locally repeating pattern in the 5-AGNR region, and (2) local interactions are sufficient to account for the physics of these states.

We claim that for a 23-5-23-AGNR Z-Z structure with length of $l = m$ unit cells, there exists an eigenstate containing m locally repeating units within the 5-AGNR region and this eigenstate has eigenenergy E independent of l. Figure 4.3 (a) clearly shows that for $l = 3$, the occupied frontier state is locally repeating in the 5-AGNR region (Fig. 4.1 (d-e) qualitatively show the same feature for $l = 8$). Next, suppose for $l = m$, we have a

frontier state $\psi_m = (c_1, c_2, \dots, c_i, \dots)$ that is locally repeating in the 5-AGNR region, with eigenenergy *E*. The Schrödinger equation of this system in matrix form is

$$\sum_j H_{ij}^{(m)} c_j^{(m)} = E c_i^{(m)} \qquad (4.1)$$

where atom index *i* runs over all atoms in the structure. Including local interactions within the nearest-neighboring unit cells is more than enough to describe the physics of graphene [12, 29]. Therefore, $H_{ij} = 0$ for all neighbors *j* beyond the nearest unit cells of *i*. Then for $l = m+1$, we can construct a state ψ_{m+1} that is identical to ψ_m, but with an extra repeating unit in the 5-AGNR region (see Fig. 4.1 (e) showing the insertion of one extra repeating unit in the 5-AGNR region) and being renormalized. Since only local interactions are important, ψ_{m+1} is a solution to the Hamiltonian $H^{(m+1)}$ with the same eigenenergy *E*

$$\sum_j H_{ij}^{(m+1)} c_j^{(m+1)} = E c_i^{(m+1)} \qquad (4.2)$$

This can be seen by considering two groups of carbon atoms in the structure with $l = m+1$. The first group consists of atoms inherited from the structure with length $l = m$, and the second group consists of atoms within the extra unit. For an atom *i* in the first group, both c_i and c_j do not change except a scaling down by the renormalization factor λ. The tight-binding hopping interactions H_{ij} between atom *i* and its neighbors *j* also remain the same. Therefore, all these atoms satisfy the Schrödinger Eqn.(4.2). For atoms in the second group, since the set of this extra unit plus its local neighbors is just a copy of another set in the first group, all atoms in this group also satisfy the Schrödinger Eqn.(4.2). A more detailed analysis can be found in Appendix A.

We see from the induction proof that the length-independence of eigenenergies is determined by the existence of locally repeating units in the wavefunction. This crucial

point is further illustrated in Fig. 4.3, where the frontier almost *l*-independent state has locally repeating units in the 5-AGNR region for *l* varying from 3 up to 50 unit cells, while the *l*-dependent state does not. A periodic wavefunction pattern is straightforward in an infinite periodic structure (see e.g. wavefunctions of perfect AGNRs in Fig. 3.2), but can hardly be preserved if the structure becomes a short segment. A locally repeating pattern can be unusually preserved in the 23-5-23-AGNR junction because, the zigzag edges serve as sources and drains so that electrons essentially do not experience a confinement effect. In contrast, for a typical junction, such as oligophenyl-diamine wires attached to gold electrodes [69], the symmetry in the transport dimension is broken by the termination at the two ends, hence the structure cannot support states with locally repeating units.

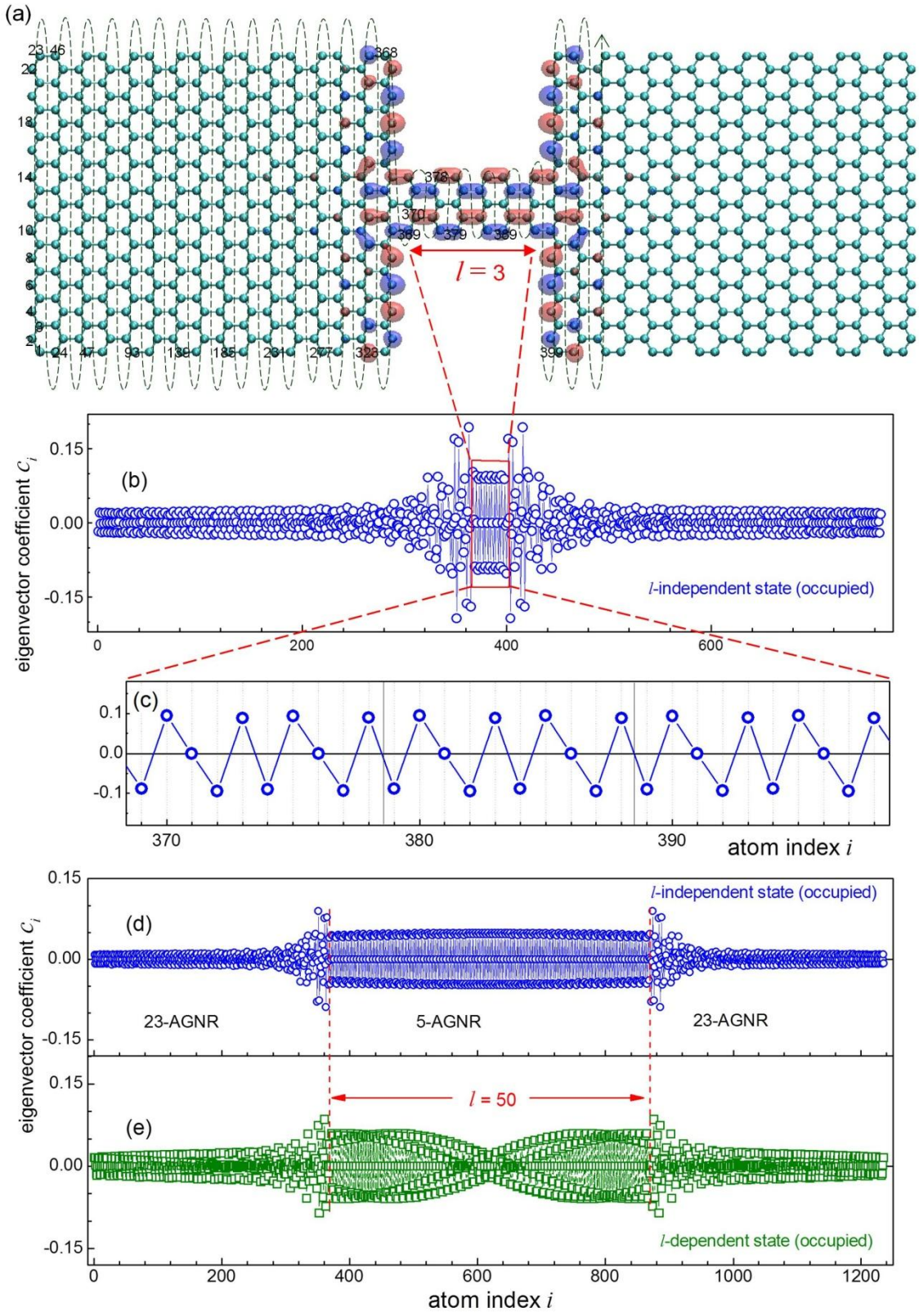

Fig. 4.3 Eigenwavefuntion coefficient c_i as a function of atom index i for the 23-5-23-AGNR Z-Z periodic structure, obtained by solving the nearest neighbour TB Hamiltonian. (a) The atomic structure with l = 3 to illustrate the atom index i. We

count the carbon atoms along the zigzag-shaped chains from bottom to top, and chain after chain from left to right, as indicated by the green dash line in (a). The red and blue isosurfaces represent the wavefunction of the occupied *l*-independent state calculated using SIESTA. (b) Coefficients for the occupied *l*-independent state with l = 3. (c) Zoom-in of (b) over the 5-AGNR region with a length of three units. (d-e) Coefficients for the (d) occupied *l*-independent and an (e) occupied *l*-dependent state with l = 50. (b-d) are reprinted from Ref. [86] with permission from Elsevier.

4.2.2 The Length Independence of Peak Width

Next, to understand why the width of transmission peaks remains the same as l increases, we examine how the wavefunction distribution along the length varies with increasing l. Figure 4.4 shows that as l increases from 2 to 9 unit cells, the weight of the wavefunction at the zigzag edges decreases significantly, while that in the 23-AGNR and 5-AGNR regions show only a minimal decrease[4]. This implies that, as the 5-AGNR lengthens, the zigzag edges serve as a "source" of electrons to enable these frontier wavefunctions to spread out into the longer ribbon without affecting weight of wavefunction in the 23-AGNR region. Therefore, as l increases, the coupling of the state to the 23-AGNR leads remains almost the same, which determines that the width of transmission peaks remains approximately constant.

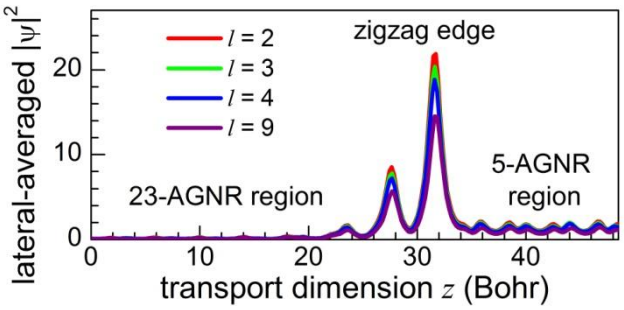

Fig. 4.4 Spatial profile of lateral-averaged absolute square of the occupied *l*-independent state for the 23-5-23-AGNR Z-Z periodic structure, obtained from DFT, as a function of the transport dimension z. The wavefunctions for structures with different

[4] This is approximately consistent with the induction argument above where the wavefunction changes by an overall normalization factor, because the wavefunction has a much larger weight on the zigzag edges.

l are aligned at one of the zigzag edge interfaces. The unoccupied *l*-independent state shows similar features. This figure is reprinted from Ref. [86] with permission from Elsevier.

4.3 Chapter Conclusion

We find that these almost *l*-independent frontier transmission peaks still persistent when the 5-AGNR is transversely shifted across the width (along the *x* direction in Fig. 4.1 (a)). Our tight-binding model and DFT results show that these unusual transport properties for the 23-5-23-AGNR junction can also be generalized to other AGNR-junction with the middle AGNR in the 3*p*+2 family, but not observed in AGNR-junctions with the middle AGNR in 3*p* and 3*p*+1 families. For example, we have verified using DFT that 23-11-23- and 35-17-35-AGNR Z-Z junctions also exhibit nearly length-independent transmission peaks close to E_F. This family behavior is consistent with the fact that states near E_F is only available in 3*p*+2-AGNRs (see Section 1.1) [12]. Further studies on the family behavior are presented in Chapter 6.

Chapter 5. Bonding and Antibonding Coupling

We have demonstrated in Chapter 4 that the two zigzag edge interfaces play a significant role in liberating electrons from being confined within the 5-AGNR segment, which leads to the eigenenergies being independent of the length of 5-AGNR segment. Since there are two zigzag edge interfaces in the AGNR Z-Z junction, and the wavefunctions of the anomalous states show localization on both zigzag edge interfaces (see Fig. 4.1 (d-e)), we wonder: are both zigzag edge interfaces necessary for the anomalous states?

5.1 Necessity of the Zigzag Edges

To separate the role of each zigzag edge interface, we designed a reference structure with one zigzag edge interface plus one armchair edge interface, which we refer as a Z-A junction, as shown in Fig. 5.1 (b). We plot the transmission curves of both Z-Z and Z-A junctions with the same length l = 3 in Fig. 5.1 (c). The Z-Z junction shows two resonant transmission peaks close to E_F, at -0.16eV and 0.12eV, which are identified as the anomalous l-independent peaks from their energies and eigenchannel wavefunctions, whereas the Z-A junction does not have such transmission peaks. This comparison clearly demonstrates that zigzag edges on both interfaces of the junction are required for the anomalous peaks.

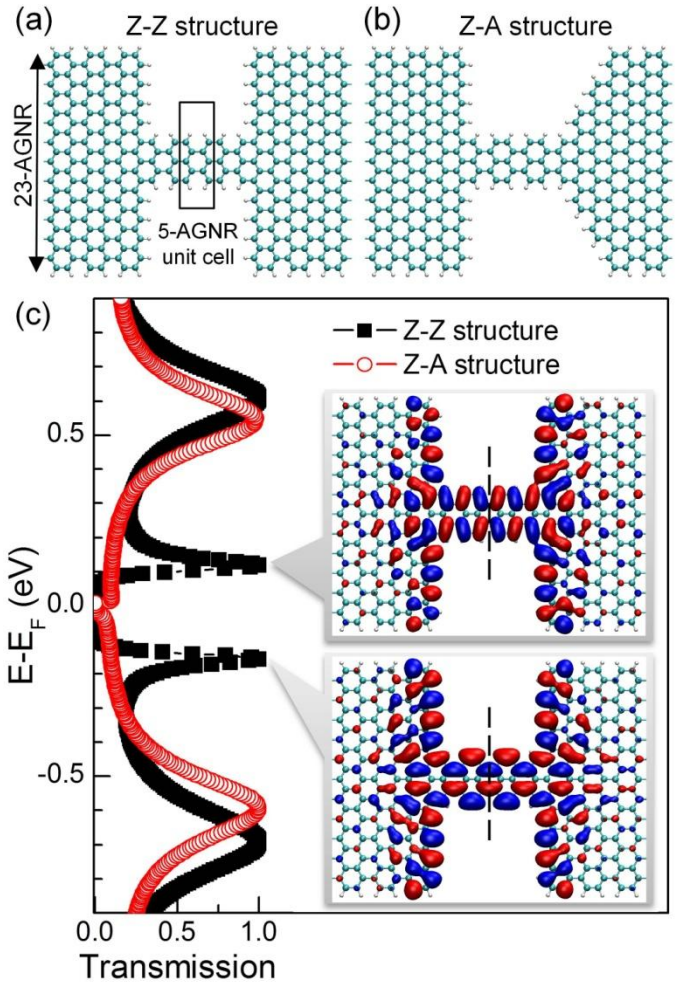

Fig. 5.1 (a-b) Atomic structures of AGNR-junctions with two zigzag edge interfaces (Z-Z structure) and one zigzag edge interface plus one armchair edge interface (Z-A structure). The length of the middle 5-AGNR segment is 3 unit cells for both structures. (c) Transmission curves of junctions shown in (a-b). Inset of (c): real parts of the eigenchannel wavefunction isosurfaces with isovalue = +/- 0.025 at the two transmission peaks (the imaginary parts show the same features).

5.2 The Bonding and Antibonding Coupling

We also note that the eigenchannel wavefunction of the occupied anomalous peak (at -0.16eV) is symmetric with respect to a plane normal to and through the center of the two-dimensional structure, as indicated by the black dashed line in Fig. 5.1 (c) inset. On the other hand, the unoccupied eigenchannel wavefunction (at 0.12eV) is antisymmetric with respect to the same plane. The symmetric and antisymmetric wavefunction patterns plus the necessity of both zigzag edge interfaces strongly suggest

that the two anomalous states arise from bonding and antibonding combinations of two "original" states. In addition, we expect the original states should be close to or at E_F and related to the zigzag edges (see Section 1.2 for a review on bonding and antibonding theory).

Representing the original states using φ_1 and φ_2, then the bonding and antibonding combinations would be

$$\psi_b = (\varphi_1 + \varphi_2)/\sqrt{2} \qquad (5.1)$$

$$\psi_{ab} = (\varphi_1 - \varphi_2)/\sqrt{2} \qquad (5.2)$$

ψ_b and ψ_{ab} are present as the HOMO-1 and LUMO+1 of the 23-5-23-AGNR periodic structure, as shown in Fig. 5.2 (a-b).

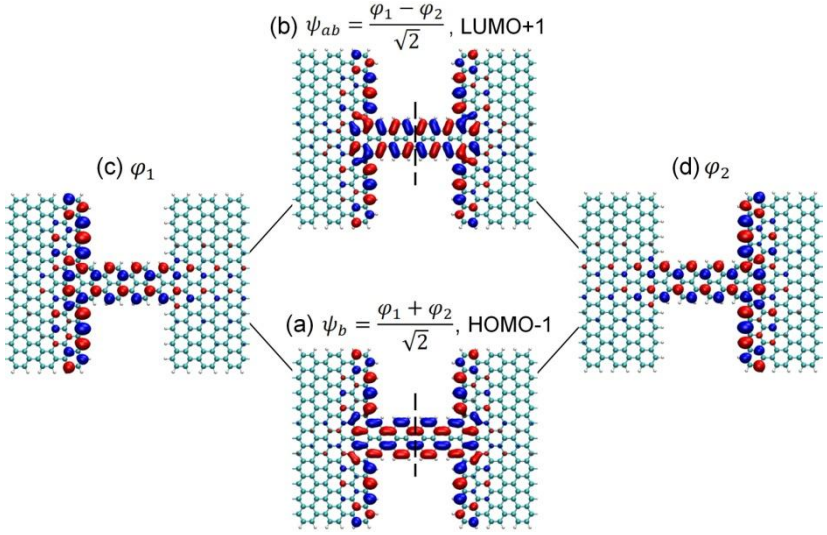

Fig. 5.2 (a-b) The HOMO-1 and LUMO+1 eigenwavefunctions of the 23-5-23-AGNR Z-Z periodic structure, at energies of E_F - 0.150eV and E_F + 0.135eV, respectively. We refer to these states as the bonding state ψ_b and the antibonding state ψ_{ab}. The dashed line represent a plan normal to the cut through the centre of the structure. (c-d) Original "zigzag + AGNR" states deduced from the bonding and antibonding states by $\varphi_1 = (\psi_b + \psi_{ab})/\sqrt{2}$ and $\varphi_2 = (\psi_b - \psi_{ab})/\sqrt{2}$. For all wavefunction isosurfaces, isovalue = +/- 0.025.

According to eqns. (5.1) and (5.2), we can deduce the "original" states from ψ_b and ψ_{ab} as $\varphi_1 = (\psi_b + \psi_{ab})/\sqrt{2}$ and $\varphi_2 = (\psi_b - \psi_{ab})/\sqrt{2}$. These deduced "original" states are plotted in Fig. 5.2 (c-d). Visually, φ_1 and φ_2 look like the usual zigzag edge state extending seamlessly into the 5-AGNR segment without any spatial decay. Such non-decaying extension seems a very unusual behavior since the zigzag edge state is well-known to be localized along the zigzag edge [11], as we reviewed in Section 1.1.3. Based on this distribution property, we refer to φ_1 and φ_2 a "zigzag + AGNR" state.

5.3 "Zigzag + AGNR" State in Real Structures

So far, we have only observed the "zigzag + AGNR" states in their bonding and antibonding coupled form, i.e. ψ_b and ψ_{ab} in the Z-Z structure. By replacing one of the two sp^2-terminated zigzag edge interfaces with an armchair edge interface (Fig. 5.3 (a)) or a sp^3-terminated zigzag edge interface (Fig. 5.3 (b)), one of the "zigzag + AGNR" states would be destroyed, thus allowing us to observe the remaining "zigzag + AGNR" state at E_F in our DFT calculations, as shown in Fig. 5.3. The "zigzag + AGNR" state in both structures does not decay over the 5-AGNR region. These observations further confirms our prediction of the "zigzag + AGNR" state.

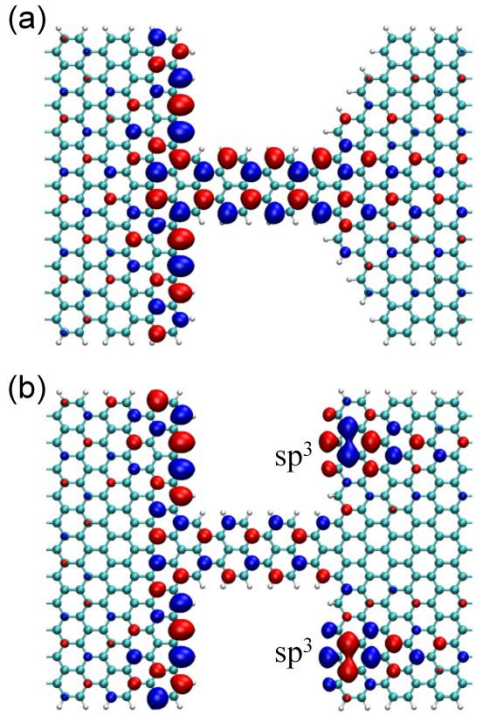

Fig. 5.3 The "zigzag + AGNR" state observed as a Fermi level eigenwavefunction, obtained using DFT under periodic boundary condition in 23-5-23-AGNR junctions with one sp^2-terminated zigag edge interface plus one (a) armchair edge interface or (b) sp^3-terminated zigzag edge interface[5].

5.4 Consistence with the Length-Independence Theory

As reviewed in Section 1.2, the energy splitting between ψ_b and ψ_{ab} is determined mainly by the overlapping between the two original states φ_1 and φ_2. As l increases, the overlapping region of φ_1 and φ_2 seems to increase, which would result in a larger energy splitting. However, the eigenenergies of ψ_b and ψ_{ab} are demonstrated to be almost independent of l in Chapter 4. How are these two facts consistent with each other?

[5] We note from our DFT calculations that the triangular shaped wavefunction localizations at the two sp^3-terminated zigzag edges in (b) is typical for this type of edge, and it does not extend into the narrow AGNR.

To understand this better, we can partition the eigenenergy of a state into energy contributed by coupling between different pairs of atoms from a tight-binding approach. For simplicity, we now use the nearest neighbor approximation which well reproduces the DFT results [12, 29]. Specifically, we can express the eigenenergy *E* as

$$E = < \boldsymbol{\psi}^{(m)} \big| \boldsymbol{H}^{(m)} \big| \boldsymbol{\psi}^{(m)} > \qquad (5.3)$$

Then

$$E = \sum_{i=1}^{N} E_i \qquad (5.4)$$

where E_i is the energy contributed by each atom i by interacting with all of its nearest neighbours j

$$E_i = c_i^{(m)} \sum_{j \in nn} H_{ij}^{(m)} \, c_j^{(m)} \qquad (5.5)$$

Taking ψ_b and ψ_{ab} of 23-5-AGNR Z-Z periodic structure as an example, we plot the eigenenergy contributed by different groups of atoms in Fig. 5.4. The eigenenergy *E* obtained by summing up E_i of all atoms as a function of *l* (blue curves in Fig. 5.4) are exactly the same as the bonding and antibonding state eigenenergy we solved (shown in Fig. 4.2). As *l* increases, the magnitude of eigenenergy contributed from the 5-AGNR region (green curves in Fig. 5.4) increases. Therefore, this is consistent with the intuitive interpretation that increased overlapping between φ_1 and φ_2 would result in larger energy splitting. However, the magnitude of eigenenergies contributed from the 23-AGNR region (red curves in Fig. 5.4) decreases with increasing *l* due to the significant scaling down of all coefficients c_i, and this compensates most of the increase in magnitude of eigenenergies contributed from the 5-AGNR region. Specifically, as the 5-AGNR becomes longer, a portion of the state transfers from the 23-AGNR region to the 5-AGNR region.

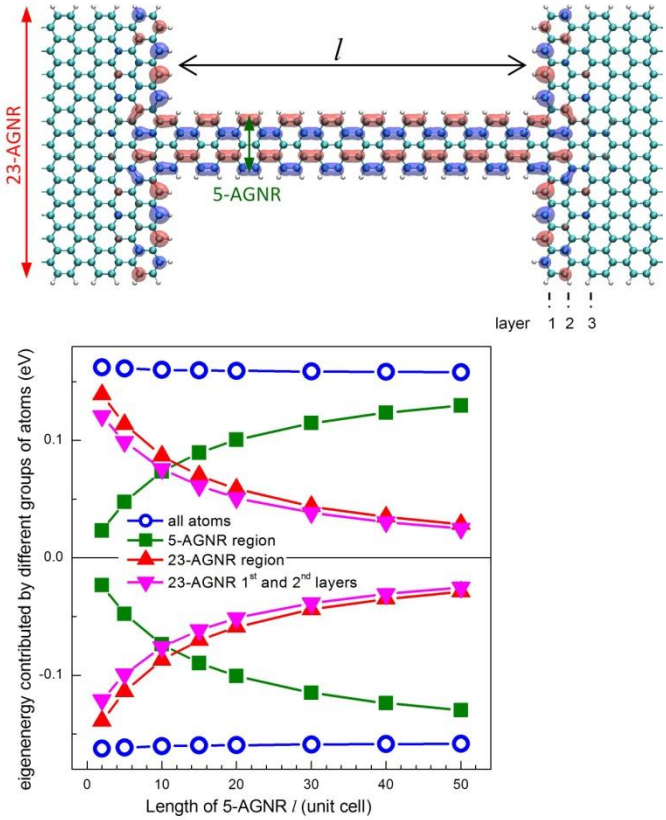

Fig. 5.4 Top panel: atomic structure of the 23-5-23-AGNR Z-Z structure with l = 9 unit cells. The isosurface (isovalue = +/- 0.025) shows the bonding state calculated using SIESTA. Bottom panel: eigenenergies of the (below E_F) bonding and (above E_F) antibonding states of 23-5-23-AGNR Z-Z periodic structure contributed by different groups of atoms. Each layer consists of one zigzag-shaped carbon chain across the width of AGNR, as labelled in the atomic structure.

Figure 5.4 also indicates that the energy contributed from the 23-AGNR is mainly coming from the first two layers capped by the zigzag edge interface. This observation is consistent with the fact that the state decays very fast from the zigzag edge towards the inner region of 23-AGNR.

5.5 Chapter Summary

We have demonstrated in this chapter that zigzag edges on both interfaces of the AGNR junction are necessary for the anomalous states, as they are bonding and

antibonding couplings of two original zigzag edge derived states. We have observed the original “zigzag + AGNR” state in real structures. We have also showed that the bonding and antibonding coupling interpretation is consistent with the length-independence property we presented in Chapter 4.

Chapter 6. Extension of the Zigzag Edge State into an AGNR: Family Dependence

As we have reviewed in Section 1.1.3, the zigzag edge state decays into the inner graphene region capped by the zigzag edge (we define this region as the "backland" of the zigzag edge). Such decaying behavior could be understood from the tight-binding based *nearest-neighboring sum rule* [11]. Then, can the zigzag edge state extend into a region outside its backland, that is beyond the applicability of the *nearest-neighboring sum rule*?

In the wide-narrow-wide-AGNR junctions we are studying, while the wide-AGNR is within the backland of the interface zigzag edge, the narrow-AGNR is well outside the backland of the zigzag edge but still immediately connected to the zigzag edge (see Fig. 6.1 for example). In fact, the bonding and antibonding states we discussed in Chapter 5 are states originating from the zigzag edges. By looking at the contributions from each sublattice, i.e. φ_1 or φ_2, as visualized in Fig. 5.2 (c-d), it is obvious that φ_1 and φ_2 both look like the usual zigzag edge state extends seamlessly into 5-AGNR within the same sublattice. Unlike the decay behavior of the zigzag edge state towards its backland, the extension into 5-AGNR seems not decaying. As a result of this non-decaying extension, the eigenenergies of the associated bonding and antibonding states are independent of the length of the 5-AGNR segment (Chapter 4).

In this chapter, we show that the zigzag edge state can extend into a general narrow-AGNR. However, the decaying behavior of such extension is strongly dependent on the family of the narrow-AGNR.

6.1 Non-Decaying Extension into 3*p*+2-AGNRs

Figures 6.1 to 6.3 and Figs. B1 to B2 (Appendix B) show the DFT calculated bonding and antibonding states in three different AGNR-junctions, all with the middle AGNR in the 3*p*+2 family. For all of these states, we do not see any obvious decay inside the middle AGNR, even when we separating them into contributions from two sublattices.

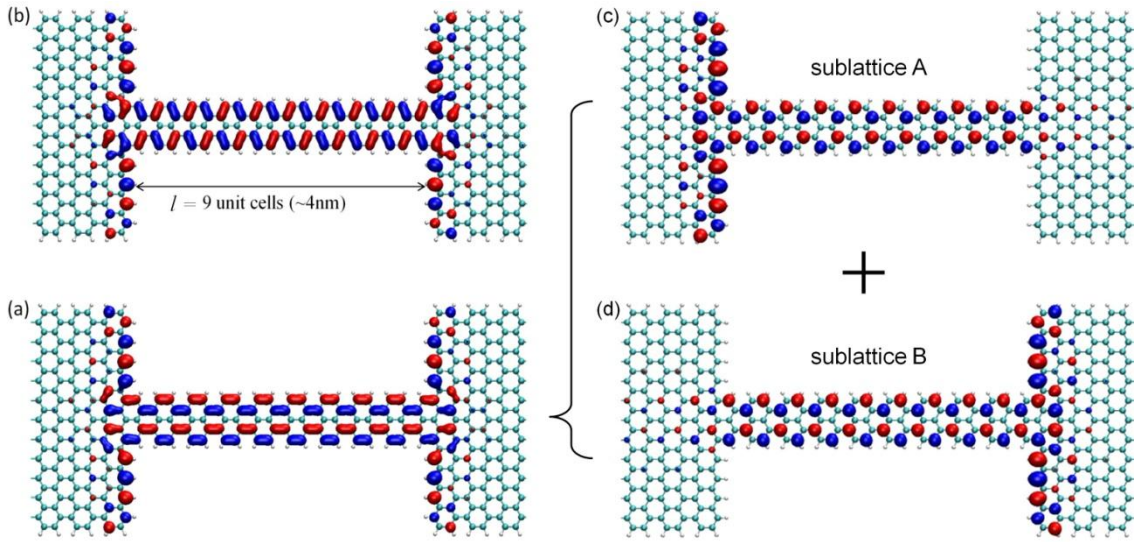

Fig. 6.1 The (a) bonding and (b) antibonding states in 23-5-23-AGNR junction with l = 9 unit cells, calculated using SIESTA under periodic boundary condition. (c-d) Contributions to the bonding/antibonding state from two sublattices. Isovalue = ±0.025 for all wavefunction isosurfaces.

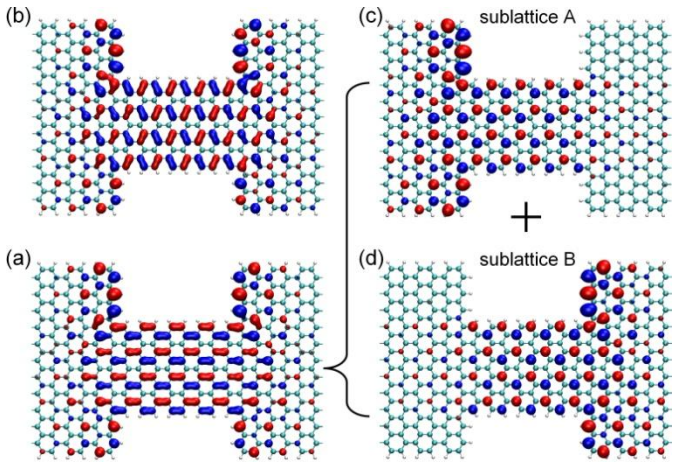

Fig. 6.2 The (a) bonding and (b) antibonding states in 23-11-23-AGNR junction, calculated using SIESTA under periodic boundary condition. (c-d) Contributions to the bonding or antibonding state from two sublattices. Isovalue = ±0.025 for all wavefunction isosurfaces.

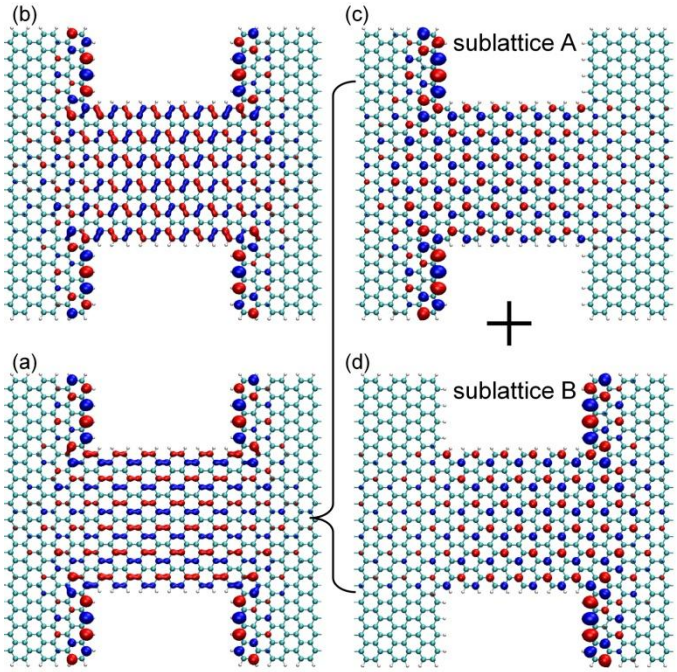

Fig. 6.3 The (a) bonding and (b) antibonding states in 35-17-35-AGNR junction, calculated using SIESTA under periodic boundary condition. (c-d) Contributions to the bonding or antibonding state from two sublattices. Isovalue = ±0.025 for all wavefunction isosurfaces.

We wonder if we could see any decay if l is sufficiently long. We checked this using DFT calculations for a 23-5-23-AGNR junction with l = 9 unit cells (~ 4nm, see Fig. 6.1), where we do not see any obvious decay. Further increase of l is challenging for DFT, so we switched to nearest-neighboring tight-binding model to solve the Hamiltonian of a 23-5-23-AGNR junction under periodic boundary conditions. We reproduced the bonding and antibonding states using tight-binding calculations, which do not decay over the 5-AGNR for l varying from 3 up to 50 unit cells (see Fig. 6.4). In addition, according to the induction principle in the proof presented in Chapter 4 and Appendix A, as long as we have a state for a short junction that contains at least 3 locally repeating units (do not decay), we expect a similar non-decaying state (locally repeating) for a junction of any length.

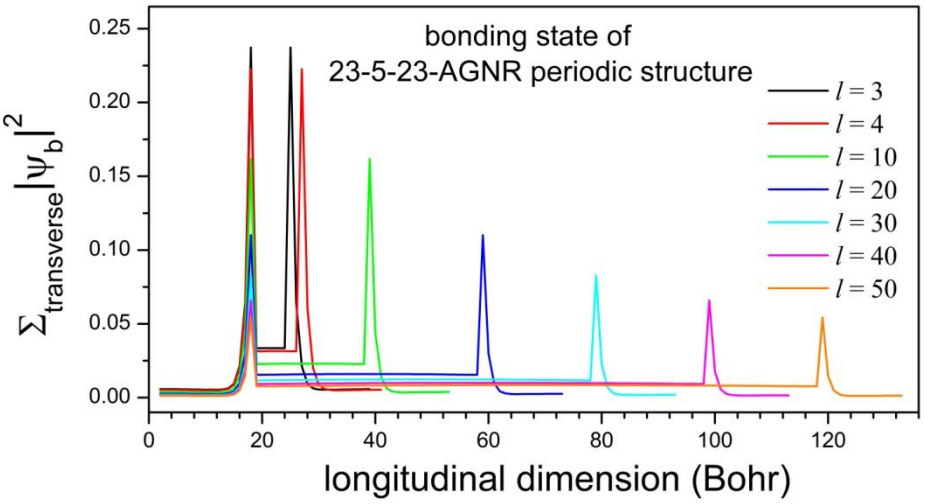

Fig. 6.4 Spatial profile of laterally-summed absolute square of the bonding state of 23-5-23-AGNR junction with varying l, as a function of the longitudinal dimension z. The states are obtained by solving the nearest-neighboring tight-binding Hamiltonian of the junction under periodic boundary condition. Each profile shows two peaks symmetric with respect to the middle point of the length, and the first peaks of all seven profiles locate at the same longitudinal position (~ 18 Bohr).

As we have already implied in Chapter 4, the wavefunction patterns of the bonding and antibonding states resemble the usual zigzag edge state coupled to the HOGO and LUGO of the middle 3*p*+2-AGNR (see Fig. 3.2). They can couple so well because gaps in 3p+2-AGNRs are extremely small, so that the DOS of HOGO/LUGO of 3*p*+2-AGNRs and the DOS of the zigzag edge state overlap in energy, as shown in Fig. 6.5.

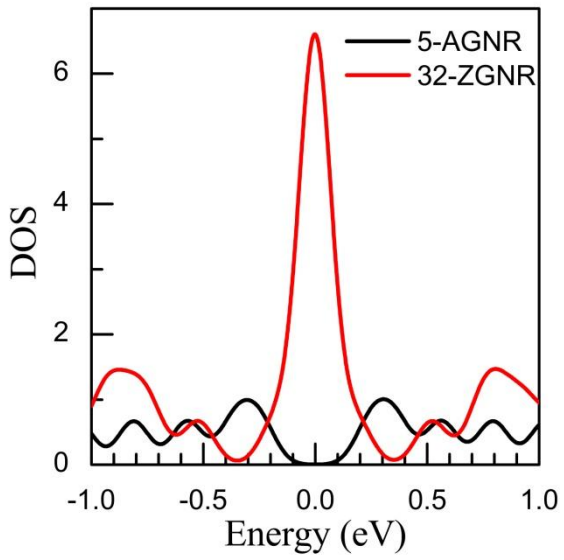

Fig. 6.5 (a) Γ-point DOS of 5-AGNR and 32-ZGNR calculated using DFT implemented in SIESTA.

6.1.1 Non-Decaying Property induced from the "3*j*" Pattern

We see from Fig. 6.1 to Fig. 6.3 that the bonding and antibonding states exhibit a "3*j*" wavefunction pattern, which is inherited from the HOGO and LUGO of infinite 3*p*+2-AGNRs. Here, we show that the non-decaying behavior in 3*p*+2-AGNRs can in fact be induced from this interesting "3*j*" pattern.

We have reviewed in Section 1.1.3 that *the sum of wavefunction projections on all nearest neighbors of any carbon atom has to vanish* for a Fermi level state, as described by Eqn. (1.6). Via this *nearest-neighboring sum rule*, Fujita *et. al.* has explained the decay behavior of the zigzag edge state towards its backland [11]. Such decay behavior is obvious in all junctions, such as those we show in Fig. 6.1 to Fig. 6.3. However, this decay argument does not apply to the narrow AGNR, as it is outside the backland of the zigzag edge.

Then, how would the wavefunction distribute over the narrow-AGNR region? For junctions with the narrow-AGNR in the 3*p*+2 family, the bonding and antibonding

states are distributed over the narrow 3*p*+2-AGNRs following a "3*j*" pattern: localized only on every two rows of carbon atoms, with every third row empty (Fig. 6.1 to Fig. 6.3). In such a pattern, each carbon atom has only two effective nearest neighbors with non-zero electron density. For example, site β in Fig. 6.6 (a) has only two effective neighbors B and C, since $c_D = 0$. According to the *sum rule*, the wavefunction coefficients on the two effective neighbors will be of the same magnitude but opposite signs. For example, $c_B = -c_A$ and $c_C = -c_B = c_A$ in Fig. 6.6 (a). This implies that the state does not decay along the AGNR.

We see from the above analysis that the absence of electron probability density on every third row is a sufficient condition for the non-decaying behavior. Such a "3*j*" pattern counting from both sides of an *n*-AGNR then requires the width *n* to be in form of $n = (2 + 1)p + 2 = 2 + (1 + 2)p = 3p + 2$.

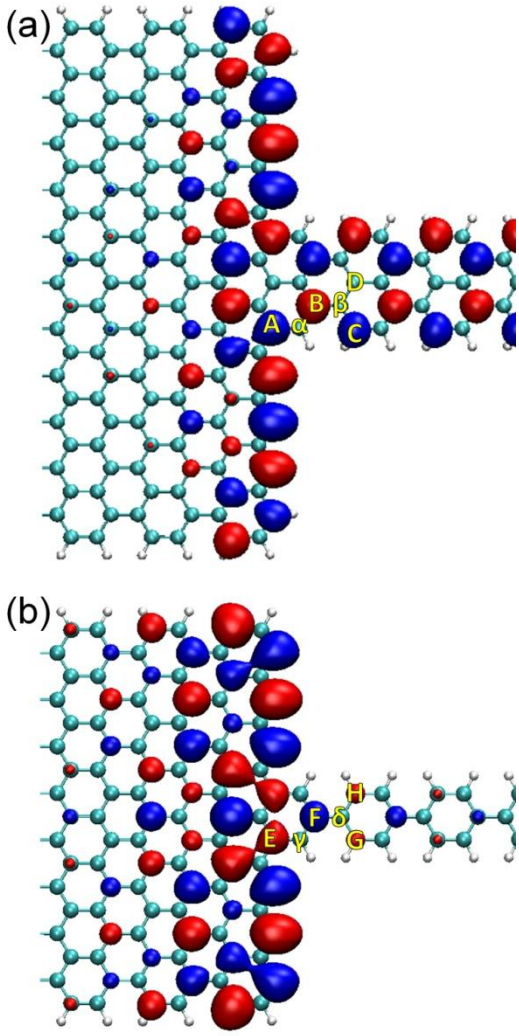

Fig. 6.6 Extension of the zigzag edge state into (a) 5-AGNR and (b) 3-AGNR. They are zooming-in of Fig. 6.1 (c) and Fig. 6.8 (c), respectively. A, B, C, etc indicate atomic sites at the occupied sublattice, whereas α, β, γ, etc represent atomic sites at the empty sublattice. Red/blue spheres are isosurfaces of the DFT wavefunctions with positive/negative isovalues. The radius of the spheres qualitatively indicate the magnitude of the electron density (hence the magnitude of the wavefunction coefficient) at an atomic site. Red/blue colors represent positive/negative signs of wavefunction coefficient.

As an opposite example, if the middle AGNR is of width $n = 3$, as shown in Fig. 6.6 (b), we show that the state decays into 3-AGNR. Like in the previous case, site γ (Fig. 6.6 (b)) has only two effective neighbors E and F, so $c_F = -c_F$. Site δ has three nearest neighbors F, G and H, then

$$c_F + c_G + c_H = 0 \quad (6.1)$$

Because site G and site H are symmetric with each other, we have

$$c_G = c_H \qquad (6.2)$$

Equations (6.1) and (6.2) together determines that

$$c_G = c_H = -\frac{c_F}{2} = \frac{c_E}{2} \qquad (6.3)$$

which means the state is decaying over the 3-AGNR segment by half per unit cell.

6.1.2 Width Dependence of the Bonding Antibonding Gap

As we have shown in Chapters 4 and 6, the bonding and antibonding states in a *w*-*n*-*w*-AGNR Z-Z junction with $n=3p+2$ originate from the HOGO and LUGO of the middle *n*-AGNR coupled to the zigzag edges at the two interfaces. Because of the zigzag edges playing as sources and drains, electrons are not confined within the middle *n*-AGNR, so the length *l* of the middle *n*-AGNR becomes unimportant in determining the energy of these states. Then, how does the bonding and antibonding energy splitting ΔE depends on the width *n* of the middle *n*-AGNR?

Figure 6.7 shows the tight-binding ΔE of a 65-*n*-65-AGNR junction as a function of *n*. This nearest-neighboring tight-binding model that has been shown to well reproduce the DFT results (see e.g. Fig. 4.2). We have also learnt from the tight-binding calculated $\Delta E(l)$ relationship of 23-5-23-AGNR junction (Fig. 4.2 and Fig. 5.4) that ΔE slightly decreases as *l* increases and converges to a constant value for $l > 20$ unit cells. Therefore, we set $l = 50$ unit cells in the 65-*n*-65-AGNR junction we are studying here, which is much longer than sufficient to give a converged ΔE.

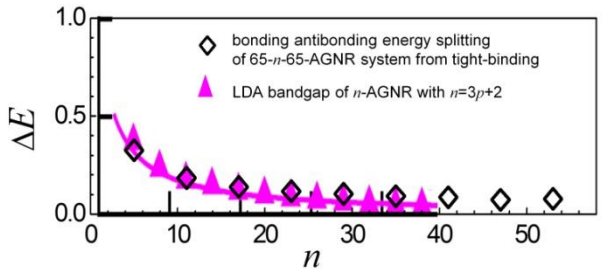

Fig. 6.7 The bonding antibonding energy splitting ΔE of a 65-n-65-AGNR junction as a function of the width n of the middle n-AGNR, calculated by solving the nearest neighboring tight-binding Hamiltonian. Here, $n = 3p+2 <= 53$. The length of 65-AGNR = 16 unit cells and length of the n-AGNR $l = 50$ unit cells. $\Delta E(n)$ is drawn on top of the LDA bandgaps of $3p$+2-AGNRs, adopted with permission from Fig. 2(b) of Ref. [12]. Copyright (2006) by the American Physical Society.

It is clear from Fig. 6.7 that the tight-binding ΔE of 65-n-65-AGNR junctions match very well to the LDA band gaps of the middle n-AGNRs [12]. This indicates that ΔE is mainly contributed from the middle n-AGNR region, consistent with our previous study in Fig. 5.4 using the example of 23-5-23-AGNR junction.

6.2 Decaying Extension into 3*p*- and 3*p*+1-AGNRs

For junctions with the middle AGNR in the $3p$ and $3p$+1 families, we also observed bonding and antibonding states that mimic the zigzag edge state and the HOGO/LUGO of the middle $3p$-AGNRs (Fig. 6.8 to Fig. 6.11) or the HOGO-1/LUGO+1 of the middle $3p$+1-AGNRs (Fig. 6.12 to Fig. 6.13).

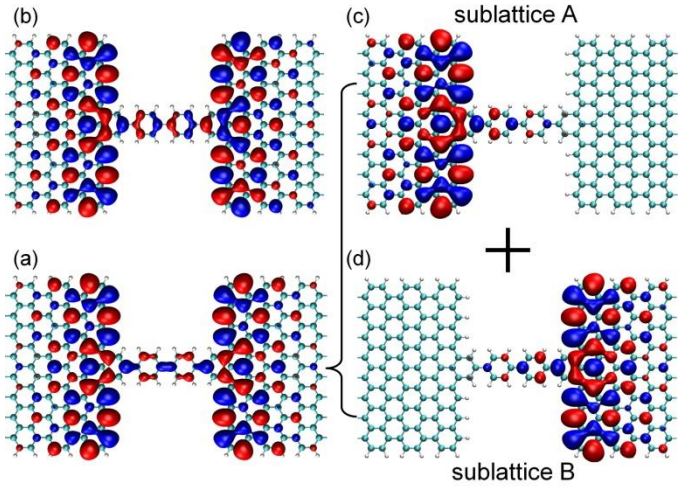

Fig. 6.8 The (a) bonding and (b) antibonding states in 17-3-17-AGNR junction, calculated using SIESTA under periodic boundary condition. (c-d) Contributions to the bonding/antibonding state from two sublattices. Isovalue = ±0.015 for all wavefunction isosurfaces.

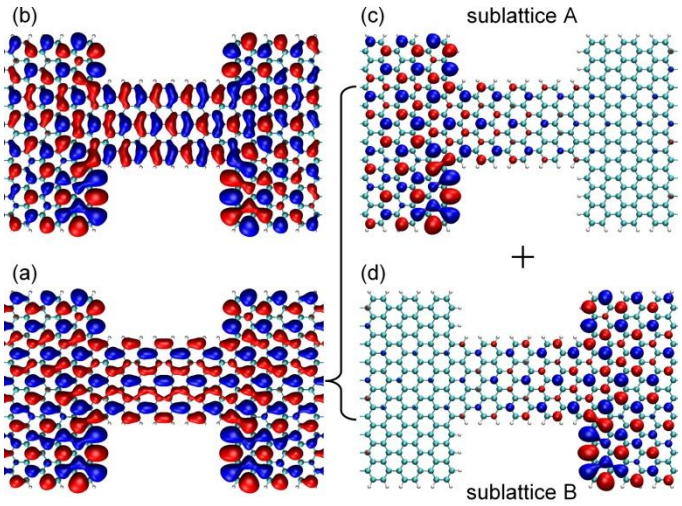

Fig. 6.9 The (a) bonding and (b) antibonding states in 21-9-21-AGNR junction, calculated using SIESTA under periodic boundary condition. (c-d) Contributions to the bonding/antibonding state from two sublattices. Isovalue = ±0.01 for all wavefunction isosurfaces.

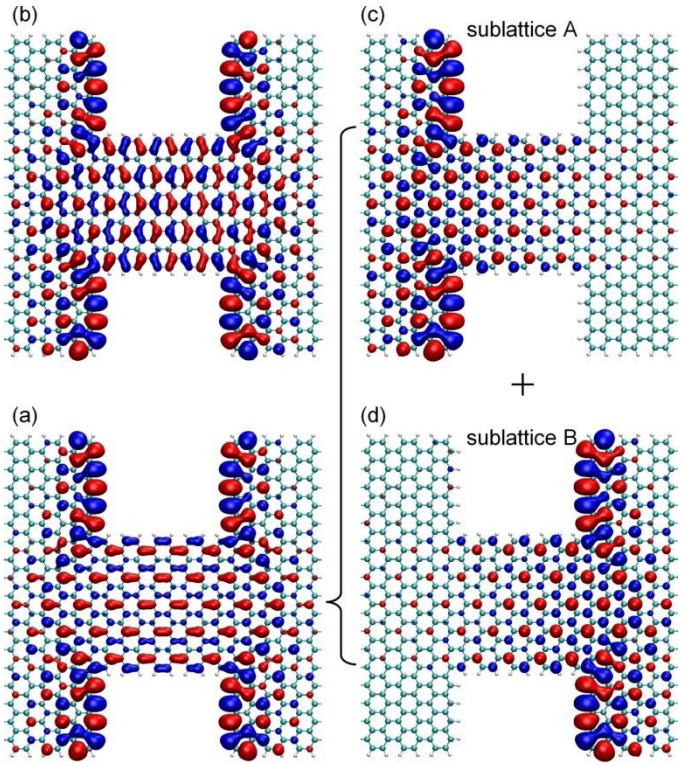

Fig. 6.10 The (a) bonding and (b) antibonding states in 35-15-35-AGNR junction, calculated using SIESTA under periodic boundary condition. (c-d) Contributions to the bonding or antibonding state from two sub-lattices. Isovalue = ±0.01 for all wavefunction isosurfaces.

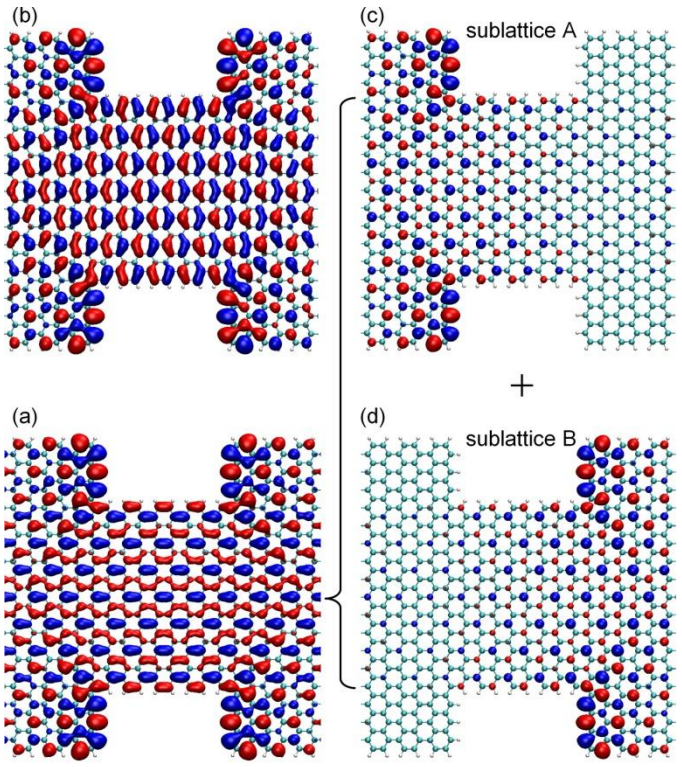

Fig. 6.11 The (a) bonding and (b) antibonding states in 35-21-35-AGNR junction, calculated using SIESTA under periodic boundary condition. (c-d) Contributions to the bonding or antibonding states from two sublattices. Isovalue = ±0.01 for (a-b) and ±0.02 for (c-d).

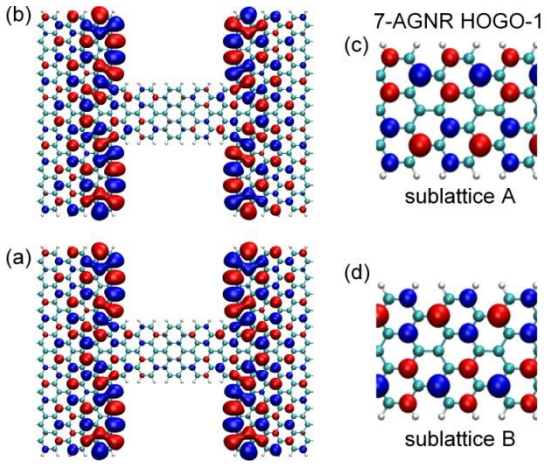

Fig. 6.12 The (a) bonding and (b) antibonding states in 25-7-25-AGNR junction. (c-d) Contributions to HOGO-1 and LUGO+1 of 7-AGNR from two sub-lattices. All wavefunctions are calculated using SIESTA under periodic boundary condition, and plotted with an isosurfaces value = ±0.08.

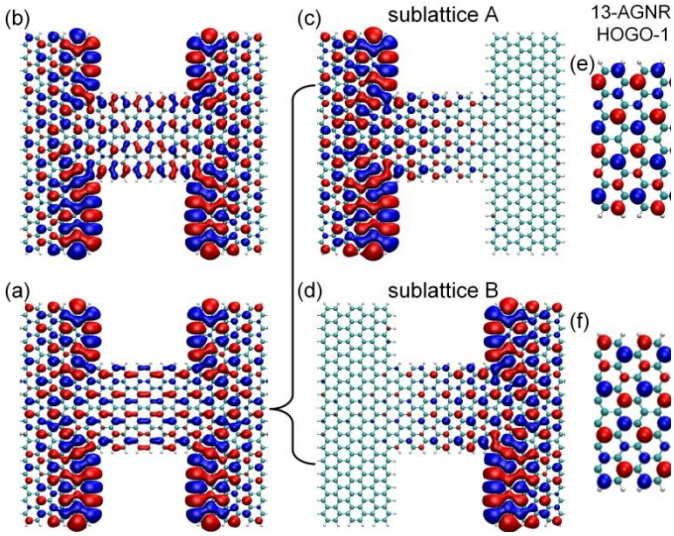

Fig. 6.13 The (a) bonding and (b) antibonding states in 33-13-33-AGNR junction. (c-d) Contributions to the bonding or antibonding states from two sublattices. (e-f) Contributions to HOGO-1 and LUGO+1 of 13-AGNR from two sublattices. All wavefunctions are calculated using SIESTA under periodic boundary condition, and plotted with an isosurface value = ±0.005 for (a-d) and ±0.05 for (e-f).

In addition, if we replace one of the zigzag edged interface with an armchair edged interface, such bonding and antibonding states are no longer observed. Instead, we see the original "zigzag + AGNR" state, as shown in Fig. 6.13 for the examples of 21-3-21- and 25-7-25-AGNR junctions. This is similar as what we observed in Fig. 5.3 (a) and confirms that the states shown in Fig. 6.8 to Fig. 6.13 are bonding and antibonding couplings of two "zigzag + AGNR" states.

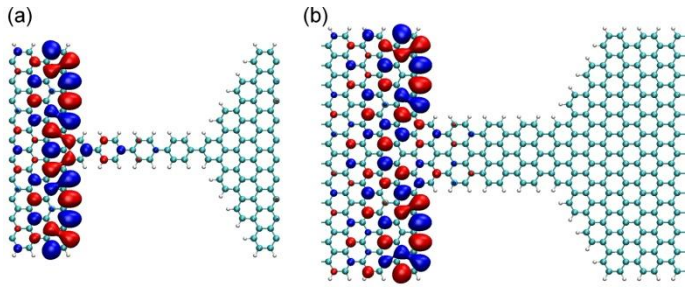

Fig. 6.14 The "zigzag + AGNR" state observed as a Fermi level eigenstate in (a) 21-3-21-AGNR Z-A junction and (b) 25-7-25-AGNR Z-A junction, obtained using DFT under periodic boundary condition. Isosurface = +/- 0.02 for both wavefunctions.

However, these states dramatically decay along the middle 3*p*- or 3*p*+1-AGNR from the zigzag edge side towards the opposite side. Such decaying tendency is especially obvious by looking at the contributions from each of the sublattices A or B. In addition to the fast decay, the energies of these bonding and antibonding states are extremely close to E_F.

6.2.1 Decay Rate from the Evanescent State approach

The extension of zigzag edge state into 3*p*- and 3*p*+1-AGNRs significantly decay because the gaps of 3*p*- and 3*p*+1-AGNRs are much wider than that of 3*p*+2-AGNRs (see Fig. 3.1) [12]. In this case, electrons and holes from the zigzag edge state see a huge energy barrier when they try to enter the HOGO/LUGO or HOGO-1/LUGO+1 of

the AGNRs. As a result, we expect that these electrons/holes penetrate into the AGNR as an evanescent state within the gap of the AGNR. As illustrated in Fig. 6.15, the evanescent state decays along the length l of the AGNR exponentially as $e^{-\alpha l}$, where the decay rate α can be obtained from the complex bandstructure of the AGNR.

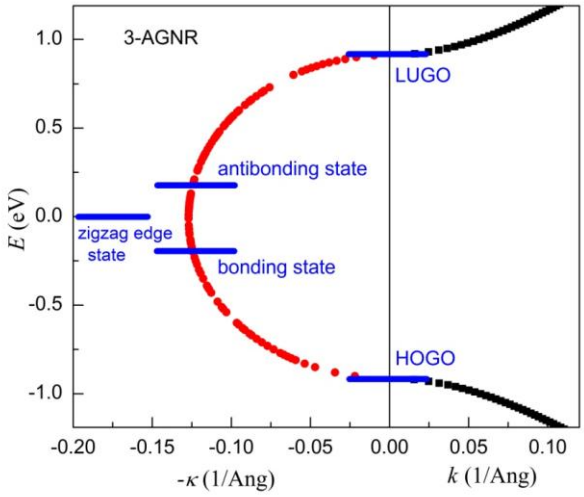

Fig. 6.15 The complex band structure of 3-AGNR, as an example to illustrate the bonding and antibonding states in AGNR-junctions as an evanescent sate penetrating the AGNR.

Exponential Fitting

In order to examine this evanescent state hypothesis, we first obtained the decay rate α of the bonding and antibonding states in each AGNR-junction by fitting the wavefunction to exponential function using MATLAB. We use the bonding state of 17-3-17-AGNR as an example to demonstrate the detailed procedures of the fitting. To distinguish the decaying from both sides, we take only the contribution from sublattice A φ_1, as shown in Fig. 6.16 (a). We then integrate the Local Density of States (LDOS) $|\varphi_1(x,y,z)|^2$ over the transverse dimensions x and y, to obtain a function of the longitudinal dimension z as

$$f(z) = \int |\varphi_1(x,y,z)|^2 \, dx \, dy$$

as plotted in Fig. 6.16 (b-c). Assuming that φ_1 decays along z following $Ae^{-\alpha z}$, then $f(z)$ would decay two times faster, i.e. following $Ae^{-2\alpha z}$. Since φ_1 is originated from the π-electrons, the electron density are localized at the carbon atoms rather than between them, so $f(z)$ is oscillating with a period (indicated by red arrow in Fig. 6.16 (b)) corresponding to the distance between two zigzag-shaped carbon chains. $f(z)$ shows a highest peak at the z position corresponding to the zigzag edge, and fast decays towards both sides. Here, we are interested on the $f(z)$ values on the right side of the highest peak, which corresponds to electron density over the 3-AGNR region. We then take the peak values of each oscillation on right of the highest peak, and fit them to $Ae^{-2\alpha z}$, as illustrated in Fig. 6.16 (c).

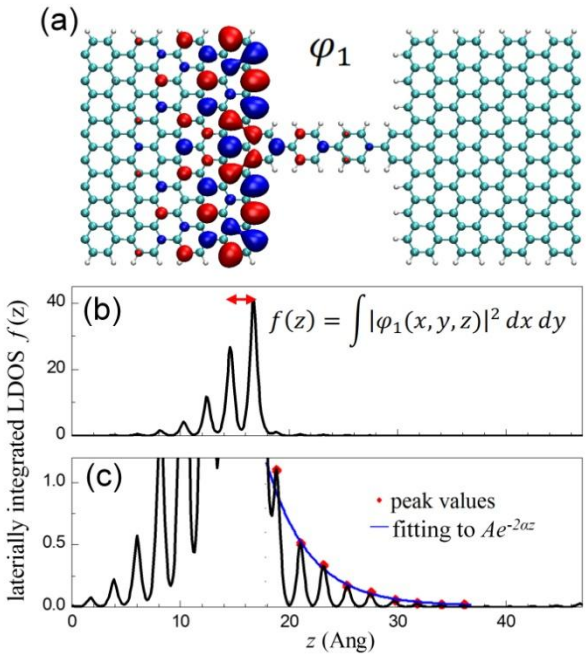

Fig. 6.16 (a) The sublattice A contribution to the bonding/antibonding state of 17-3-17-AGNR junction, which is also Fig. 6.8 (c), obtained from ψ_b and ψ_{ab} by $\varphi_1 = (\psi_b + \psi_{ab})/\sqrt{2}$. (b) The z-profile of corresponding electron density obtained as $f(z) = \int |\varphi_1(x,y,z)|^2 \, dx \, dy$. The red arrow indicates the wavelength of oscillations. (c) Zooming-in of (b) to see the peaks on the right side of the zigzag edge and fitting of the

peak values to $Ae^{-2\alpha z}$. Note that the first peak immediately on right of the zigzag edge is affected by the zigzag edge, so it is excluded in the fitting.

We see that the decaying over the 3-AGNR region fits very well to the exponential function. In fact, we obtained an adjusted R-square of 0.9936 for this particular fitting. The fitted decaying rate α = 0.1282 ± 0.0152 Å^{-1}. As the unit cell length over the 3-AGNR is ~4.32 Å, the decaying rate converts to 0.5538 ± 0.0657 per unit cell, which matches very well to the decay rate of half per unit cell we derived in Section 6.1.1.

We performed fittings via the same procedures for the bonding/antibonding state in other AGNR-junctions and all are fitted very well to the exponential function $Ae^{-2\alpha z}$. The fitted decaying rate α in various AGNR-junctions are summarized in Table 6.1.

Complex Bandstructures

On the other hand, we calculated the complex band structures of corresponding AGNRs using DFT implemented in ATK, as shown in Fig. 6.17. When the zigzag edge state extends into these AGNRs as an evanescent state, it follows the smallest κ that gives the slowest decay rate. We define the complex band giving the smallest κ at E_F as the lowest complex band. For all 3*p*-AGNRs shown in Fig. 6.17, the lowest complex band smoothly connects the lowest unoccupied real band and the highest occupied real band, forming one continues curve. The evanescent state with an κ value on this complex band will show the character of the HOGO and LUGO with an decaying envelop.

However, for the 3*p*+1-AGNRs, especially 7-AGNR, the lowest complex band connects the second lowest unoccupied and second highest occupied real bands. Because of this feature, the zigzag edge extends into the HOGO-1 and LUGO+1 of 3*p*+1-AGNR. This explains why the states shown in Fig. 6.12 to Fig. 6.13 mimic the

HOGO-1 and LUGO+1 rather than the HOGO and LUGO of 3*p*+1-AGNRs. In fact, we also observed states results from the zigzag edge state extending into the HOGO and LUGO of 3*p*+1-AGNRs, but decaying very fast to zero.

We extract the smallest complex wave number κ at the corresponding energy of the bonding/antibonding state for various AGNRs, as presented in Table 6.1.

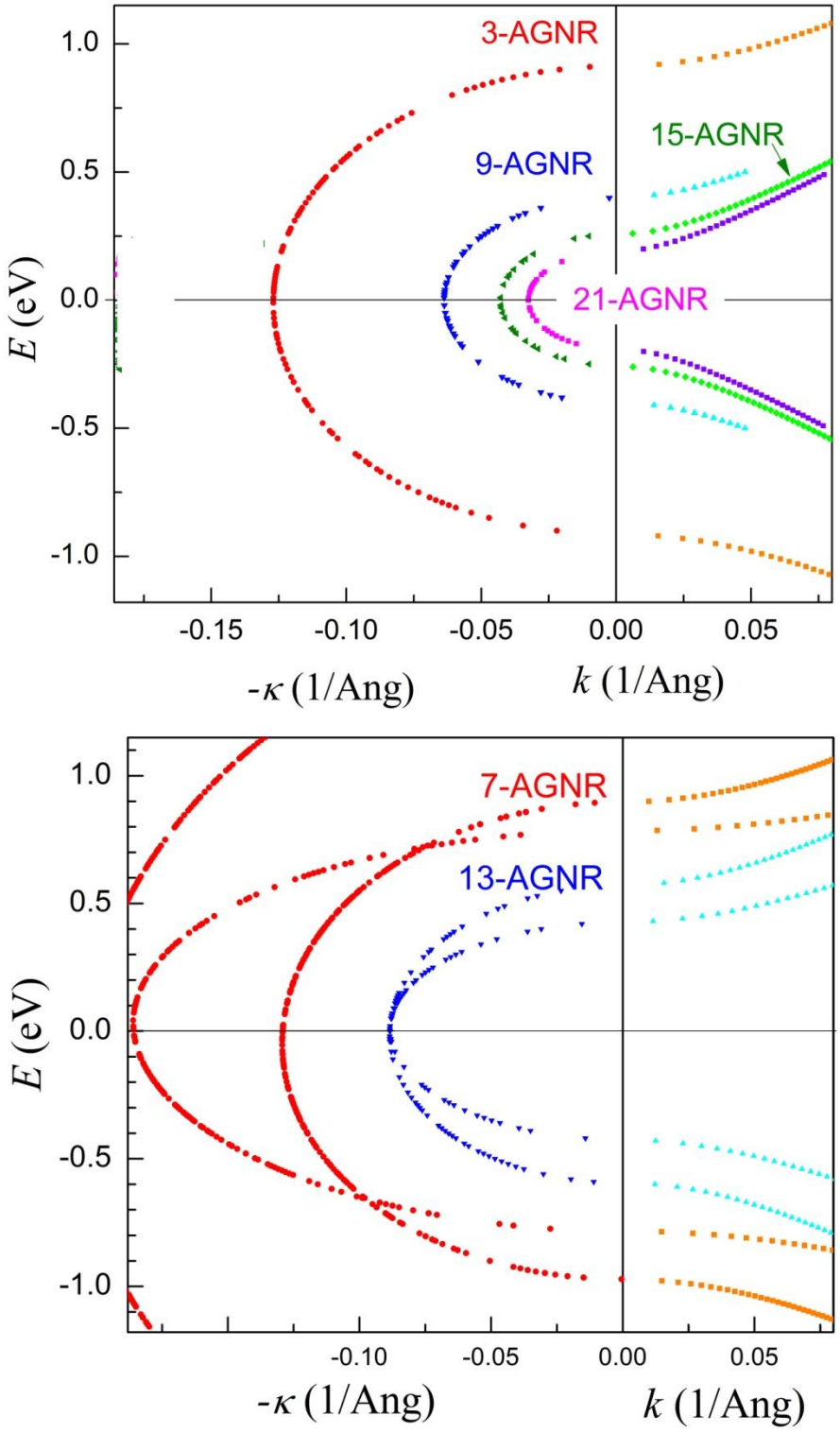

Fig. 6.17 The complex band structures of fully relaxed (upper panel) 3*p*- and (lower panel) 3*p*+1-AGNRs, calculated using DFT implemented in ATK with double-zeta polarized basis-set.

Comparison and Discussion

Table 6.1 Energy splitting ΔE and fitted decay rate α for the bonding/antibonding state in various AGNR-junctions (obtained from SIESTA calculation with double-zeta basis-set) vs the corresponding complex wave number κ and gaps in infinite n-AGNRs (obtained from ATK calculation with double-zeta polarized basis-set). The AGNR-junctions are all with the same length l = 4 for the middle AGNR (except 17-3-17-AGNR junction, where l = 3). Note that for 3p+1-AGNRs, we use the gaps and complex bands both corresponding to the HOGO-1 and LUGO+1, rather than HOGO and LUGO.

w-n-w-AGNR junction		ψ_b and ψ_{ab} splitting ΔE (eV)	n-AGNR gap (eV)	fitted α (Å^{-1})	κ at E = $\Delta E/2$ (Å^{-1})
n = 3p	17-3-17	0.01868	1.826078	0.1282 ± 0.0152	0.12704
	21-9-21	0.00819	0.800716	0.07134 ± 0.00416	0.06373
	35-15-35	0.03215	0.514635	0.05375 ± 0.00302	0.04280
	35-21-35	0.04882	0.381823	0.04260 ± 0.00289	0.03244
n = 3p+1	25-7-25	0.00154	1.869195	0.13077 ± 0.01096	0.12918
	33-13-33	0.00498	1.165442	0.09355 ± 0.0019	0.08846

It is very clear from Table 6.1 that the decay rate α and the complex wave number κ match very well for all 3p- and 3p+1-AGNR junctions we examined. This evidence confirms the hypothesis that the zigzag edge extends into the gaps of 3p- and 3p+1-AGNRs as an evanescent state.

In a Z-Z AGNR-junction, the extensions from zigzag edges on both interfaces overlap over the middle AGNR, so they couple to form a bonding state ψ_b with lower energy and an antibonding state ψ_{ab} with higher energy (Section 1.2 and Chapter 5). However, as extensions from both sides decay very fast, the overlap is very weak, so energy splitting between ψ_b and ψ_{ab} is extremely small, especially compared to the large gaps in 3p- and 3p+1-AGNRs (see Table 6.1). In the case where zigzag edge state extends into a 3p+2-AGNR without decay, the energy splitting between ψ_b and ψ_{ab} is invariant

with the length of the middle 3*p*+2-AGNR (Chapters 4-5 and Section 6.1). Here, as the extension of zigzag edge state into 3*p*- and 3*p*+1-AGNRs decays, the overlapping between extensions from two sides reduces as the middle AGNR lengthens, therefore the energy splitting between ψ_b and ψ_{ab} also decreases, and vanishes to zero when the middle AGNR is sufficiently long.

The AGNR junctions examined in Table 6.1 are all with the same length of l = 4 unit cells, except 17-3-17-AGNR junction. For junctions in both 3*p* and 3*p*+1 families, as the width of the middle AGNR increases, the energy splitting between ψ_b and ψ_{ab} also increases. This arises from the increased overlapping due to slower decay rate, which is attributed to the smaller gap of the middle *n*-AGNR.

6.3 Chapter Conclusion

We have showed in this chapter that the zigzag edge state extends into a 3*p*+2-AGNR as a non-decaying state because of the small gap in 3*p*+2-AGNRs. The non-decaying behavior can also be deduced from the "3*j*" wavefunction pattern of these states via the tight-binding sum rule. However, as 3*p*- and 3*p*+1-AGNRs have much wider gaps, the zigzag edge state can only extend into these AGNRs as an evanescent state with an exponential decay rate determined by the complex wave number.

As a result of the decaying behavior, the bonding and antibonding states in AGNR-junctions of the 3*p*+2 family exhibit invariant eigenenergies with respect to the length of the middle AGNR, while the bonding and antibonding eigenenergies in AGNR-junctions of the 3*p* and 3*p*+1 family approaches E_F as the middle ribbon lengthens.

Chapter 7. Large Magnetoresistance

We have seen in Chapters 4-5 that the states ψ_b and ψ_{ab} in a Z-Z AGNR-junction give rise to perfect transmission channels. Since the "zigzag + AGNR" state φ_1 (φ_2) is derived from the spin-polarized zigzag edge state, we expect these conducting channels will exhibit non-trivial spin-dependent phenomena. In fact, as we demonstrate in this chapter, we can destroy the transmission channels if we break the degeneracy of φ_1 and φ_2 by applying antiparallel spin-polarizations on two zigzag edge interfaces.

7.1 Spin-Polarized Transmission

In zigzag graphene nanoribbons, the spin up and spin down edge states are split in energy by ~0.5 eV within DFT [12], and larger when many-electron effects are taken into account [18]. Likewise, we expect here that each "zigzag + AGNR" state φ_1(φ_2) is split into two states with opposite spins $\varphi_1^{\uparrow}$ ($\varphi_2^{\uparrow}$) and $\varphi_1^{\downarrow}$ ($\varphi_2^{\downarrow}$), where the one with majority spin is shifted down in energy by the magnetic exchange energy term E_M and the other with minority spin is shifted up in energy by the same amount E_M. Crucially, because good coupling between these states requires them to be at the same energy, we expect that the spin orientation at the two zigzag edge interfaces can be used to control the coupling between the states, thereby closing or opening the channels for electron transmission. When the spin orientations at both zigzag edge interfaces are parallel (P configuration), the spin up (down) original states on both sub-lattices of the junction will still be at the same energy, and therefore can couple equally well as in the non-spin-polarized case. In contrast, when the spin at one zigzag-edge interface is pointed

in the opposite direction as the spin at the other zigzag-edge interface (antiparallel (AP) configuration), the spin up (down) original states at both sides of the junction will be at different energies, resulting in significantly reduced coupling and electron transmission.

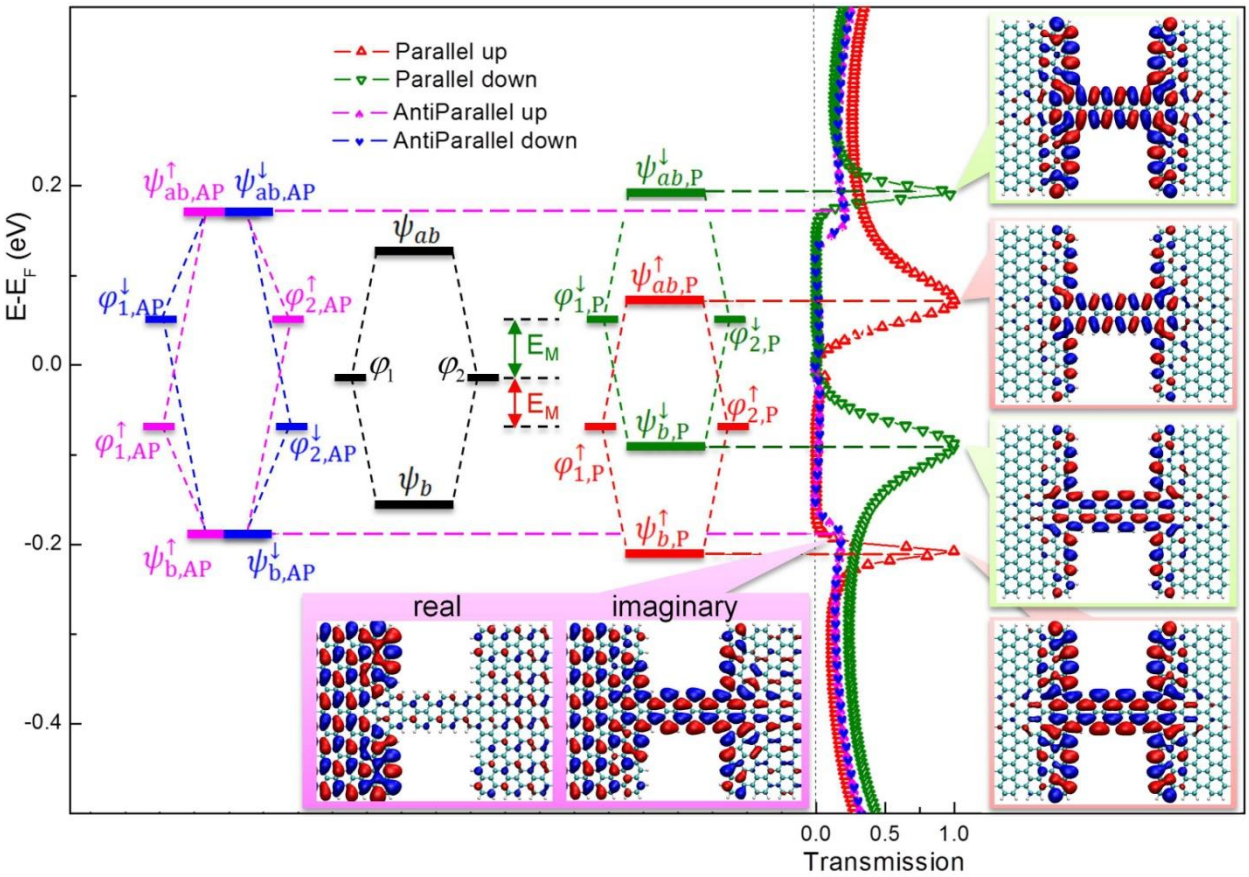

Fig. 7.1 Spin-polarized transmission curves of the 23-5-23-AGNR Z-Z junction with Parallel (P) and Antiparallel (AP) spins on two zigzag edge interfaces. Inset schematic: energy level diagrams illustrating the bonding and antibonding couplings of two original states in non-spin-polarized (middle black diagram), P (right red/green diagram), and AP (left pink/blue diagram) cases. Inset wavefunction isosurfaces (isovalue = +/- 0.025) on right side of transmission curve: real parts of eigenchannel wavefunctions at the four perfect transmission peaks for P case. Inset wavefunction isosurfaces (isovalue = +/- 0.005) on left side of the transmission curve: spin up eigenchannel wavefunction (real and imaginary parts) incident from the left at the bonding (loosely defined) peak of AP case.

The above hypothesis, illustrated in the energy level diagrams in Fig. 7.1 inset, is clearly supported by our first principles spin-polarized transmission results (Fig. 7.1).

For the P configuration, the computed spin up (majority) and spin down (minority) transmission curves both show two resonant peaks with transmission T ~ 1 close to E_F, but shifted lower and higher in energy relative to the non-spin-polarized case, respectively (Fig. 7.1, red/green curves). The eigenchannel wavefunctions at these perfect transmission peaks (Fig. 7.1 inset, right side) are exactly the bonding and antibonding states. In particular, when we construct the "original" states from spin-polarized eigenstates of the periodic structure by $\varphi_{1,\mathrm{P}}^{\uparrow} = \left(\psi_{b,\mathrm{P}}^{\uparrow} + \psi_{ab,\mathrm{P}}^{\uparrow}\right)/\sqrt{2}$ $(\varphi_{1,\mathrm{P}}^{\downarrow} = \left(\psi_{b,\mathrm{P}}^{\downarrow} + \psi_{ab,\mathrm{P}}^{\downarrow}\right)/\sqrt{2})$ and $\varphi_{2,\mathrm{P}}^{\uparrow} = \left(\psi_{b,\mathrm{P}}^{\uparrow} - \psi_{ab,\mathrm{P}}^{\uparrow}\right)/\sqrt{2}$ $(\varphi_{2,\mathrm{P}}^{\downarrow} = \left(\psi_{b,\mathrm{P}}^{\downarrow} - \psi_{ab,\mathrm{P}}^{\downarrow}\right)/\sqrt{2})$, we obtain essentially the same "original" states as in the non-spin-polarized case, as shown in Fig. 7.2.

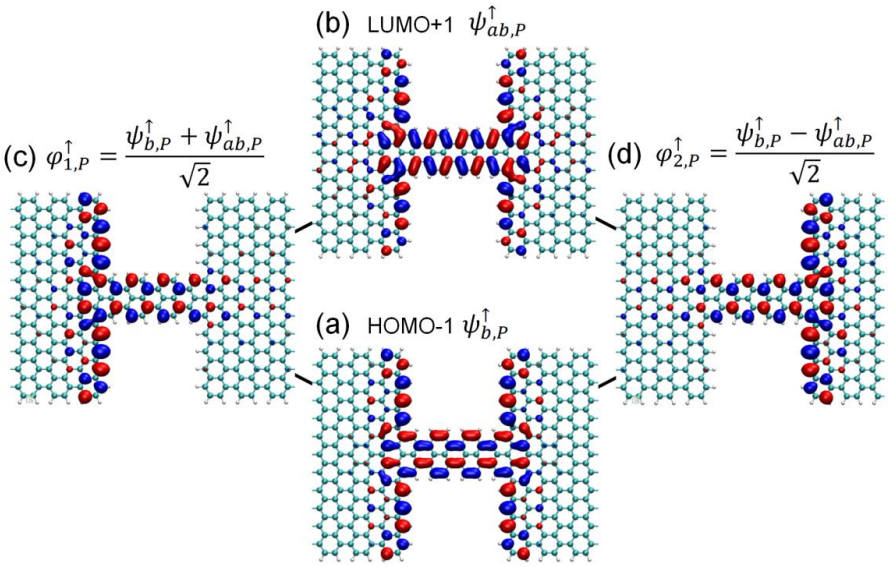

Fig. 7.2 The spin-up (a) bonding and (b) antibonding states of the 23-5-23-AGNR Z-Z junction with parallel spin-configurations on two zigzag edge interfaces, and the two original states (c) $\varphi_{1,\mathrm{P}}^{\uparrow}$ and (d) $\varphi_{2,\mathrm{P}}^{\uparrow}$ deduced from (a) and (b). All Isosurfaces are with isovalue = +/- 0.025. The spin-down bonding, antibonding, and original states show the same features.

On the other hand, the corresponding transmission peaks are significantly suppressed in the AP configuration (Fig. 7.1, pink/blue curves). The corresponding eigenchannel

wavefunction (Fig. 7.1 inset, left side) indicates that electrons coming from the left are reflected at the first (real part) or second (imaginary part) zigzag edge interface they encounter.

7.2 Spin-Polarized Current and Magnetoresistance

The significant difference in transmission spectra for P and AP configurations results in a large difference in the currents. As shown in Fig. 7.3 (a), the current in P configuration increases rapidly and almost linearly as the bias increases from 0.1 to 0.5 V, while the current in AP configuration remain very small until the bias voltage reaches ~ 0.4V. The AP current starts to slightly increase for bias voltage above 0.4V because the two small transmission peaks at ~ ±0.2 eV (Fig. 7.1 pink/blue curves) enter the bias window at bias ~ 0.4V.

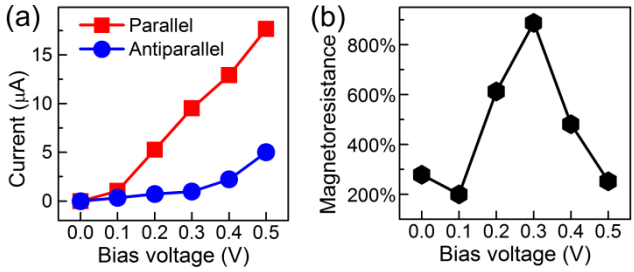

Fig. 7.3 (a) IV curves of the Z-Z junction with P and AP spin configurations. (b) Magnetoresistance of the junction at various bias voltages.

The large difference in currents of the P and AP cases then suggests that a large magnetoresistance (MR, defined as $\frac{I_P - I_{AP}}{I_{AP}} \times 100\%$) can be achieved in spin valve architectures based on this structure. Our MR results in Fig. 7.3 (b) indicate a large MR value reaching ~900% at the bias voltage of 0.3V. The MR peaks close to 0.3V because current in AP configuration starts to increase at ~0.4 V. We also verified from

our calculations that the magnetization is localized mainly on the zigzag edge interfaces and is not affected by the bias up to 0.5V.

7.3 Understanding the Width of Transmission Peaks

Figure 7.4 plots the transmission curves of the 23-5-23-AGNR Z-Z junction for the non-spin-polarized, Parallel spin-up, and Parallel spin-down cases together. We see an interesting feature that the width of the bonding and antibonding transmission peaks varies greatly among these three cases. Here we show that the origin of the difference in peak widths lies in the non-conducting zigzag edge state that produces a transmission valley.

7.3.1 Transmission Valley by the Non-Conducting Zigzag Edge State

For all the three transmission curves in Fig. 7.4 left panel, there is always a transmission valley with transmission probability T~0 between the bonding and antibonding transmission peaks. The log scale transmission curves (Fig. 7.4 right panel) show there exists a point with minimum transmission (T_min point) within the transmission valley for all three cases. Note that the local minima at E_F for all three cases are due to the gap in the 23-AGNR lead and irrelevant to our discussion here[6]. The eigenchannel wavefunctions at the T_min points (Fig. 7.4 right panel inset (a-c)) all indicate that the incoming wave enters the zigzag edge state localized at the zigzag edge interface of the incoming side and almost totally reflected by this interface (the state has no weight on the transmitted side no matter how low the isovalue is). This is

[6] An interesting point to note is that the scattering state SCARLET calculation (black curve) gives zero transmission in the gap, while the non-equilibrium Green's function TRANSIESTA calculation (red and green curves) still gives very small non-zero transmission in the gap, which we attribute to numerical errors.

consistent with the fact that transmission at the T_min point is almost zero. This non-conducting nature arises from the strong localization of the zigzag edge state, which prevents it from coupling to other states, especially states over the other side of the narrow ribbon.

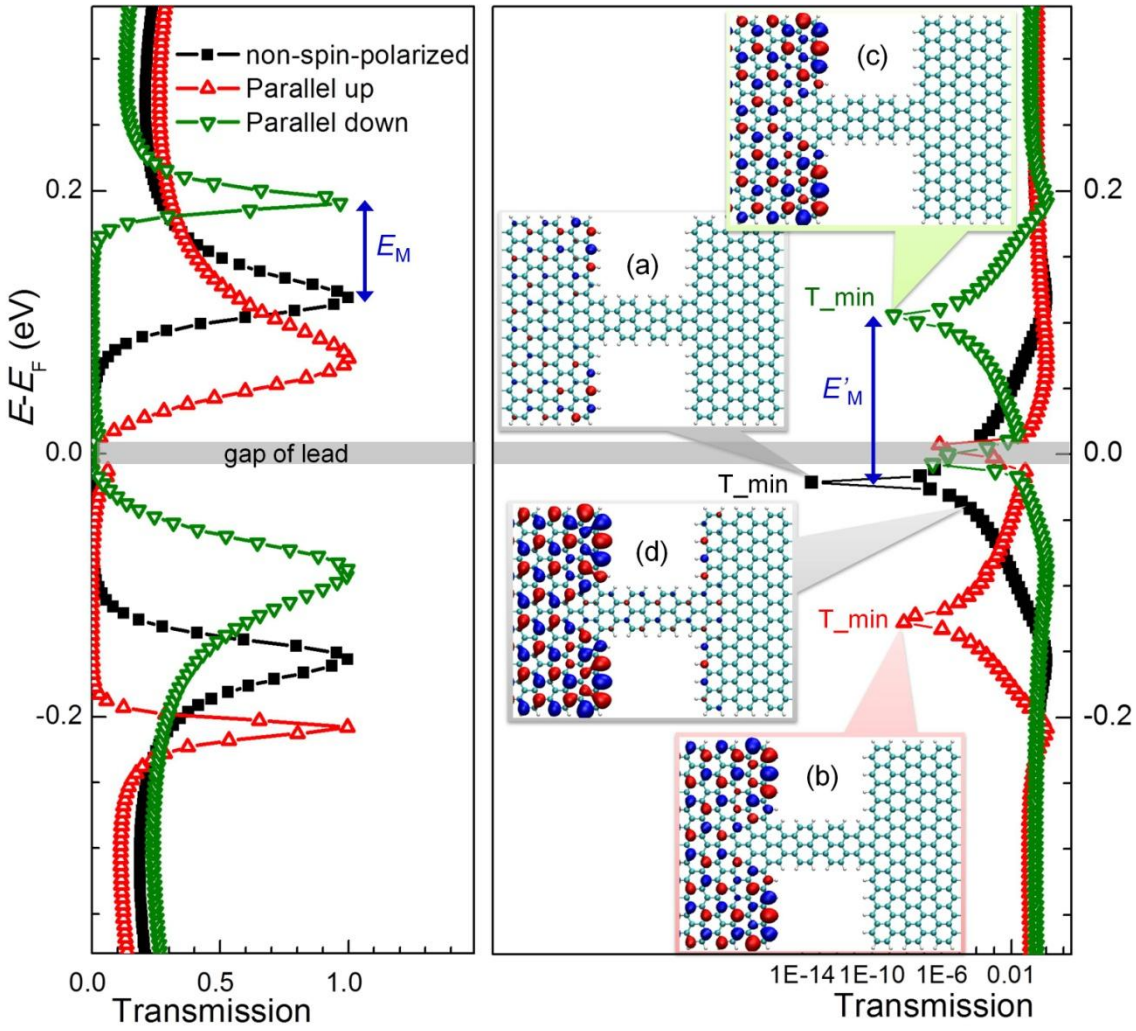

Fig. 7.4 Transmission curves of the 23-5-23-AGNR Z-Z junction without spin and with Parallel spins, plotted on (left panel) linear scale and (right panel) log scale. Inset (a-c): Real parts of eigenchannel wavefunctions, incident from the left side, at the lowest points (T_min) of the transmission valleys (the imaginary parts of the wavefunctions show similar features). Inset (d): Eigenchannel wavefunction at 0.04eV below T_min for the non-spin-polarized case. All wavefunction isosurfaces are with isovalue = +/- 0.015. E_M and E'_M represent the magnetic exchange energies for the "zigzag + AGNR" (φ_1) state and the zigzag edge state, respectively.

As we know, a conducting resonant state interacting with a uniform density of states in the electrodes produces a Lorentzian-shaped transmission peak. The width of the peak increases with the coupling strength between the resonant state and the states in the electrodes. Similarly, a non-conducting resonant state will produce a valley in the transmission spectrum, and the valley widens with increased coupling to the leads. The eigenchannel wavefunction at 0.04 eV below T_min point (Fig. 7.4 inset (d)) shows that majority of the incoming state still enters the zigzag-edge state and reflected back at the interface on the incident side, but a very small percentage of the incoming wave transmits to the other side. This confirms that states in the valley but away from the T_min point are still related to the zigzag edge state, hence suggests that the T~0 transmission valley is due to the non-conducting zigzag edge state.

7.3.2 Width of Transmission Peaks

For the non-spin-polarized case, the bonding and antibonding transmission peaks both fall off rapidly on the valley side, and the shapes of both peaks are roughly symmetric about E_F because the zigzag-edge state is almost mid-way in energy between the bonding and antibonding states. In the Parallel spin configuration, however, the spin-polarized zigzag edge state will split into two states. The one with majority spin shifts down in energy, whereas the one with minority spin shifts up, both by an magnetic exchange energy term E_M', similar as the splitting of the delocalized state φ_1 discussed in Section 7.1. We find that E_M' (~0.1eV from Fig. 7.4) > E_M (~0.06eV, from Fig. 7.4), which is consistent with the fact that the zigzag edge state here is more localized on the zigzag edge (where the magnetic moments also localized on) than is the "zigzag + AGNR" state φ_1. As a result, the corresponding zero-conductance zigzag edge state will be closer to the bonding state for spin-up (majority) case and closer to the

antibonding state for spin-down case, leading to asymmetric line widths for the bonding and antibonding peaks in the corresponding transmission curves.

7.4 Chapter Conclusion

In summary, we have demonstrated in this chapter that the transmission spectrum of AGNR junctions are spin-dependent, leading to a large magnetoresistance reaching 900% for 23-5-23-AGNR junction. The origin of the spin-polarization lies in the nature of the two frontier resonant states as bonding and antibonding couplings of original zigzag edge derived states. As the bonding and antibonding transmission channels are intrinsic for all AGNR junctions in the 3p+2 family, we expect the spin-polarized transport property can also be generalized to other AGNR junctions in the 3p+2 family. For AGNR junctions in the 3p and 3p+1 families, especially for long junction, these transmission channels becomes less conducting, therefore we expect the magnetoresistance will also be less.

Chapter 8. Negative Differential Resistance

We see from previous chapters that the bonding and antibonding transmission peaks of the AGNR Z-Z junction are very narrow and close to $E_{F.}$ Moreover, the AGNR-leads have a bandgap that can be well controlled by the width of the AGNR. The narrow transmission peaks and the gap in the leads provide very good conditions to obtain negative differential resistance (NDR), where an increase in voltage induces a decrease in current. This is an uncommon property and is very useful in many electronic device applications, including oscillators, amplifiers [87], switching, memory circuits [88], etc. In addition, NDR with low on-set bias and high peak-to-valley ratio is preferred for practical applications. In this chapter, we demonstrate in detail the NDR mechanism in AGNR junctions via the resonant tunnelling model [89] and show how AGNR junctions is advantageous to achieve high performance NDR.

8.1 the AGNR Junction and Transmission Properties

In our previous prototypical 23-5-23-AGNR junction, the gap of 23-AGNR is too narrow compared with the width of the bonding and antibonding transmission peaks. To obtain an effective NDR, here we choose 17-AGNR with a larger bandgap ~ 0.1eV [12] as the leads and form a 17-5-17-AGNR junction, as shown in Fig. 8.1 (a). To make it metallic, the 17-AGNR lead region is doped with 0.15% of B atoms via the Virtual Crystal Approximation [90]. This p-type doping shifts the E_F from the middle of gap to ~0.05eV below the valence band edge, as indicated in Fig. 8.1 (b).

The 17-5-17-AGNR junction shows two perfect narrow transmission peaks near E_F (Fig. 8.1 (b)). According to their eigenchannel wavefunction patterns, we can identify that these two transmission peaks arise from the well studied bonding and antibonding states (Chapters 4 and 5). As will be demonstrated in detail in next section, we can use a bias voltage to drive these peaks into the gap of leads to obtain NDR.

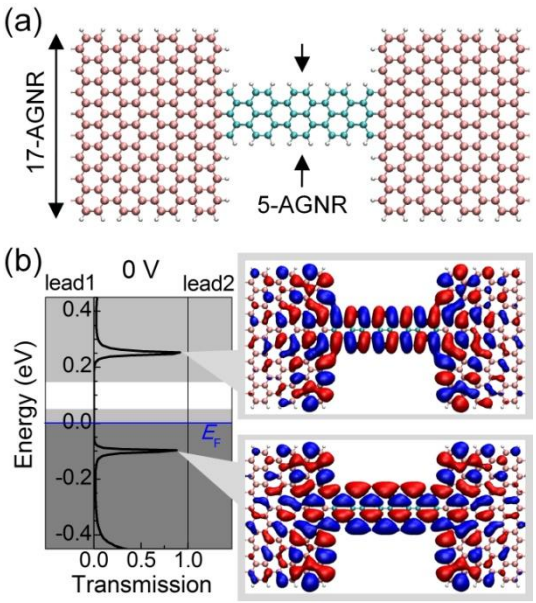

Fig. 8.1 (a) Atomic structure of 17-5-17-AGNR Z-Z junction. The 17-AGNR region is doped with 0.15% of B atoms via the Virtual Crystal Approximation [90]. (b) Transmission curve for the junction shown in (a) at zero bias. The dark and light gray shadings indicate occupied and unoccupied states in the leads, respectively. The white blank region indicates the gap of leads. Inset: the real parts of eigenchannel wavefunctions (isovalue = +/- 0.025) at the two transmission peaks (imaginary parts show similar features).

8.2 NDR and the Mechanism

Figure 8.2 (a) gives the IV curve of the 17-5-17-AGNR junction, where a NDR effect with an on-set bias of only 0.2V and a peak-to-valley current ratio > 6 is observed. This ratio is quite high compared to other systems such as the GNR-CNT cross bar system with a peak-to-valley ratio of 2 [91] and the Si-SiGe system with a peak-to-valley ratio of 5.2 [92].

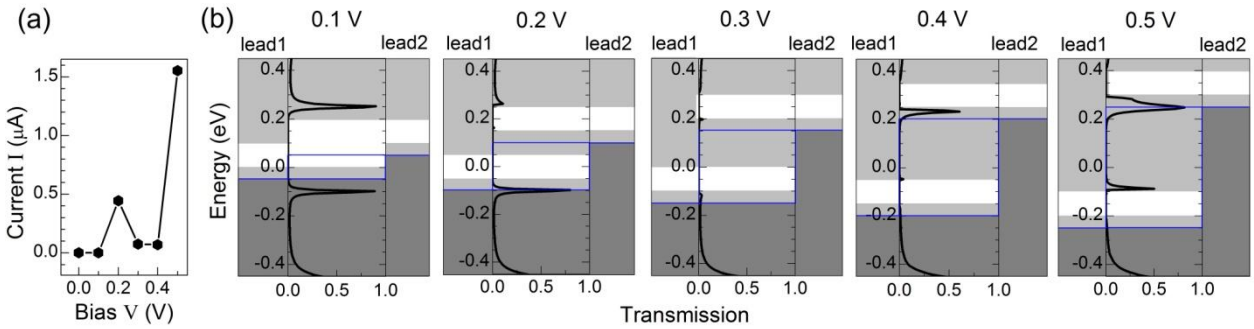

Fig. 8.2 (a) IV curve of the 17-5-17-AGNR junction shown in Fig. 8.1 (a). (b) Transmission spectrums of the junction with a bias of 0.1 to 0.5V. The dark and light gray shadings indicate occupied and unoccupied states in the leads, respectively. The white blank regions indicate the gaps of leads. The blue box indicates biased energy window, within which one lead is occupied and the other lead is unoccupied.

The NDR can be understood by examining the transmission curve as a function of the bias voltage, as shown in Fig. 8.2 (b). When we apply a bias of 0.1 V, the Fermi level of lead 1 (E_{F1}) drops by 0.05 eV and the Fermi level of lead 2 (E_{F2}) increases by 0.05 eV. This produces an energy window of 0.1eV with occupied states in lead 2 but empty states in lead 1, as indicated by the blue box. The current at low temperature is the integration of the transmission probability $T(E)$ within this energy window [77]

$$I = \frac{2e}{h}\int_{E_{\mathrm{F1}}}^{E_{\mathrm{F2}}} T(E)dE$$

Since the cumulative transmission probability falling into the energy window at the bias of 0.1V is almost zero, the current is also almost zero. As the bias increases to 0.2V, the bias window widens and partially covers the transmission peak initially below E_{F1}, which gives rise to a current up to ~ 0.444 μA. At the bias of 0.3V and 0.4V, although the bonding transmission state would be well within the energy window, it is however driven into the gap of lead 1, where there is no incoming electrons, hence giving no transmission. This leads to a significant drop of the current from ~ 0.444 μA at 0.2V to

only ~ 0.071 μA at 0.4V, thus results in a NDR with peak-to-valley ratio ~ 0.444/0.071 = 6.25. At a bias of 0.5V, as the gap of lead 1 shifts further down, the bonding peak partially emerges out of the gap. Moreover, the other transmission peak also starts to fall into the biased energy window, so together the two transmission peaks give rise to a current as large as ~ 1.6 μA. For bias beyond 0.5V, since both transmission peaks will fall into the biased energy window and will no longer be affected by the gaps of leads, we expect the current to increase further.

8.3 Advantages of AGNR-Junctions for NDR

We see from the mechanism of NDR that AGNR junctions possess many advantages to achieve the NDR with relatively low on-set bias and high peak-to-valley ratio. Firstly, the bonding and antibonding nature of the two transmission peaks determines that they are close to E_F. The bonding peak of the 17-5-17-AGNR Z-Z junction is only ~0.1 eV below E_F (Fig. 8.1 (b)). The closeness to E_F makes it easier to achieve NDR with a relatively low on-set bias.

Secondly, the eigenchannel wavefunctions (Fig. 8.1 (b)) of the transmission peaks also show that the two states are strongly localized over the middle AGNR region and the two zigzag edge interfaces, but relatively weakly coupled to the leads. Such localization is an intrinsic property originated from the zigzag edges (Chapters 4 and 5). On one hand, the weak coupling determines that the states are not perturbed much by the bias applied to the two leads. Figure 8.2 (b) shows that the energy and shape of these transmission peaks do not vary much as bias increases, except a suppression by the gap. In addition, the eigenchannel wavefunction at the bonding peak under a bias of as large as 0.5V (see Fig. 8.3) remains essentially the same as that at 0V (Fig. 8.1 (b)

inset), further confirming that the state is not perturbed much by the bias. It would be more difficult or even impossible to achieve NDR if these states were drifted away or destroyed by the bias. On the other hand, the weak coupling determines that the two transmission peaks are very narrow in energy width (< 0.05 eV), hence can be completely suppressed by the gap of the lead (~0.1eV for 17-AGNR, see Fig. 8.1 (b) and Fig. 8.2 (b)). In addition, there is no other transmission peaks nearby. Therefore, once the bonding peak enters the gap, we can achieve a valley current of almost zero.

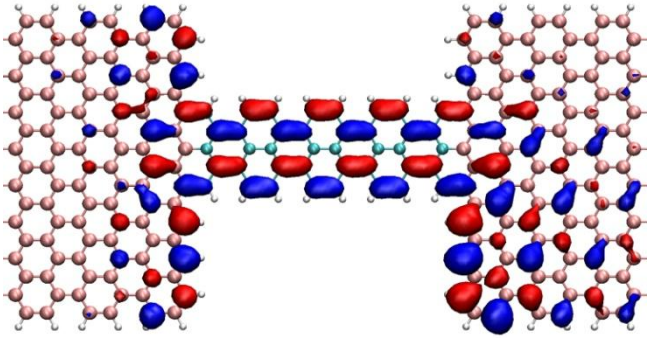

Fig. 8.3 Real part of the eigenchannel wavefunction with isovalue = +/- 0.025 at the bonding peak of 17-5-17-AGNR junction under a bias of 0.5V, as shown in Fig. 8.2 (b). The imaginary part show the same feature.

Thirdly, the two narrow transmission peaks close to E_F arise from the HOGO and LUGO of the middle AGNR (see Chapter 3, 4, 6), so they are intrinsic to the AGNR junction as long as there are zigzag edges at the interfaces. The gap in the AGNR lead is also intrinsic and can be well controlled through the width. Therefore, the high performance NDR that we demonstrated using the example of 17-5-17-AGNR can be generalized to other AGNR junctions. In addition, as we have demonstrated in Chapter 4, these transmission peaks do not shift away from E_F as the ribbon lengthens for AGNRs in the $3p$+2 family. This unique property allows that the device can be extremely long-ranged. For AGNRs in $3p$- and $3p$+1 families, as the ribbon lengthens,

the transmission peaks approach the Fermi level and may immerge into the gap (Chapter 6), while the peak height (transmission probability) also attenuates to zero, so there would a length limitation for the NDR device.

Fourthly, these intrinsic channels still persist when the junction is put on graphene or BN substrates (Fig. 8.4). This can be understood since the two interesting states are originated from the π-electrons, which do not couple strongly to these substrates. Therefore, we expect the high performance NDR would also be robust against substrates.

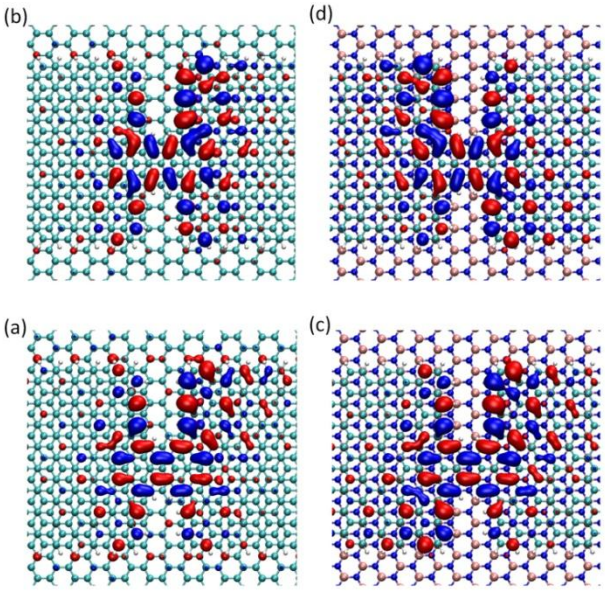

Fig. 8.4 The bonding (a, c) and antibonding (b, d) states with isovalue = +/- 0.025 of a 17-5-17-AGNR junction on a graphene (a-b) or boron nitride (c-d) substrate.

8.4 Junctions made by Hydrogenization

So far, we have been demonstrating NDR in an etched AGNR junction. In fact, the perfect transmission channels giving rise to NDR is originated from spatial extension of the zigzag edge state, which is related to the π-orbitals of carbon atoms (Chapter 5 - 6; [11]). Therefore, we expect an equivalent AGNR junction of π-orbitals (rather than

carbon atoms) is enough to exhibit the bonding and antibonding states and the relevant effects. Figure 8.5 (a) shows one such junction of π-orbitals made from perfect 17-AGNR by passivating the π-electron of extra carbon atoms with a hydrogen atom other than etched these atoms off; we call this a hydrogenised junction. This hydrogenised junction shows essentially the same transmission curve at zero bias (Fig. 8.5 (c)) as that of an etched junction (Fig. 8.1 (b)). The eigenchannel wavefunctions at the two narrow peaks close to E_F (Fig. 8.5 (d)) also look similar as the eigenchannels determining the NDR in an etched 17-5-17-AGNR junction (Fig. 8.1 (b)), confirming that the nature of the channels are the same. As a result, this hydrogenised junction gives an IV curve (Fig. 8.5 (b)) also similar to that of the equivalent etched junction, which exhibits an NDR with the same on-set voltage of 0.2 V and a peak-to-valley ratio ~18.6.

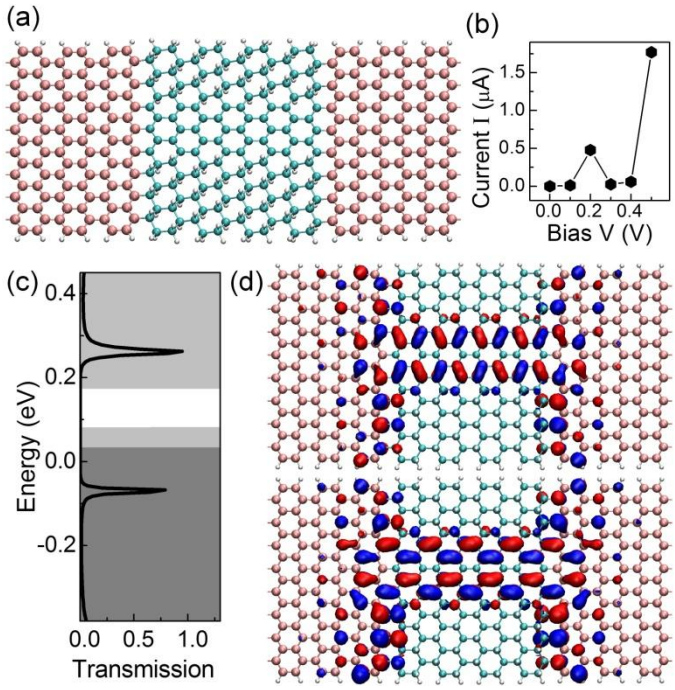

Fig. 8.5 The (a) geometry structure, (b) IV curve, and (c) transmission curve at zero bias of the 17-5-17-AGNR Z-Z junction made from 17-AGNR by hydrogenization. (d) The real parts of eigenchannel wavefunctions at the two perfect transmission peaks with isovalue = +/- 0.08. Imaginary parts show similar features.

8.5 Chapter Summary

In conclusion, we have demonstrated NDR in AGNR-junction via the resonant tunnelling model by utilizing an intrinsic transmission channel and the gap of the semiconducting AGNR-leads. The intrinsic channel is close to EF, weakly coupled to the leads, and without any other channels nearby. All these properties help to give a very low on-set voltage and high peak-to-valley ratio for the NDR. Moreover, the intrinsic channel hence the resulting NDR effect is robust against effects from substrates, and whether the junction is made by etching or hydrogenization, both providing great convenience in practical applications.

Chapter 9. Disorder Effects

So far, we have been assuming perfect AGNR junctions. In practice, it is difficult to experimentally make such perfect nanostructures, and many kinds of disorders may occur. From this practical point of view, it is important to study how various types of disorder affects the two interesting and useful states in AGNR junctions with a 3*p*+2-AGNR in the middle region. As the two states originate from the zigzag edge state coupled to states in the narrow 3*p*+2-AGNR (Chapters 4, 5, and 6), we expect disorders at the zigzag edge and the narrow 3*p*+2-AGNR would affect more on the two states. In this chapter, we discuss two types of disorders: 1) roughness at the zigzag edge interface and 2) an extra H atom over the narrow 3*p*+2-AGNR.

9.1 Zigzag Edge Interface Roughness

Since the bonding and antibonding states originate from the zigzag edge state that extends into an AGNR in the front side of the zigzag edge, the atomic structure at the interface connecting the zigzag edge and the AGNR is especially important. So far, we have been assuming that the zigzag edge segment at the interface connects to the narrow-AGNR at one end, and connects to the armchair edge of the wide-AGNR at the other end, both with a well defined 90^0 corner, as shown in Fig. 9.1 (a). Such well defined connection on both sides of the zigzag edge segment requires the width of the wide-AGNR exceeding that of the narrow-AGNR by an odd number. Namely, the total number of carbon atoms along the zigzag edge segment has to be an odd number.

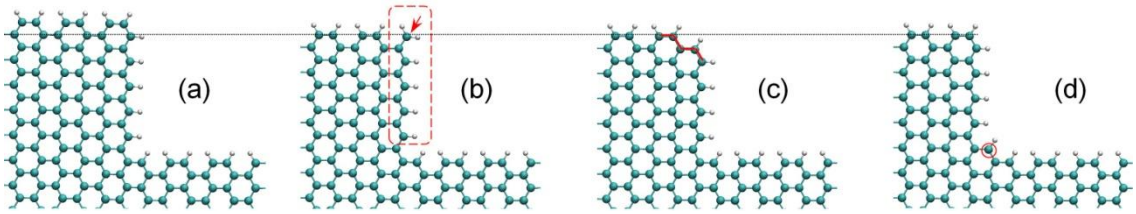

Fig. 9.1 Possible atomic structures at the zigzag edge interface.

If this number becomes even, as shown in Fig. 9.1(b), there will be a carbon atom at the outer end of the zigzag edge segment (indicated by red arrow in Fig. 9.1(b)) that is bonded to only one carbon atoms and passivated with two hydrogen atoms. This carbon atom will be more active and makes the structure less stable. We may modify the structure by deleting this unstable carbon atom to obtain a structure as shown in Fig. 9.1(c). This generates a very short zigzag edge smoothly connecting the vertical zigzag edge and the armchair edge of the wide-AGNR. An alternative modification is to delete the whole zigzag chain indicated by the red box in Fig. 9.1(b), generating a structure shown in Fig. 9.1(d). However, there will be a carbon atom left at the corner between the zigzag edge and the armchair edge of the narrow-AGNR, as indicated by the red circle in Fig. 9.1(d). If we remove this carbon atom, there will be two passivating hydrogen atom being at the same place, which is not stable.

Next, we examine how is the "zigzag + AGNR" state affected by the different atomic structures at the interface using a Z-A junction under periodic boundary condition. As shown in Fig. 9.2, the Fermi level "zigzag + AGNR" state survives in all four junctions. For structures with a shorter zigzag edge (four edge atoms, Fig. 9.2(c-d)), there is only one Fermi level state that exhibiting a positive and negative oscillation of wavefunction value along the zigzag edge atoms. However, for structures with a longer zigzag edge (five edge atoms, Fig. 9.2(a-b)), there are two such Fermi level states, one of exhibiting

a node with negative wavefunction value on two adjacent edge atoms, as indicated in Fig. 9.2 (a1) and (b1). The extra carbon in structure (b) traps more electron probability than the usual zigzag edge atoms. The short zigzag edge in structure (c) (highlighted in red in Fig. 9.2 (c)) enhances extension of the zigzag edge state into the 5-AGNR, while the extra carbon at the zigzag edge – 5-AGNR corner (indicated by red circle in Fig. 9.1(d)) prohibits the extension. Based on these observations, we expect that the "zigzag + AGNR" state as well as the bonding and antibonding states will be robust against the detailed atomic structure at interface as long as we have a zigzag edge.

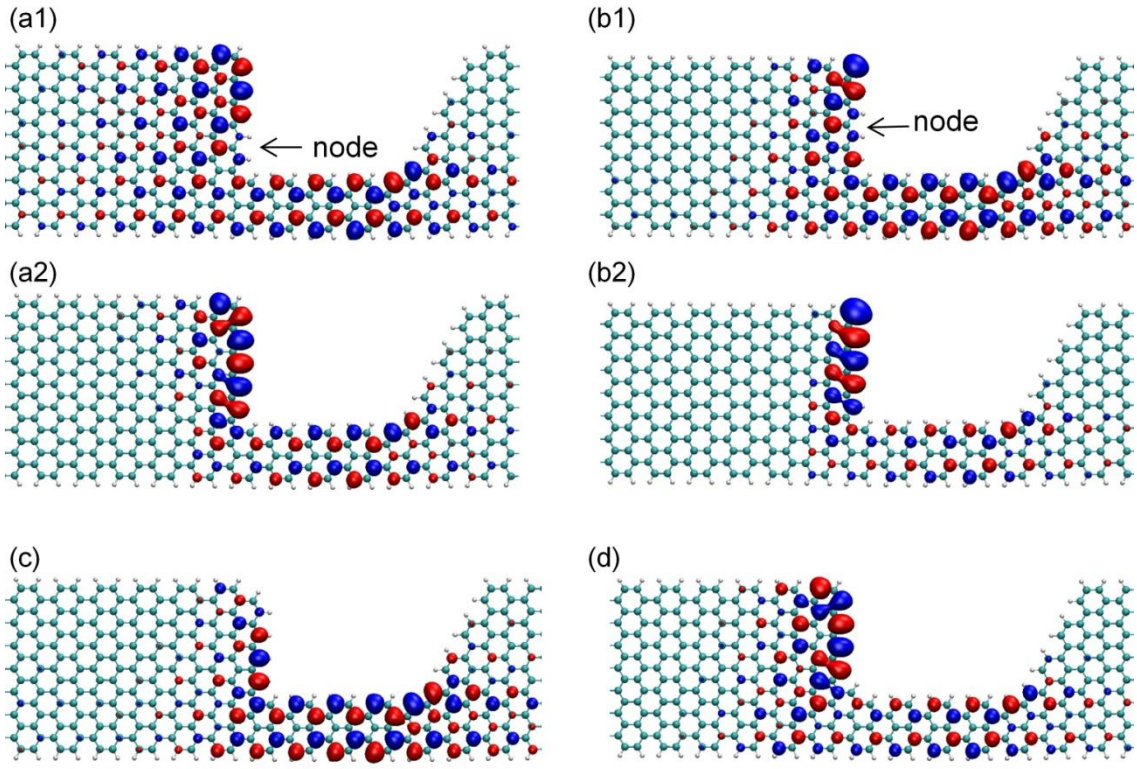

Fig. 9.2 The Fermi level "zigzag + AGNR" states in four AGNR Z-A junctions. The atomic structures at the zigzag edge interface in (a-d) corresponds those shown in Fig. 9.1 (a-d), respectively. The wavefunction magnitude over the 5-AGNR region slightly increases from left to right. This could be due to the short zigzag edge at the corner between the 5-AGNR and the armchair edge at the right interface.

9.2 Extra H atom over the narrow-AGNR

The bonding and antibonding states arise from the π-electron of carbon atom in an sp^2 configuration (we have confirmed this in Section 8.4). An extra H atom forms bond with this π-electron, hence may destroy the bonding and antibonding states. Without loss of generality, we still use the 23-5-23-AGNR Z-Z junction to examine the effects of having an extra hydrogen atom over the narrow 3*p*+2-AGNR region. An extra H atom could be bonded to a carbon atom of the middle 5-AGNR at the first, second, or third rows, as shown in Fig. 9.3, which stabilizes the system by -1.61eV, -1.06eV, and -0.22eV compared with the perfect junction, respectively.

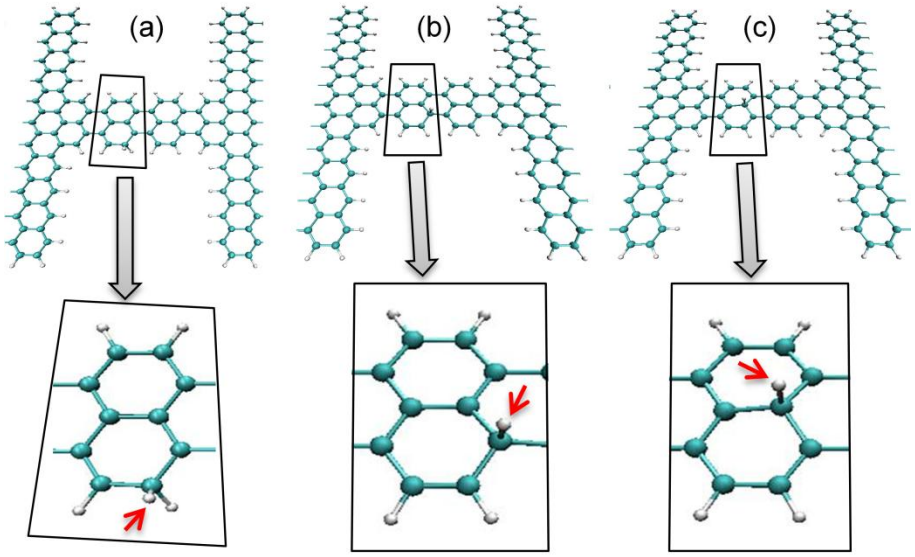

Fig. 9.3 Atomic structures of 23-5-23-AGNR Z-Z junction with an extra H atom (indicated by red arrow) bonded to carbon atoms on the (a) first, (b) second, or (c) third row counting from the armchair edge. The length of the middle 5-AGNR l = 3 unit cells for all junctions.

The transmission curves of these three defected junctions and the perfect junction are given in Fig. 9.3. For junctions with an extra H atom on the 1st and the 2nd rows of the 5-AGNR, the bonding and antibonding transmission peaks disappear, indicating that

the bonding and antibonding states are destroyed by the extra H atom. However, for the junction with an extra H atom on the 3rd row of the 5-AGNR, the bonding and antibonding transmission peaks survive. This could be understand from the unique "3*j*" wavefunction pattern over the 5-AGNR region: absence of wavefunction distribution on the $(3j)^{th}$ rows of carbon atoms (Fig. 4.1 and Figs. 6.1 to 6.3). We expect that for AGNR junctions with much wider 3*p*+2-AGNRs in the middle, an extra hydrogen atom bonded to a carbon atom in the $(3j)^{th}$ rows will not destroy the bonding and antibonding states.

We also note that the two peaks of the junction with an extra H atom on the 3rd row slightly shifted lower in energy, compared to that of the perfect junction. This arises from the n-type doping effect by the extra H atom, which slightly lifts the Fermi level. This result implies that we may dope the AGNR junction system by putting H atoms on carbon atoms in the $(3j)^{th}$ rows without destroying the two interesting states.

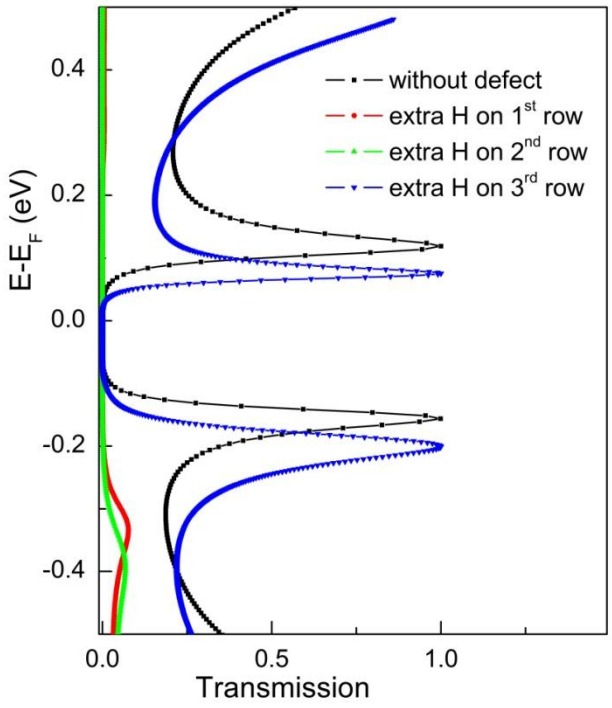

Fig. 9.4 The transmission spectra of the three defected junctions shown in Fig. 9.1 and of a perfect junction.

9.3 Chapter Summary

In this Chapter, we have discussed the effects from two types of disorders. Results show that the bonding and antibonding states tend to be robust against the detailed atomic structure at the interface, as long as there is a zigzag edge. However, the bonding and antibonding states are more fragile to disorders over the narrow 3*p*+2-AGNR, as the non-decaying extension relies on a locally repeating property. Once such repeating property is destroyed, the state would be hardly survive any more. For example, we have showed that an extra H atom bonded to a carbon atom over the 5-AGNR will destroy the bonding and antibonding states unless this carbon atoms is in the empty $3j^{th}$ row.

Chapter 10. Overall Conclusion and Outlook

In summary, we find that the zigzag edge state can extend into an AGNR in front of the zigzag edge. Such extension results in a non-decaying state for AGNRs in the 3*p*+2 family and an exponentially decaying evanescent state for AGNRs in other families. In particular, the non-decaying extension liberates the zigzag edge state from the localized nature, potentially leading to many more interesting phenomena. In an AGNR-junction with two zigzag edge interfaces on both sides of the middle 3*p*+2-AGNR, states originated from zigzag edges on both interfaces couple to form perfect transmission channels. The zigzag edges serving as sources and drains to liberate electrons in these channels from confinement within the 3*p*+2-AGNR. Therefore, the eigenenergies of these channels are independent on the length of the 3*p*+2-AGNR segment. This property makes AGNR-junctions in the 3*p*+2 family excellent molecular wires showing invariant conductance with respect to length. In addition, our results o the spin-polarized transmission suggest that these perfect transmission channels can be tuned with a magnetic field to obtain a large magnetoresistance. By utilizing theses transmission channels and the gap in the semiconducting AGNR leads, we can also obtain high performance negative differential resistance via the resonant tunneling mechanism.

Possible future developments of this project include but not limited to

1) Based on the fact that the zigzag edge state can extend without decay into an 3*p*+2-AGNR, we can design many other applications utilizing the non-decaying extension. For example, we expect the zigzag edge state and its non-decaying

extension into 3*p*+2-AGNR can serve as a conducting channel that turns direction by 90^0. With this as the building units, we would be able to design nanoscale conducting channels of any desired shape. In addition, we can control the opening/closing of each section of the channel using a magnetic field.

2) Besides the states derived from the zigzag edge, we observed another type of interesting states in 3*p*+1-AGNR junctions whose patterns over the middle 3*p*+1-AGNR look like the HOGO and LUGO of 3*p*+1-AGNs, as shown in Fig. 10.1 (a-b) for 25-7-25-AGNR junction as an example. What's more, these states also show a localization at the zigzag edges.

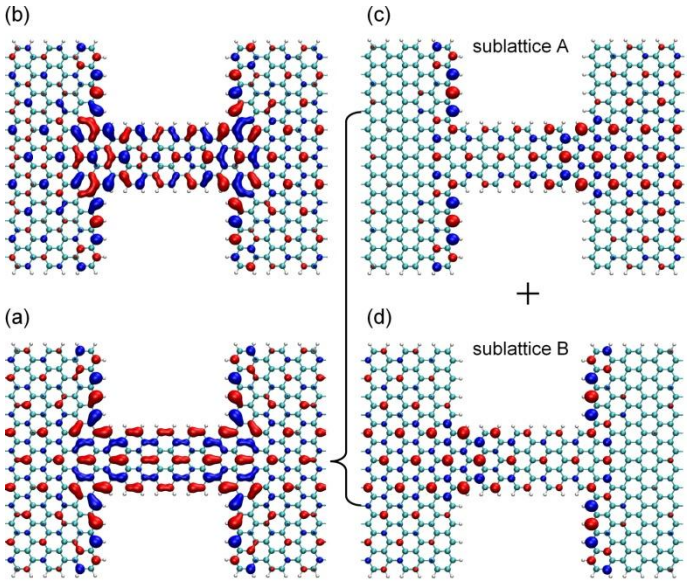

Fig. 10.1 (a-b) Two states in 25-7-25-AGNR periodic structure, at energies of -0.35eV and 0.35eV, respectively. (c-d) Contributions to each of the two states from sublattices A and B.

However, separating the contributions from the two sublattices, the state seems increasing inside the middle AGNR from the zigzag edge side towards the opposite side. We are still not sure of the reason for this increasing yet, but this implies the state in the middle AGNR may not be derived from the zigzag edge.

In order to find out the necessity of the zigzag edge for these states, we studied two reference junctions with one or both of the zigzag edge interfaces replaced by armchair edge interfaces, i.e. a Z-A and an A-A junction as shown in Fig. 10.2. Interestingly, we also observed two states in both the Z-A and the A-A junction with the pattern inside the middle 3*p*+1-AGNR mimic the HOGO and LUGO of an infinite 3*p*+1-AGNR and the pattern at any zigzag edge mimic the zigzag edge state, as shown in Fig. 10.2.

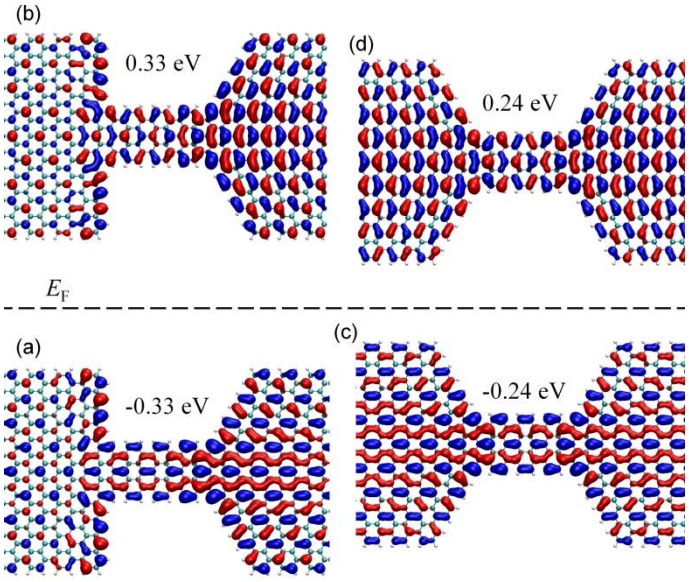

Fig. 10.2 Two states in 25-7-25-AGNR (a-b) Z-A and (c-d) A-A periodic structures.

The states shown in Fig. 10.2 (especially those for the A-A structure) definitely do not rely on the zigzag edge. So we can tell that the two states shown in Fig. 10.1 (a-b) are of the same nature. Namely, these states may be related to the HOGOs and LUGOs of the middle 3*p*+1-AGNR, but they are not derived from the zigzag edge, although the state show localization at the zigzag edge.

These two interesting states worth further investigation.

Appendix A. Mathematical Induction Proof of the Length-Independence of Eigenenergy

The *l*-independence of eigenenergies of the anomalous states discussed in Chapter 4 mainly results from the locally repeating pattern in the wavefunction. For a 23-5-23-AGNR Z-Z periodic structure, let $P^{(m)}$ be the proposition that *for l = m, there exists an eigenstate with m locally repeating units within the 5-AGNR region and this eigenstate has eigenenergy E independent of l.* Here, we present a mathematical proof of this proposition by induction.

Step 1) We show that $P^{(3)}$ is true.

For *m* = 3, the eigenwavefunction patterns of the bonding state and antibonding state of 23-5-23-AGNR Z-Z periodic structure each includes 3 locally repeating units in the 5-AGNR region, with each unit consisting of two zigzag-shaped carbon columns, as qualitatively shown in the DFT eigenstate results in Fig. 5.2 (a) and (b). We also plot the exact values of coefficients $c_i^{(m=3)}$ of the bonding state $\boldsymbol{\psi}_{bonding}^{(m=3)}$ calculated by tight-binding method in Fig. 4.3 (b). The zoomed-in plot for the coefficients projected in the 5-AGNR region shows clearly 3 locally repeating units, each consisting of $2n = 2\times5 = 10$ coefficients.

Step 2) We show that if $P^{(m)}$ is true, then $P^{(m+1)}$ is also true.

Suppose for a 23-5-23-AGNR Z-Z periodic structure with *l* = *m*, we have the Hamiltonian $\boldsymbol{H}^{(m)}$ and an eigenwavefunction $\boldsymbol{\psi}^{(m)}$ with eigenenergy *E*

$$\boldsymbol{H}^{(m)}\boldsymbol{\psi}^{(m)} = E\boldsymbol{\psi}^{(m)} \qquad \text{(A1)}$$

Mathematically, $\boldsymbol{\psi}^{(m)}$ is an eigenvector whose elements are coefficients projected at each carbon atom *i* out of the *N* atoms in the whole structure.

$$\boldsymbol{\psi}^{(m)} = \begin{pmatrix} c_1^{(m)} \\ c_2^{(m)} \\ \vdots \\ c_i^{(m)} \\ \vdots \\ c_N^{(m)} \end{pmatrix} \qquad \text{(A2)}$$

Assume the coefficients projected at the 5-AGNR segment is locally repeating, and group $c_i^{(m)}$ within each repeating unit as a sub-vector v, we can represent $\boldsymbol{\psi}^{(m)}$ as

$$\boldsymbol{\psi}^{(m)} = \begin{array}{|c|} \hline v_{23-\mathrm{AGNR}} \\ \hline v \\ \hline v \\ \hline \cdot \\ \cdot \\ \cdot \\ \hline v \\ \hline \end{array} \quad \} \; m \text{ sub-vectors } v \qquad \text{(A3)}$$

where $v_{23-\mathrm{AGNR}}$ is a sub-vector consisting of coefficients projected at carbon atoms in the 23-AGNR region.

Substituting (A2) into the matrix multiplication Eqn. (A1), we can represent it as a series of *N* equations

$$\sum_{j=1}^{N} H_{ij}^{(m)} c_j^{(m)} = E c_i^{(m)} \qquad \text{(A4)}$$

where $H_{ij}^{(m)}$ is the element *ij* of the Hamiltonian matrix $\boldsymbol{H}^{(m)}$, representing the hopping interaction between atom *i* and atom *j*, and *i* runs from 1 to *N*.

Including interactions up to third nearest neighboring zigzag columns, which covers 1st to 7th nearest neighboring carbon atoms, is more than enough to describe the physics of graphene [12, 29]. For convenience, we define neighbors within third nearest zigzag-shaped columns as local neighbors. With this definition, local neighbors for the 5-AGNR region are within the same and nearest locally repeating unit cells. Therefore, the interaction parameter between atom *i* and its neighbor *j* outside the local neighbor definition would vanish $H_{ij}^{(m)} = 0$, and Eqn.(A4) can be simplified to

$$\sum_{j=local\ neighbor} H_{ij}^{(m)} c_j^{(m)} = E c_i^{(m)} \qquad \text{(A5)}$$

From the eigenstate $\boldsymbol{\psi}^{(m)}$, we can insert one more locally repeating sub-vector v (as illustrated in Fig. 4.1 (e)) and renormalize the wavefunction by multiplying an scaling down parameter λ to manually construct an eigenstate $\boldsymbol{\psi}^{(m+1)}$ as

$$\boldsymbol{\psi}^{(m+1)} = \lambda \begin{bmatrix} v_{23-AGNR} \\ v \\ v \\ \cdot \\ \cdot \\ \cdot \\ v \end{bmatrix} \quad m+1 \text{ sub-vectors } v \text{ (A6)}$$

We show that $\boldsymbol{\psi}^{(m+1)}$ constitutes an eigenstate of $\boldsymbol{H}^{(m+1)}$ (the Hamiltonian of the periodic structure with $l = m+1$) with the same eigenenergy E, i.e.

$$\boldsymbol{H}^{(m+1)}\boldsymbol{\psi}^{(m+1)} = E\boldsymbol{\psi}^{(m+1)} \quad \text{(A7)}$$

Considering again only interactions with local neighbors, Eqn.(A7) can be simplified to a series of $N+2n$ equations (n is the number of carbon atoms across the width of n-AGNR, and $2n$ is the number of atoms in one locally repeating unit)

$$\sum_{j=local\ neighbor} H_{ij}^{(m+1)}\, c_j^{(m+1)} = E c_i^{(m+1)} \quad \text{(A8)}$$

For convenience, we arrange the coefficients $c_i^{(m+1)}$ of $\boldsymbol{\psi}^{(m+1)}$ in such a sequence that coefficient projected on the newly inserted $2n$ atoms are attached at the end of the vector, although geometrically they are inserted in-between two sub-vectors v.

We discuss the validity of eqns. (A8) for i in three cases: Case 3) is the newly inserted sub-vector v; Case 2) are the two sub-vectors v neighboring with the extra v; and Case 1) includes the rest $N-4n$ atoms that are inherited from $\boldsymbol{\psi}^{(m)}$ but excluding Case 2).

For the N coefficients $c_i^{(m+1)}$ inherited from $c_i^{(m)}$, there is only a scaling down by a parameter λ, i.e.

$$c_i^{(m+1)} = \lambda c_i^{(m)} \quad \text{(A9)}$$

For Case 1), both the atoms $c_i^{(m+1)}$ and their local neighbours $c_j^{(m+1)}$ satisfy Eqn.(A9). The local interactions also remain the same, i.e.

$$H_{ij}^{(m+1)} = H_{ij}^{(m)} \quad \text{(A10)}$$

Hence Eqns. (A8) for *i* runs within these *N*-4*n* atoms can be further simplified exactly to the series of equations (A5), which are already valid by assumption.

Case 2) is almost same as Case 1) except that one neighboring sub-vector *v* is replaced with a newly inserted but exactly same sub-vector *v*, so Eqn.(A8) also holds for these 4*n* atoms.

For Case 3), the atoms $c_i^{(m+1)}$ and their local neighbors $c_j^{(m+1)}$ (within the same and the nearest locally repeating unit cells of narrow-AGNR) are exactly a copy of another sub-vector v plus its two neighboring sub-vectors v, hence they will all satisfy equation (A8).

Summing up Cases 1), 2), and 3), all *N*+2*n* coefficients $c_i^{(m+1)}$ of $\boldsymbol{\psi}^{(m+1)}$ satisfy the Schrödinger equation (A8). Hence we have proved $\boldsymbol{\psi}^{(m+1)}$ is an eigenstate of $\boldsymbol{H}^{(m+1)}$ with the same eigenenergy E, i.e. $P^{(m+1)}$ is true.

With $\boldsymbol{\psi}_{\text{bonding}}^{(m=3)}$ as a starting point, according to Step 2), we can construct an eigenstate $\boldsymbol{\psi}_{\text{bonding}}^{(m)}$ for any $m > 3$ with the same eigenenergy E. This explains why the eigenenergies of the bonding and antibonding eigenstates are almost independent of the number of locally repeating units in the 5-AGNR region. This proof indicates that as long as there exists a starting eigenwavefunction $\boldsymbol{\psi}^{m\geq 3}$ containing *m* locally repeating units, we can construct an eigenwavefunction *with the same eigenenergy* for a longer structure by inserting more locally repeating units.

Appendix B. Family of the wide-AGNR

In the main text of the whole thesis, we have been focusing on the zigzag edge interface and the narrow-AGNR. In particular, when the narrow-AGNR is in 3*p*+2 family, the zigzag edge state at the interface will extend into this 3*p*+2-AGNR without decay. Otherwise, the state decays inside the narrow-AGNR exponentially. In contrast to the important role the family of the narrow-AGNR plays, the family of the wide-AGNR makes little difference to the peculiar "zigzag + narrow-AGNR" states. For example, the bonding and antibonding states are also observed in a 19-5-19-AGNR and a 27-5-27-AGNR (Fig. B.1), where the wide-AGNR is in 3p+1 and 3p family, respectively.

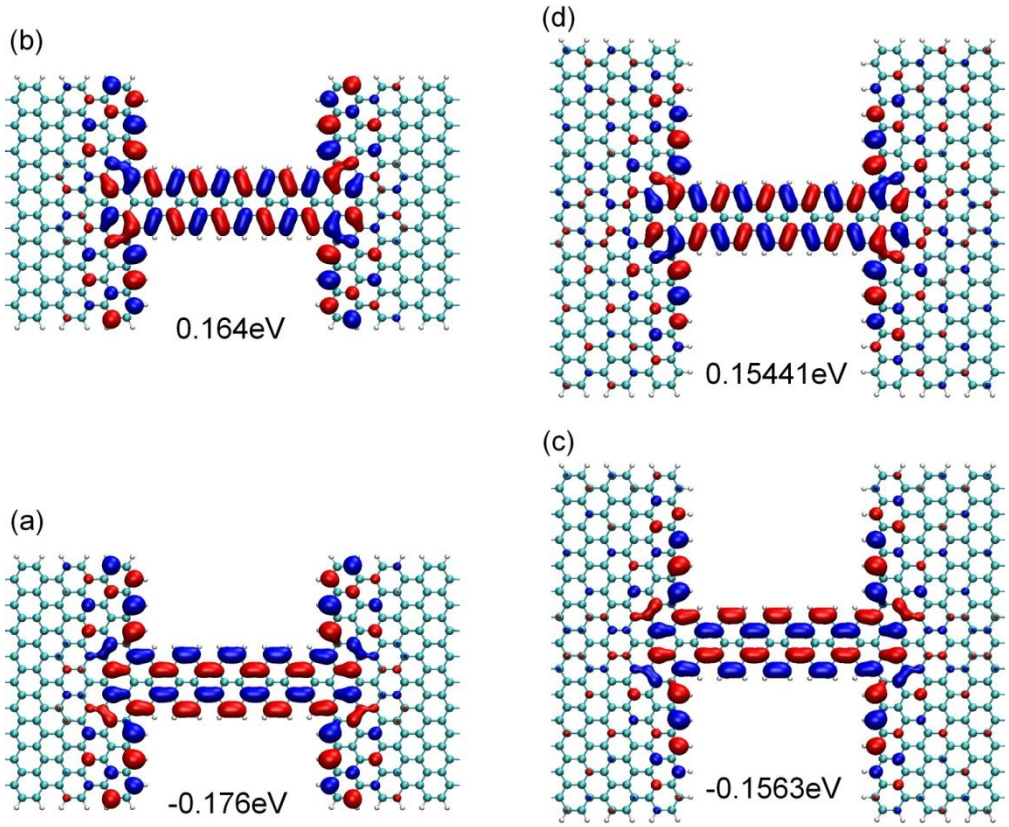

Fig. B.1 The (a, c) bonding and (b, d) antibonding states in (a-b) 19-5-19- and (c-d) 27-5-27-AGNR Z-Z junctions. Isovalue = +/- 0.025 for all wavefunction isosurfaces. The number show the energy of these states relative to the Fermi level.

However, these bonding and antibonding states are at energies very close to the Fermi level. When we use a narrow-gap 3*p*+2-AGNR as the leads, the bonding and antibonding states both give rise to a transmission channel with conductance reaching 1. However, if we use a wide-gap 3*p*- or 3*p*+1-AGNR [12] as the leads, although the bonding and antibonding states still well survive, they immerse into the wide gap of the leads and does not give rise to a transmission channel. As shown in Fig. B.2, the transmission spectra of the 19-5-19- and 27-5-27-AGNR junctions both show a wide gap (~ 1V) cantered around $E_{F,}$ within which there is no incoming state to transmit through the bonding or antibonding state. However, we expect that the bonding and antibonding states will conduct as well as in the 23-5-23-AGNR junction if we drift them out of the gap using e.g. a bias.

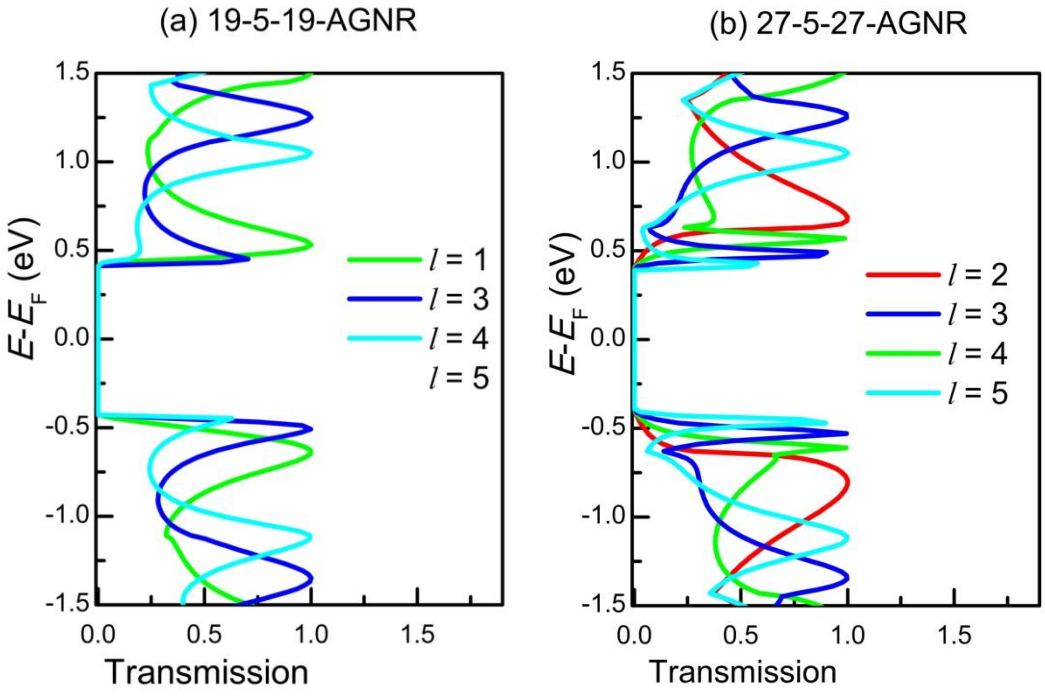

Fig. B.2 The transmission spectra of (a) 19-5-19- and (b) 27-5-27-AGNR Z-Z junctions with a varying length *l* of the 5-AGNR.

References

1. Novoselov, K.S., A.K. Geim, S.V. Morozov, D. Jiang, Y. Zhang, S.V. Dubonos, et al., *Electric field effect in atomically thin carbon films.* Science, 2004. **306** (5696): p. 666.

2. Novoselov, K.S., A.K. Geim, S.V. Morozov, D. Jiang, M.I. Katsnelson, I.V. Grigorieva, et al., *Two-dimensional gas of massless dirac fermions in graphene.* Nature, 2005. **438** (7065): p. 197.

3. Geim, A.K. and K.S. Novoselov, *The rise of graphene.* Nature Materials, 2007. **6** (3): p. 183.

4. Andrei, E.Y., G.H. Li, and X. Du, *Electronic properties of graphene: A perspective from scanning tunneling microscopy and magnetotransport.* Reports on Progress in Physics, 2012. **75** (5): p. 056501.

5. Wakabayashi, K., Y. Takane, M. Yamamoto, and M. Sigrist, *Electronic transport properties of graphene nanoribbons.* New Journal of Physics, 2009. **11**: p. 095016.

6. Wallace, P.R., *The band theory of graphite* Physical Review, 1947. **71** (9): p. 622.

7. McClure, J.W., *Band structure of graphite and de haas-van alphen effect.* Physical Review, 1957. **108** (3): p. 612.

8. Sasaki, K., K. Wakabayashi, and T. Enoki, *Electron wave function in armchair graphene nanoribbons.* Journal of the Physical Society of Japan, 2011. **80** (4): p. 044710.

9. Wakabayashi, K. and S. Dutta, *Nanoscale and edge effect on electronic properties of graphene.* Solid State Communications, 2012. **152** (15): p. 1420.

10. Wakabayashi, K., K. Sasaki, T. Nakanishi, and T. Enoki, *Electronic states of graphene nanoribbons and analytical solutions.* Science and Technology of Advanced Materials, 2010. **11** (5): p. 054504.

11. Fujita, M., K. Wakabayashi, K. Nakada, and K. Kusakabe, *Peculiar localized state at zigzag graphite edge.* Journal of the Physical Society of Japan, 1996. **65** (7): p. 1920.

12. Son, Y.-W., M.L. Cohen, and S.G. Louie, *Energy gaps in graphene nanoribbons.* Physical Review Letters, 2006. **97** (21): p. 216803.

13. Nakada, K., M. Fujita, G. Dresselhaus, and M.S. Dresselhaus, *Edge state in graphene ribbons: Nanometer size effect and edge shape dependence.* Physical Review B, 1996. **54** (24): p. 17954.

14. Wakabayashi, K., M. Fujita, H. Ajiki, and M. Sigrist, *Electronic and magnetic properties of nanographite ribbons.* Physical Review B, 1999. **59** (12): p. 8271.

15. Ezawa, M., *Peculiar width dependence of the electronic properties of carbon nanoribbons.* Physical Review B, 2006. **73** (4): p. 045432.

16. Brey, L. and H.A. Fertig, *Electronic states of graphene nanoribbons studied with the dirac equation.* Physical Review B, 2006. **73** (23): p. 235411.

17. Zheng, H.X., Z.F. Wang, T. Luo, Q.W. Shi, and J. Chen, *Analytical study of electronic structure in armchair graphene nanoribbons.* Physical Review B, 2007. **75** (16): p. 165414.

18. Yang, L., C.H. Park, Y.W. Son, M.L. Cohen, and S.G. Louie, *Quasiparticle energies and band gaps in graphene nanoribbons.* Physical Review Letters, 2007. **99** (18): p. 186801.

19. Han, M.Y., B. Ozyilmaz, Y.B. Zhang, and P. Kim, *Energy band-gap engineering of graphene nanoribbons.* Physical Review Letters, 2007. **98** (20): p. 206805.

20. Cai, J.M., P. Ruffieux, R. Jaafar, M. Bieri, T. Braun, S. Blankenburg, et al., *Atomically precise bottom-up fabrication of graphene nanoribbons.* Nature, 2010. **466** (7305): p. 470.

21. Koch, M., F. Ample, C. Joachim, and L. Grill, *Voltage-dependent conductance of a single graphene nanoribbon.* Nature Nanotechnology, 2012. **7** (11): p. 713.

22. Linden, S., D. Zhong, A. Timmer, N. Aghdassi, J.H. Franke, H. Zhang, et al., *Electronic structure of spatially aligned graphene nanoribbons on au(788).* Physical Review Letters, 2012. **108** (21): p. 216801.

23. Huang, H., D.C. Wei, J.T. Sun, S.L. Wong, Y.P. Feng, A.H.C. Neto, and A.T.S. Wee, *Spatially resolved electronic structures of atomically precise armchair graphene nanoribbons.* Scientific Reports, 2012. **2**: p. 983.

24. Yen-Chia Chen, D.G.d.O., Zahra Pedramrazi, Chen Chen, Felix R. Fischer, and Michael F. Crommie, *Tuning the band gap of graphene nanoribbons synthesized from molecular precursors.* ACS Nano, 2013. **7** (7): p. 6123.

25. Tanaka, K., S. Yamashita, H. Yamabe, and T. Yamabe, *Electronic-properties of one-dimensional graphite family.* Synthetic Metals, 1987. **17** (1-3): p. 143.

26. Sato, T., M. Tanaka, and T. Yamabe, *Size-dependent homo-lumo gap oscillation of carbon nanotube with a finite length.* Synthetic Metals, 1999. **103** (1-3): p. 2525.

27. Treboux, G., P. Lapstun, and K. Silverbrook, *Loss of translational symmetry in carbon nanotubes.* Chemical Physics Letters, 1999. **302** (1-2): p. 60.

28. Yang, H., A.J. Mayne, M. Boucherit, G. Comtet, G. Dujardin, and Y. Kuk, *Quantum interference channeling at graphene edges.* Nano Letters, 2010. **10** (3): p. 943.

29. Reich, S., J. Maultzsch, C. Thomsen, and P. Ordejon, *Tight-binding description of graphene.* Physical Review B, 2002. **66** (3): p. 035412.

30. Wakabayashi, K., Y. Takane, M. Yamamoto, and M. Sigrist, *Edge effect on electronic transport properties of graphene nanoribbons and presence of perfectly conducting channel.* Carbon, 2009. **47** (1): p. 124.

31. Hod, O., J.E. Peralta, and G.E. Scuseria, *Edge effects in finite elongated graphene nanoribbons.* Physical Review B, 2007. **76** (23): p. 233401.

32. Ezawa, M., *Metallic graphene nanodisks: Electronic and magnetic properties.* Physical Review B, 2007. **76** (24): p. 245415.

33. Kudin, K.N., *Zigzag graphene nanoribbons with saturated edges.* Acs Nano, 2008. **2** (3): p. 516.

34. Chia, C.-I. and V.H. Crespi, *Stabilizing the zigzag edge: Graphene nanoribbons with sterically constrained terminations.* Physical Review Letters, 2012. **109** (7): p. 076802.

35. Wakabayashi, K., M. Sigrist, and M. Fujita, *Spin wave mode of edge-localized magnetic states in nanographite zigzag ribbons.* Journal of the Physical Society of Japan, 1998. **67** (6): p. 2089.

36. Wakabayashi, K. and K. Harigaya, *Magnetic structure of nano-graphite mobius ribbon.* Journal of the Physical Society of Japan, 2003. **72** (5): p. 998.

37. Yamashiro, A., Y. Shimoi, K. Harigaya, and K. Wakabayashi, *Spin- and charge-polarized states in nanographene ribbons with zigzag edges.* Physical Review B, 2003. **68** (19): p. 193410.

38. Harigaya, K. and T. Enoki, *Mechanism of magnetism in stacked nanographite with open shell electrons.* Chemical Physics Letters, 2002. **351** (1-2): p. 128.

39. Yoshioka, H., *Spin excitation in nano-graphite ribbons with zigzag edges.* Journal of the Physical Society of Japan, 2003. **72** (9): p. 2145.

40. Kumazaki, H. and D.S. Hirashima, *Local magnetic moment formation on edges of graphene.* Journal of the Physical Society of Japan, 2008. **77** (4): p. 044705.

41. Fernandez-Rossier, J. and J.J. Palacios, *Magnetism in graphene nanoislands.* Physical Review Letters, 2007. **99** (17): p. 177204.

42. Palacios, J.J., J. Fernandez-Rossier, L. Brey, and H.A. Fertig, *Electronic and magnetic structure of graphene nanoribbons.* Semiconductor Science and Technology, 2010. **25** (3): p. 033003.

43. Hikihara, T., X. Hu, H.H. Lin, and C.Y. Mou, *Ground-state properties of nanographite systems with zigzag edges.* Physical Review B, 2003. **68** (3): p. 035432.

44. Kusakabe, K. and M. Maruyama, *Magnetic nanographite.* Physical Review B, 2003. **67** (9): p. 092406.

45. Son, Y.W., M.L. Cohen, and S.G. Louie, *Half-metallic graphene nanoribbons.* Nature, 2006. **444** (7117): p. 347.

46. Furst, J.A., M. Brandbyge, and A.P. Jauho, *Atomic carbon chains as spin-transmitters: An ab initio transport study.* Epl, 2010. **91** (3): p. 37002.

47. Zeng, J., K.Q. Chen, J. He, X.J. Zhang, and C.Q. Sun, *Edge hydrogenation-induced spin-filtering and rectifying behaviors in the graphene nanoribbon heterojunctions.* Journal of Physical Chemistry C, 2011. **115** (50): p. 25072.

48. Kim, W.Y. and K.S. Kim, *Prediction of very large values of magnetoresistance in a graphene nanoribbon device.* Nature Nanotechnology, 2008. **3** (7): p. 408.

49. Farghadan, R. and E. Saievar-Iranizad, *Spin-polarized transport in zigzag-edge graphene nanoribbon junctions.* Journal of Applied Physics, 2012. **111** (1): p. 014304.

50. Ding, G.H. and C.T. Chan, *Spin-polarized electron transport through graphene nanoribbon with zigzag edges.* Journal of Physics-Condensed Matter, 2011. **23** (20): p. 205304.

51. Munoz-Rojas, F., J. Fernandez-Rossier, and J.J. Palacios, *Giant magnetoresistance in ultrasmall graphene based devices.* Physical Review Letters, 2009. **102** (13): p. 136810.

52. Zhao, H., X.-W. Zhang, T. Cai, T. Sang, X.-C. Liu, and F. Liu, *Spin-dependent transport induced by magnetization in zigzag graphene nanoribbons coupled to one-dimensional leads.* Chinese Physics B, 2012. **21** (1): p. 017305.

53. Farghadan, R. and E. Saievar-Iranizad, *Spin-polarized edge and magnetoresistance in graphene flake.* Solid State Communications, 2011. **151** (23): p. 1763.

54. Ma, Z.L. and W.D. Sheng, *A spin-valve device based on dumbbell-shaped graphene nanoislands.* Applied Physics Letters, 2011. **99** (8): p. 083101.

55. Lakshmi, S., S. Roche, and G. Cuniberti, *Spin-valve effect in zigzag graphene nanoribbons by defect engineering.* Physical Review B, 2009. **80** (19): p. 193404.

56. Weymann, I., J. Barnas, and S. Krompiewski, *Manifestation of the shape and edge effects in spin-resolved transport through graphene quantum dots.* Physical Review B, 2012. **85** (20): p. 205306.

57. Kobayashi, Y., K. Fukui, T. Enoki, K. Kusakabe, and Y. Kaburagi, *Observation of zigzag and armchair edges of graphite using scanning tunneling microscopy and spectroscopy.* Physical Review B, 2005. **71** (19): p. 193406.

58. Kobayashi, Y., K. Fukui, T. Enoki, and K. Kusakabe, *Edge state on hydrogen-terminated graphite edges investigated by scanning tunneling microscopy.* Physical Review B, 2006. **73** (12): p. 125415.

59. Niimi, Y., T. Matsui, H. Kambara, K. Tagami, M. Tsukada, and H. Fukuyama, *Scanning tunneling microscopy and spectroscopy studies of graphite edges.* Applied Surface Science, 2005. **241** (1-2): p. 43.

60. Tao, C.G., L.Y. Jiao, O.V. Yazyev, Y.C. Chen, J.J. Feng, X.W. Zhang, et al., *Spatially resolving edge states of chiral graphene nanoribbons.* Nature Physics, 2011. **7** (8): p. 616.

61. Sugawara, K., T. Sato, S. Souma, T. Takahashi, and H. Suematsu, *Fermi surface and edge-localized states in graphite studied by high-resolution angle-resolved photoemission spectroscopy.* Physical Review B, 2006. **73** (4): p. 045124.

62. Lafferentz, L., F. Ample, H. Yu, S. Hecht, C. Joachim, and L. Grill, *Conductance of a single conjugated polymer as a continuous function of its length.* Science, 2009. **323**: p. 1193.

63. Choi, S.H., B. Kim, and C.D. Frisbie, *Electrical resistance of long conjugated molecular wires.* Science, 2008. **320** (5882): p. 1482.

64. Davis, W.B., W.A. Svec, M.A. Ratner, and M.R. Wasielewski, *Molecular-wire behaviour in p-phenylenevinylene oligomers.* Nature, 1998. **396** (6706): p. 60.

65. Engelkes, V.B., J.M. Beebe, and C.D. Frisbie, *Length-dependent transport in molecular junctions based on sams of alkanethiols and alkanedithiols: Effect of metal work function and applied bias on tunneling efficiency and contact resistance.* Journal of the American Chemical Society, 2004. **126** (43): p. 14287.

66. Wang, W.Y., T. Lee, and M.A. Reed, *Mechanism of electron conduction in self-assembled alkanethiol monolayer devices.* Physical Review B, 2003. **68** (3): p. 035416.

67. Venkataraman, L., J.E. Klare, C. Nuckolls, M.S. Hybertsen, and M.L. Steigerwald, *Dependence of single-molecule junction conductance on molecular conformation.* Nature, 2006. **442** (7105): p. 904.

68. Lafferentz, L., F. Ample, H. Yu, S. Hecht, C. Joachim, and L. Grill, *Conductance of a single conjugated polymer as a continuous function of its length.* Science, 2009. **323** (5918): p. 1193.

69. Quek, S.Y., H.J. Choi, S.G. Louie, and J.B. Neaton, *Length dependence of conductance in aromatic single-molecule junctions.* Nano Letters, 2009. **9** (11): p. 3949.

70. He, J., F. Chen, S. Lindsay, and C. Nuckolls, *Length dependence of charge transport in oligoanilines.* Applied Physics Letters, 2007. **90** (7): p. 072112.

71. McConnell, H., *Intramolecular charge transfer in aromatic free radicals.* Journal of Chemical Physics, 1961. **35** (2): p. 508.

72. Magoga, M. and C. Joachim, *Conductance and transparence of long molecular wires.* Physical Review B, 1997. **56** (8): p. 4722.

73. Mujica, V., A. Nitzan, Y. Mao, W. Davis, M. Kemp, A. Roitberg, and M.A. Ratner, *Electron transfer in molecules and molecular wires: Geometry dependence, coherent transfer, and control.* Advancements in Chemical Physics, 1999. **107**: p. 403.

74. Hohenberg, P. and W. Kohn, *Inhomogeneous electron gas.* Physical Review B, 1964. **136** (3B): p. B864.

75. Soler, J.M., E. Artacho, J.D. Gale, A. Garcia, J. Junquera, P. Ordejon, and D. Sanchez-Portal, *The siesta method for ab initio order-n materials simulation.* Journal of Physics-Condensed Matter, 2002. **14** (11): p. 2745.

76. Choi, H.J., M.L. Cohen, and S.G. Louie, *First-principles scattering-state approach for nonlinear electrical transport in nanostructures.* Physical Review B, 2007. **76** (15): p. 155420.

77. Davies, J.H., *The physics of low-dimensional semiconductors : An introduction*. 1998, New York : Cambridge University Press.

78. K. stokbro, J.T., M. Brandbyge, and H. Guo, *Ab-initio non-equilibrium green's function formalism for calculating electron transport in molecular devices*, in *Introducing molecular electronics*. 2005. p. 117-151.

79. *Wikipedia: Dirac delta function*. Available from: http://en.wikipedia.org/wiki/Sokhotski%E2%80%93Plemelj_theorem.

80. Vladimirov, V.S., *Equations of mathematical physics*. 1971.

81. Datta, S., *Electronic transport in mesoscopic systems*. 1997.

82. Xue, Y.Q., S. Datta, and M.A. Ratner, *First-principles based matrix green's function approach to molecular electronic devices: General formalism.* Chemical Physics, 2002. **281** (2-3).

83. Brandbyge, M., J.-L. Mozos, P. Ordejón, J. Taylor, and K. Stokbro, *Density-functional method for nonequilibrium electron transport.* Physical Review B, 2002. **65** (16): p. 165401.

84. Hartmut Haug, A.-P.J., *Quantum kinetics in transport and optics of semiconductors*. Vol. 123. 2008.

85. Taylor, J., H. Guo, and J. Wang, *Ab initio modeling of open systems: Charge transfer, electron conduction, and molecular switching of a c-60 device.* Physical Review B, 2001. **63** (12): p. 121104.

86. Li, S., C.K. Gan, Y.-W. Son, Y.P. Feng, and S.Y. Quek, *Anomalous length-independent frontier resonant transmission peaks in armchair graphene nanoribbon molecular wires.* Carbon, 2014. **76** (0): p. 285.

87. *Intelligent materials*. 2008: London: Royal Society of Chemistry.

88. Beneking, H., *High speed semiconductor devices: Circuit aspects and fundamental behaviour*. 1994: Springer Science & Business Media.

89. Rakshit, T., G.C. Liang, A.W. Ghosh, and S. Datta, *Silicon-based molecular electronics.* Nano Letters, 2004. **4** (10): p. 1803.

90. Bellaiche, L. and D. Vanderbilt, *Virtual crystal approximation revisited: Application to dielectric and piezoelectric properties of perovskites.* Physical Review B, 2000. **61** (12): p. 7877.

91. Saha, K.K. and B.K. Nikolic, *Negative differential resistance in graphene-nanoribbon-carbon-nanotube crossbars: A first-principles multiterminal quantum transport study*. Journal of Computational Electronics, 2013. **12** (4): p. 542.

92. Ramesh, A., P.R. Berger, and R. Loo, *High 5.2 peak-to-valley current ratio in si/sige resonant interband tunnel diodes grown by chemical vapor deposition.* Applied Physics Letters, 2012. **100** (9): p. 092104.